Design Strategies for Shape-Controlled Magnetic Iron Oxide Nanoparticles

Alejandro G. Roca[a,b,*], Lucía Gutiérrez[a,c,*], Helena Gavilán[a], María Eugênia Fortes Brollo[a], Sabino Veintemillas-Verdaguer[a], María del Puerto Morales[a]

[a,] Instituto de Ciencia de Materiales de Madrid, Consejo Superior de Investigaciones Científicas, Cantoblanco, E-28049 Madrid, Spain

[b] Catalan Institute of Nanoscience and Nanotechnology (ICN2), CSIC and BIST, Campus UAB, Bellaterra, E-08193 Barcelona, Spain

[c]Dept. Química Analítica, Instituto de Nanociencia de Aragón, Universidad de Zaragoza and CIBER-BBN, E-50018 Zaragoza, Spain

Corresponding author: E-mail: alejandrogroca@gmail.com; lu@unizar.es

Keywords: Magnetic nanoparticles; anisometry; shape anisotropy; nanocubes; elongated nanoparticles; disks; hollow nanoparticles; nanocitotoxicity; biomedical applications

Abstract:

Ferrimagnetic iron oxide nanoparticles (magnetite or maghemite) have been the subject of an intense research since ancient times, not only for fundamental research but also for their potentiality in a widespread number of practical applications. Most of these studies were focused on nanoparticles with spherical morphology but recently there is an emerging interest on anisometric nanoparticles. This review is focused on the synthesis routes for the production of uniform anisometric magnetite/maghemite nanoparticles with different morphologies like cubes, rods, disks, flowers and many others, such as hollow spheres, worms, stars or tetrapods. We analyse key parameters governing the production of these nanoparticles and, in particular, the role of the ligands in the final nanoparticle morphology. The main structural and magnetic features as well as the nanotoxicity as a function of the nanoparticle morphology are also described. Finally, the impact of

each morphology on the different biomedical applications (hyperthermia, magnetic resonance imaging and drug delivery) are analysed in detail but other applications such as spintronics, magnetic recording media, microwave absorption or environmental remediation are also discussed.

We would like to dedicate this work to Professor Carlos J. Serna, Instituto de Ciencia de Materiales de Madrid, ICMM/CSIC, for his outstanding contribution in the field of monodispersed colloids and iron oxide nanoparticles. We would like to express our gratitude for all these years of support and inspiration on the occasion of his retirement.

Contents

1. Introduction

In the last decades, nanocrystals have gained attention due to their unique properties at the nanoscale and have been used in different technological applications such as energy storage, catalysis, photonics, electronics or biomedicine.[1–10] The improvement of their performance has required innovative and continuous upgrades of the nanofabrication processes to yield "monodispersed colloids' consisting on uniform nanoparticles in both size and shape (e.g. size and shape distribution less than 10%).[11–16] In these systems, the overall physicochemical properties reflect the properties of each constituent, leading to size/shape-dependent performance materials. Apart of size and shape, aggregation and the internal structure, are important parameters that control the materials properties. The control of these parameters is linked to the synthesis route used for their preparation or the post-synthesis treatments.

Recently, different efforts have been made in developing new routes for the synthesis of anisometric nanocrystals (i.e. nanocrystals which differ from spherical shape) like nanocubes, nanorods, nanowires, nanodisks, and nanoflowers among others.[17–23] These materials possess direction-dependent properties, high surface-to-volume ratio and also particular crystal facets at the surface that can confer different reactivity.[24] The final shape of the nanocrystals is determined during the growth stage in the synthesis procedure, where thermodynamic and kinetic aspects control the reaction (see Fig.1).[25–29] In many cases, a general mechanism for the formation of these morphologies has not been fully described yet because of the difficulty in characterising the nanoparticle formation from the first stages. Those mechanisms include a complex combination of chemical reactions leading to the growth units, nucleation of first clusters, and final crystal growth by diffusion or self-assembly into aggregates.[30–32] In some cases, preferential adsorption of capping molecules to specific facets can hinder crystal growth in some directions resulting in

anisometric nanoparticles. [17,19,33,34] In other cases, the resulting morphology comes from an oriented aggregation of subunits due to an extra force such as a small magnetic or dielectric moment. [35–37] In summary, the synthetic route represents the trickiest step in the design of a nanomaterial for a specific application, as it will determine the particle size/shape, the size distribution, the surface chemistry of the particles and consequently their unique properties. However, the current scenario is that the most-developed recipes are not robust enough for synthesizing high-quality nanoparticles due to the poor understanding of the mechanisms of nucleation and growth during nanoparticle formation.

It is clear that under reduced dimensionality, shape is an important matter. For example, in the case of Au NPs, when Au turns anisometric (rod-shape, nanocages, nanoshell, etc.) a second plasmon resonance band arises at the near-infrared range which can be very advantageous for their application in biomedicine and sensing.[38–40] Changing rod aspect ratio affects the longitudinal plasmon resonance frequency which can be tuned systematically. Furthermore, ultrathin gold nanowires present mechanical flexibility and high conductivity.[41] Platinum nanocrystals, with high-performance in catalysis, have been obtained with peculiar morphologies (cubic dendrites or planar tripods) that provide high surface to volume ratio and controlled crystallographic facets.[42,43] For example, the hydrogenation of benzene is strongly affected by the Pt nanoparticle shape. Both cyclohexane and cyclohexene molecules were obtained using cubo-octahedral Pt nanocrystals, whereas only cyclohexane was selectively formed on cubic nanocrystals.[44] Anisometric magnetic nanoparticles of Fe, Co, FeCo and CoNi with high aspect ratio and enhanced magnetic properties have been obtained for permanent magnet applications. [45] However, the stability, as well as the dipolar interactions, limits the application of these materials.[46]

Among the iron oxide nanoparticles, the ferrimagnetic ones, magnetite and maghemite, (called “magnetic”) are of particular interest because of their potential in fields such as magnetic recording, separation and recycling, and in the biomedical area, in magnetic resonance imaging (MRI), targeted drug delivery, hyperthermia treatment of solid tumours, gene therapy and tissue regeneration.[34,47–52] For the above uses, most of the synthesis studies have been concentrated on spherical magnetite nanoparticles since they are, in general, easily obtained according to reproducible experimental procedures.[53,54] However, introducing anisotropy in magnetite nanoparticles can change substantially their magnetic properties.[34,55,56] The coercive field of the particles can be increased considerably by introducing shape anisotropy that can be up to two orders of magnitude larger than crystal anisotropy, as it is the case of magnetic recording nanoparticles.[57–59] The behaviour of the particles under an alternating magnetic field will also be different depending on the magnetic anisotropy. Thus, disk and rods magnetite nanoparticles have

been shown to induce mechanical damage of cancer cells,[60–62] while cubes, nanorings and nanoflowers seems to be ideal heat mediators for hyperthermia,[22,63–65].

In this review, we present an overview and recent progress on the preparation of well-controlled magnetite/maghemite nanoparticles with non-spherical shapes and the mechanisms proposed to control their formation. We have focused on the magnetite nanoparticle growth, either in one step or through a templated-assisted reduction process from other iron hydroxides/oxides such as goethite, lepidocrocite and hematite nanocrystals. This route has the advantage that the reduction preserves the anisometric morphology of the precursors. We describe the effect of key parameters on the final magnetite morphology, including: (i) control of the precursor's formation and growth, and (ii) effect of their crystalline phase and (iii) crystal orientation and facets exposed on the nanocrystals as a function of the shape. Those parameters can be classified as physical parameters (those that concern the number of steps and temperature and heating rate in each step) and chemical parameters (nature and concentration of reactives and solvents). We dedicate a section to ligands as it is one of the key parameters that control the reaction and one can manipulate to reach the desired morphology. Ligands can be very diverse in nature and they are able to favour a thermodynamic or kinetic regime but also control the relative growth rate between the different facets by binding specifically to particular ones. Structural and magnetic properties for each morphology are also reviewed and related to the synthetic route. Finally, the advantages of using magnetic anisometric nanoparticles for biomedical applications (magnetic hyperthermia, drug delivery and MRI) and other applications such as magnetic recording media, environmental remediation, Li-ion batteries, spintronics and microwave absorption are also summarised.

2. Synthesis of anisometric magnetic nanoparticles

Magnetite has a cubic inverse spinel structure and its space group is Fd3m with a cell parameter of 8.394 Å.[66] The unit cell contains 32 O^{2-} ions forming a cubic closed-packed system. Fe(II) ions are disposed in the octahedral sites and Fe(III) ions are located in both octahedral and tetrahedral sites (Fig.1). Maghemite (γ-Fe_2O_3) is formed during the oxidation of magnetite or by dehydration of lepidocrocite. [67] The direct synthesis of maghemite is not possible probably due to the presence of vacancies in octahedral positions (Fig.1).[68] Maghemite (γ-Fe_2O_3) has an inverse spinel structure like magnetite with a cell parameter slightly smaller (a=8.351-8.33 Å), containing vacancies located in the octahedral positions and Fe(III) ions in both octahedral and tetrahedral positions. The stoichiometry of maghemite can be described with the formula $Fe_{Td}(Fe_{5/3}\square_{1/3})_{Oh}O_4$ (Td= tetrahedral sites; Oh= octahedral sites). Depending on the extent and nature of vacancies ordering, three different crystal symmetries for maghemite can be described. In the first one, the

vacancies are randomly distributed in the octahedral positions (Fd3m space group). In the second one the vacancies are partially ordered ($P4_32_12$ and $P4_12_12$). In the last one, the vacancies are perfectly ordered forming a tetragonal superstructure along the c-axis where the value of c is around three times the value of a ($P4_32_12$ space group).[69–71]

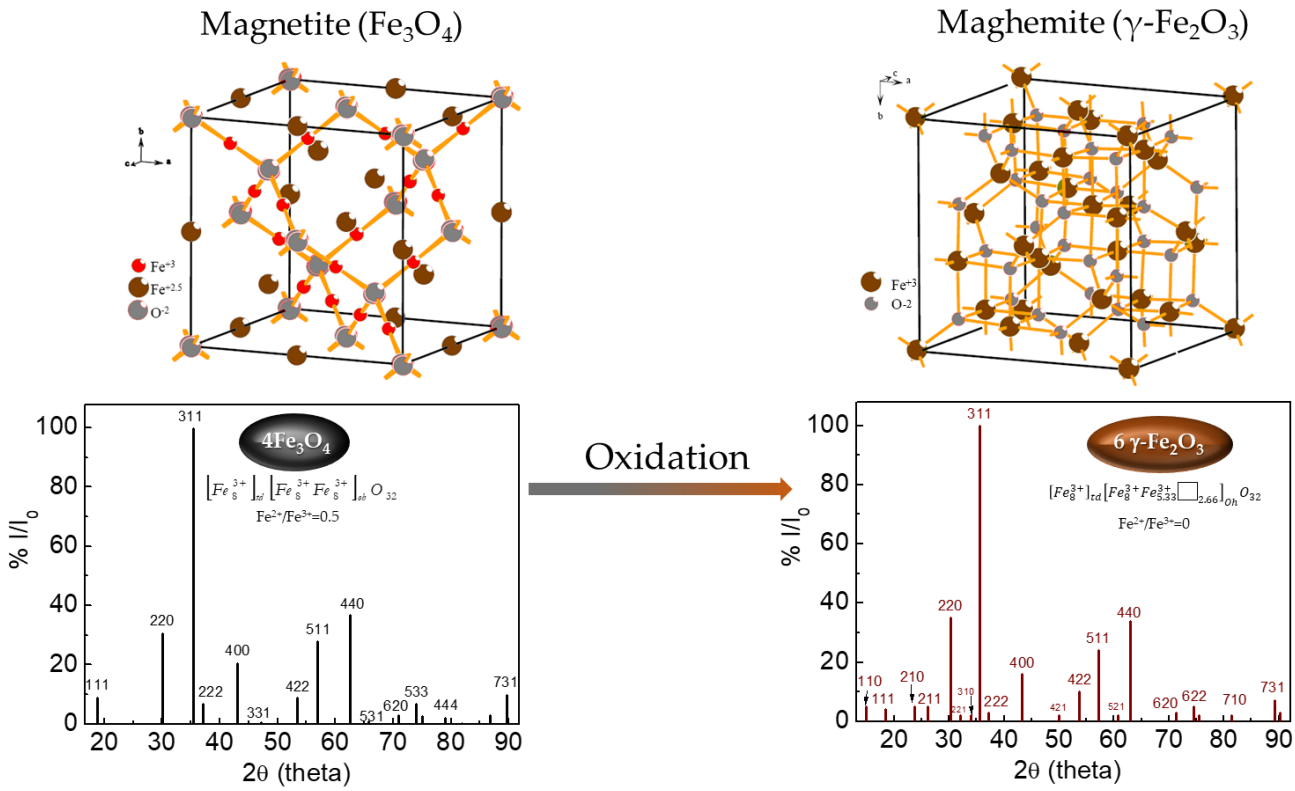

Fig.1. Crystal structure and x-ray diffraction pattern (using Cu Kα radiation) of magnetite and maghemite phases.

There are two different approaches for the direct synthesis of magnetite, i) starting from iron(II) or iron(III) inorganic salts such as nitrates, sulphates or chlorides, [72,73] or ii) starting from organic precursors such as iron oleates,[74] acetates,[75] acetylacetonates[76] or pentacarbonyl.[77] In most cases, a mild reducer or oxidizer is added to the reaction to get the final Fe_3O_4 stoichiometry. In other cases, indirect methods involve the initial synthesis and reduction of different iron oxide (hematite)[69] or oxohydroxide (goethite, akaganeite or lepidocrocite)[52] which acts as shape-template setting the final dimensions and shape of the nanostructure. If akaganeite or goethite are used as shape-templates, they are thermally transformed to magnetite through hematite. The well-known reduction of hematite to magnetite through a topotactic reaction is performed in dry conditions, i.e. static or dynamic atmosphere of H_2/Ar at temperatures not lower than 360 ºC.[78] The reduction can also be performed in wet conditions either in organic or aqueous media. In organic media, heating hematite or iron oxohydroxide nanoparticles in trioctylamine in

the presence of oleic acid at around 350 ºC leads to magnetite.[79,80] In aqueous media the reduction to magnetite is achieved by using hydrazine at alkaline pH range between 9.5 and 11.5 [81] through a dissolution-recrystallization mechanism.[82,83]

In the case of maghemite, it can be obtained through oxidation of magnetite at 240 ºC in air. However, when the size reduces to nano, oxidation temperature can be reduced down to 50 ºC and even at room temperature for long periods of time (1 year for sizes below 10 nm).[84] Finally, maghemite can also be obtained through dehydration of lepidocrocite (Fig. 2).

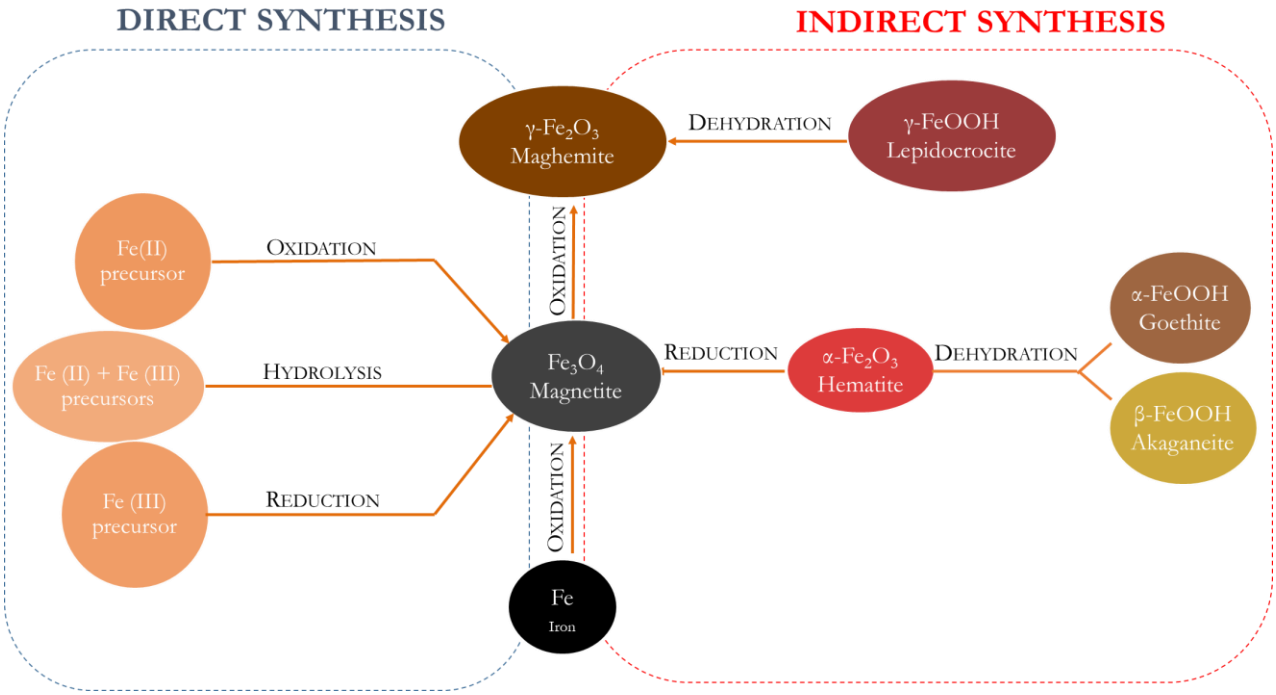

Fig. 2. Synthesis scheme and phase transformation to prepare Fe_3O_4 and γ-Fe_2O_3 nanoparticles.

It is important to mention that any colloidal synthesis route involves two main stages: nucleation and growth/agglomeration. In the case of the synthesis of monodisperse nanoparticles, both stages must be separated in temperature and time, otherwise broad size distributions and diverse particle morphology are obtained. For the case of anisometric nanoparticles, growth stage is the critical step responsible for the final morphology. There are different strategies to achieve a specific morphology that will be commented in the following sections but all of them are based on the induction of different growth rates on low index planes such as {111}, {110} and {100} with low surface energy.

2.1. Cubic-shaped nanoparticles

Magnetite is often found as cubes, octahedrons, and rhombododecahedrons, habits coming from the spinel structure (cubic). The synthesis of 0-D cubic-shaped nanocrystals in liquid can be

carried out by different routes depending on the nature of the solvent and the iron precursors (Fig. 3).

In water, the precipitation of an iron(II) salt in alkaline media in the presence of a mild oxidant such as potassium nitrate (KNO_3) at 90 ºC renders magnetite nanocubes but only under certain conditions.[85] The most critical parameter is the [Fe(II)]:[OH^-] ratio, so 33 nm nanocubes are achieved when [Fe(II)]:[OH^-] ratio is 0.77. Interestingly, when [Fe(II)]:[OH^-] gets closer to 1, size becomes larger (76 and 169 nm for [Fe(II)]:[OH^-] ratios of 0.97 and 0.997 respectively) and shape evolves to octahedral morphology. The kinetics of the reaction is affected by the pH and how far/close it is from the isoelectric point of magnetite (pH~7). [86,87] In excess of OH^-, i.e. the pH is above Fe_3O_4 isoelectric point, cubic particles are grown by slow diffusion of $Fe(OH)_2$ species to the primary particles (negatively charged). However, if the excess of OH^- is negligible, the growth takes place mainly by aggregation and the kinetic is much faster. Primary particles are not repelling each other since they are not sufficiently charged and the aggregation is followed by subsequent recrystallization leading to octahedral particles with larger sizes from few nanometers up to microns. Interestingly, the addition of ethanol induces the cubic morphology as well, and reduces the final size of the particles because it modifies the hydrolysis of ferrous and ferri oxo-aqueous species decreasing the critical diameter at which nuclei can be formed, and finally slows down the growth hampering the diffusion process.

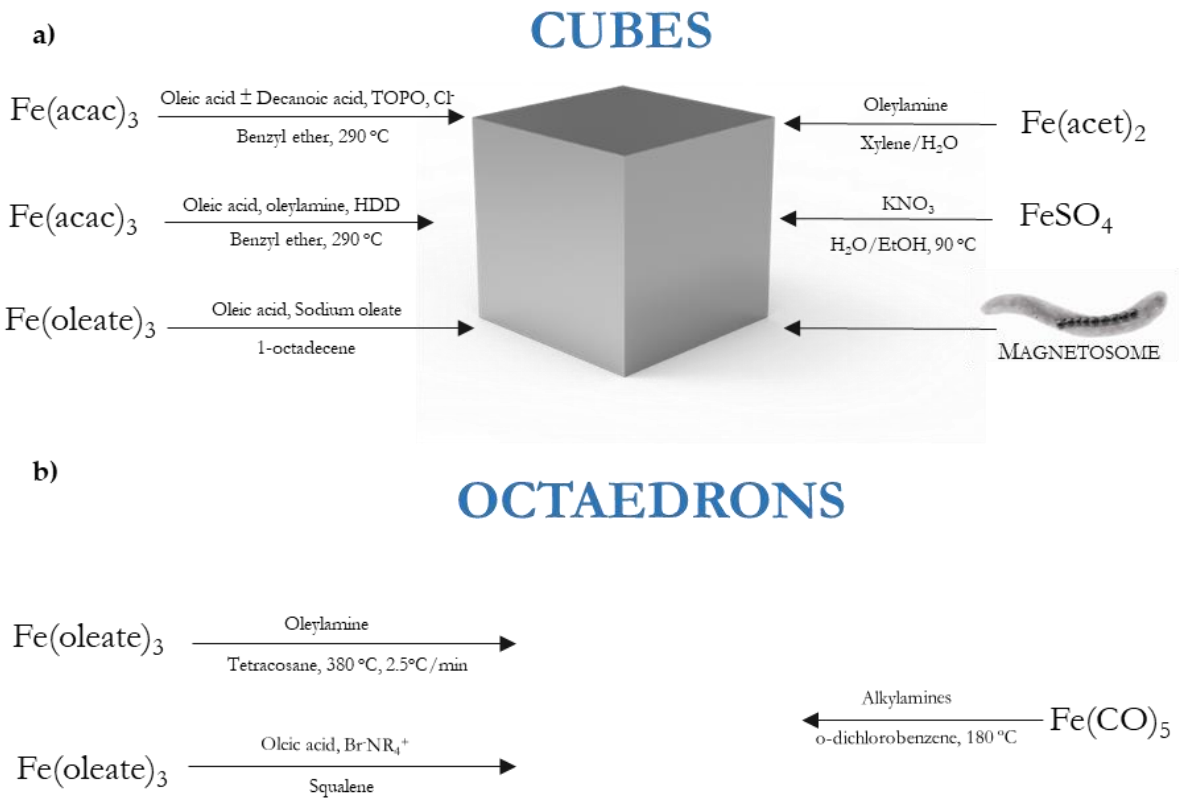

Fig. 3. Scheme of the synthetic routes for the growth of Fe_3O_4 nanocubes and nanoctahedrons. (Acac = Acetylacetonate, Acet = Acetate, EtOH = Ethanol, HDD = 1, 2-hexadecanediol, TOPO=Trioctylphosphine oxide, $Br^-NR_4^+$= Tetraalkylammonium bromide).

The decomposition of iron organic precursors in high boiling-point organic solvents in the presence of surfactants can lead to cubic magnetite nanoparticles with in a wide range of sizes and narrow size distribution (Fig. 4). The particle size can be tailored by changing both, the precursor concentration and reflux time. For example, 79 nm Fe_3O_4 nanocubes were grown by heating iron(III) acetylacetonate in benzyl ether in the presence of oleic acid.[88] Then, by doubling the precursor concentration and increasing the reflux from 30 min to 1, 1.5 and 2 hours it is possible to achieve larger particles of 110, 150 and 160 nm respectively. The cubic shape was induced by the high amount of active species in solution being the growth kinetically controlled. In addition, surfactant/precursor molar ratio and the type of surfactant are other crucial parameters to control the final nanoparticle size. For example, by decreasing the oleic acid/precursor ratio from 5/1 to 2/1 the mean size of the magnetite nanocubes increases from 16 to 104 nm. Oleic acid has a critical effect because it has the capacity of delaying the nucleation towards higher temperatures leading to smaller nuclei, but also modulating the particle growth kinetics. If oleic acid is exchanged by

decanoic acid, smaller particles are grown (size range of 5-30 nm with decanoic and 16-100 nm with oleic acid [89]) and can be tuned by changing the surfactant/iron ratio. Decanoic acid is much shorter than oleic acid and also linear, so probably the coordination with Fe_3O_4 facets is more efficient leading to a drastic decrease in the mean size. The same effect was observed with 4-biphenylcarboxylic acid, which leads to a sharp decrease in the mean particle size from 79 to 22 nm when used as impurity with oleic acid in the decomposition of iron(III) acetylacetonate.[88]

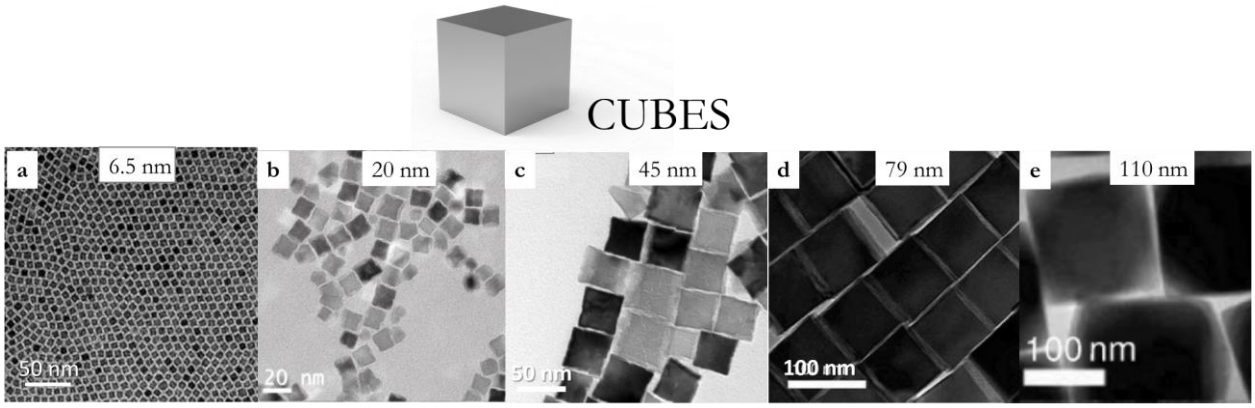

Fig. 4. TEM images of magnetite nanocubes synthesized by thermal decomposition with different mean sizes, a) 6.5 nm (Reproduced from [90] with the permission of AIP Publishing.; b) 20 nm, adapted with permission from [89] Copyright (2010) American Chemical Society; c) 45 nm, adapted with permission from [91] Copyright (2011) American Chemical Society; d) 79 nm, adapted with permission from [88] Copyright (2009) American Chemical Society; e) 110 nm. adapted with permission from [88] Copyright (2009) American Chemical Society.

Heating rate is other critical parameter to control the final nanoparticle size. For example, a huge enlargement from 13 to 180 nm can be achieved when the heating rate slows down from 5.2 to 0.8 $^{o}C \cdot min^{-1}$ in the decomposition of iron(III) acetylacetonate and decanoic acid in benzyl ether. The heating rate dominates the nucleation process of the nanocubes so when heating rate decreases the nucleation rate decreases too, less nuclei are formed and they are able to grow more.[90] Interestingly, in the same synthesis but using a surfactant mixture of oleic acid, oleylamine and 1,2-hexadecanediol, when the heating rate decreases from 35 to 5$^{o}C \cdot min^{-1}$, the size of the cubes increases from 5 to 30 nm.[90]

The nature of the surfactants has also been demonstrated to determine, at least in part, the final morphology of magnetite nanoparticles synthesised in organic media. For example, the addition of sodium or potassium oleate leads to cubic nanocrystals between 9 and 23 nm.[92] However, if the surfactant is replaced by oleic acid or dibutylammonium oleate, spherical

nanoparticles were grown. In this case cubic shape is induced by the selective adhesion of the sodium and potassium oleate on the {100} facets reducing its growth rate.[93] However, it should be noted that depending on the amount of oleate and the synthetic conditions during and post-synthesis, non-stoichiometric wüstite (FeO) can be formed.[94,95] Trioctylphosphine oxide (TOPO) [96], chloride ions[97] and β-amyrin[98] are other ligands which selectively bind to {100} facets inducing cubic shape.

Changing the precursor, it is possible to obtain magnetite octahedrons by thermal decomposition. Thus, the decomposition of iron(III) oleate in tetracosane in the presence of oleylamine leads to 21 nm Fe_3O_4 octahedral nanocrystals induced by the selective binding of oleylamine to {111} facets.[99] Furthermore, the use of quaternary ammonium bromide salts (which generate trioctylammonium bromide at high temperatures)[100,101] in conjunction with oleic acid in the decomposition of iron(III) oleate using squalene as solvent also leads to 50 nm Fe_3O_4 octahedrons. Interestingly, the increase of the alkylamine/Fe ratio from 2:1 to 10:1 using $Fe(CO)_5$ in o-dichlorobenzene leads to the formation of 50 nm hexagonal-shaped Fe_3O_4 nanocrystals because once the {111} facets are saturated of alkylamine molecules they bind to the second facet with the highest energy {110}.[102] Finally, heating a solution of iron(II) chloride in oleylamine up to 200 ºC at a rate of 10 $ºC \cdot min^{-1}$ renders 8 nm Fe_3O_4 octahedrons.[103] A synthetic strategy lying between the aqueous and organic media consist on the hydrolysis of iron(II) acetate in the presence of oleylamine dissolved in xylene. Heating the reaction mixture followed by fast injection of water triggers the hydrolysis of the Fe-oleylamine complex leading to 9 nm nanocubes.[104]

Recently, 47 nm rhombohedral Fe_3O_4 nanocrystals were synthesized using a three-step process, which comprises the generation of hematite nanoparticles, further encapsulation in silica and final reduction to magnetite. The first step is critical for the growth of rhombohedral scaffolding and it was achieved by solvothermal synthesis by heating at 180 ºC for 12 hours iron(III) chloride in a mixture of ethanol/water 5:1 using sodium acetate as base.[79]

Finally, biological synthesis of iron oxide nanocrystals, cubes and octahedron between 30 and 100 nm in size, can be generated by bacterial magnetosomes following a natural pathway and constitutes one of the most fascinating processes of iron biomineralization.[105–107] These magnetosomes (often ferrimagnetic) are grown enveloped in membranes and form chains, which allows the cells to align with external magnetic fields.

2.2. Elongated nanoparticles

By "elongated nanoparticles" we cover all the 1-D nanostructures described in the literature with different names such as nanowires, spindle, ellipsoids, needles, nanobelts, nanorice, rods or nanowhiskers (Fig.5). The different names are attributed to their different axial ratio and final morphology at the particle edges (sharp or rounded).

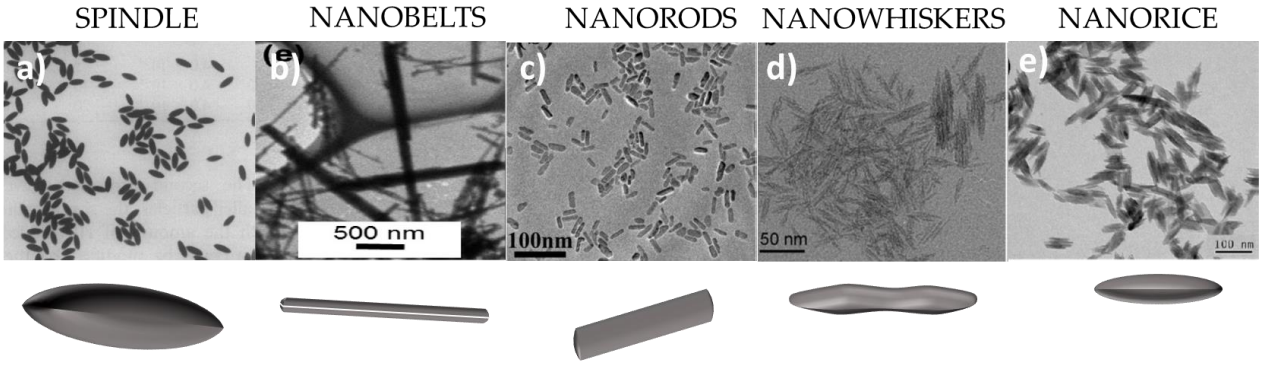

Fig. 5. Different types of elongated nanostructures reported in the bibliography. a) spindles, adapted/reprinted with permission from [108] © 1984, by Elsevier; b) nanobelts, adapted/reprinted with permission from [109], copyright (2011) American Chemical Society; c) nanorods, adapted/reprinted with permission from [80]), copyright © 2016, by Wiley; d) nanowhiskers, adapted/reprinted with permission from [110], copyright (2011) American Chemical Society; e) nanorice, adapted/reprinted with permission from [111], copyright © 2008, by Wiley.

Traditionally, synthetic strategies for the growth of elongated magnetic iron oxide nanostructures were based on aqueous media using other iron oxides or oxohydroxides as templates (Fig. 6 and 7). Interestingly, in the last years, one-step organic-based approaches have come up succeeding in the direct synthesis of elongated Fe_3O_4 nanoparticles that differ in the intermediate and the strategy to tailor length and axial ratio. Final properties will depend mainly on the geometry of the particles but also on the synthetic route used as it determines the internal structure (crystallinity, porosity and long axis direction).

Starting at the end of the 80´s and particularly during the 90´s, the main strategy for the synthesis of elongated magnetic nanoparticles for magnetic recording media was using goethite as shape template, followed by its transformation to hematite and further reduction to magnetite.

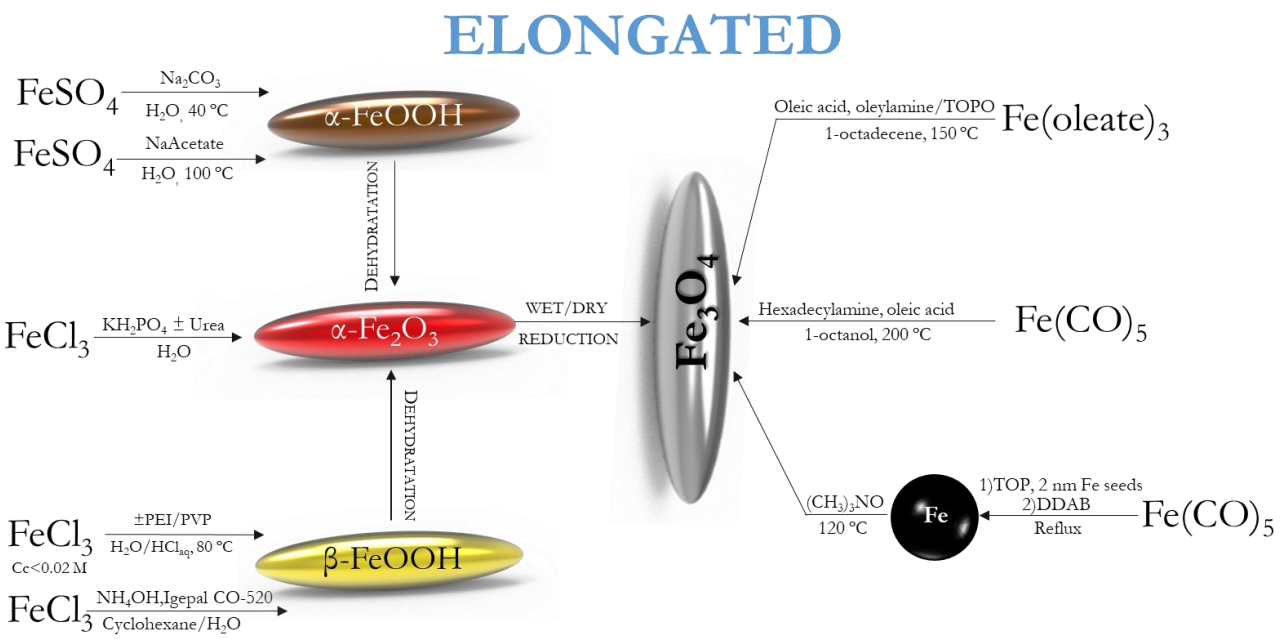

Fig. 6. Scheme of the synthetic routes to produce elongated Fe_3O_4 nanostructures. (PEI = Polyethyleneimine, PVP = Polyvinylpyrrolidone, TOP = Trioctylphosphine, DDAB = dodecyl dimethylammonium bromide).

Templating with goethite (α-FeOOH) as an intermediate, larger axial ratios up to 10 can be accomplished although the further thermal reduction produces a high porous structure associated to dehydroxilation. Uniform goethite particles with lengths ranging between 80 and 250 nm and diameters between 25 and 65 (axial ratios~3-4) can be obtained by hydrolysis and oxidation of iron(II) sulphate in water in the presence of carbonate ions at 40 ºC. The concentration of iron(II) sulphate and carbonate, air flow rate and reaction time are critical parameters to tailor the final nanoparticle dimensions.[111] Larger α-FeOOH particles can be grown by increasing the pressure and substituting sodium carbonate (Na_2CO_3) by sodium acetate (NaAc).The reaction takes place by hydrothermal synthesis at 100 ºC for 8 hours and leads to goethite rods of 170-300 nm in length and 15-25 nm in diameter (axial ratio around 10).[112]

Akaganeite (β-FeOOH) is the other iron oxohydroxide phase that serves as template for final synthesis of magnetite 1-D nanorods. In general, the hydrolysis of iron(III) chloride above a certain concentration (cc>0.02M) at 60-100 ºC in water for several hours renders β-FeOOH anisometric nanoparticles, whose length depends on the synthesis temperature, hydrolysis time, concentration of iron(III) chloride, internal pressure (hydrothermal synthesis) and the presence of several additives acting as pH modifiers to control the reaction kinetics or as shape/growth modulators. For example, β-FeOOH nanoparticles of 500 x 50 nm can be synthesized in water with a HCl concentration of

0.012 M at 100 ºC for 24 hours. Smaller rods of 200 x 22 nm were grown at 60 ºC without HCl and with a shorter the reaction time (5 h) rods of 72 x 10 nm were produced.[113] Reduction was carried out in liquid after protecting the akaganeite particles with silica by heating at 245 ºC in 2-hydroxiethyl ether. If the initial concentration of iron(III) chloride is around the nucleation limit for akaganeite (0.02 M), rods with 63 x 14 nm can be achieved.[114] Smaller rods (50 x 10 nm) were synthesized by hydrothermal treatment in a autoclave using short heating times (6 h).[80] Other strategy leading to a drastical reduction in size was the synthesis of akaganeite nanoparticles in the presence of polyethyleneimine (PEI) (from 291 x 42 nm to 32 x 5 nm (M_W PEI= 2500 g/mol)), because PEI is adsorbed on the lateral plane (200) of the nanorods, changing also the shape from rod to spindle with the edges more rounded (Fig. 7). [115,116] Moreover, the presence of polyvinylpryrrolidone (PVP) at 100 ºC for 12 h lead to hollow elongated particles of 300-200 x 30-50 nm after reduction.[117]

Finally, the use of a ternary water-in-oil/water system has been used to grow β-FeOOH nanoparticles. In this approach the iron(III) chloride solution is placed at the bottom and a water-in-oil microemulsion formed with cyclohexane and Igepal CO-520.[118] The aqueous phase of the microemulsion contains NH_4OH and when the system is destabilized by action of the temperature a phase separation begins. By gravity action, NH_4OH migrates to the bottom of the tube leading to the hydrolysis of the iron(III) chloride. Temperature reaction and concentration of iron(III) chloride and NH_4OH are the critical parameters to tailor the final dimensions. β-FeOOH rods of 45 x 8 nm were achieved when the concentration of $FeCl_3$ was 0.1 M and the volume of NH_4OH was 320 μL at 100 ºC, while the longest rods (450 x 120 nm) where grown using 1 M [$FeCl_3$] and 128 μL NH_4OH at 50 ºC. The reaction rate is slower at acidic pHs, (i.e. increasing the concentration of iron(III) chloride or decreasing the concentration of NH_4OH) and at lower temperatures, leading to larger particles.

Other strategy for the synthesis of elongated magnetite nanoparticles is based on the synthesis of hematite (α-Fe_2O_3) elongated particles as shape template. Hematite can be directly synthesized by forced hydrolysis of iron(III) salt (i.e. chloride and perchlorate) at 100 ºC during several days in the presence of phosphate ions, which are the responsible for conferring the anisometric growth along the c-axis and setting the axial ratio, leading to particles from 100 to 500 nm in length and axial ratios (length/width) between 1 and 5 (Fig. 7).[36,69] It is worth to mention that pure hematite can be obtained in certain ranges of iron(III) chloride concentrations, otherwise, akaganeite phase (β-FeOOH) or amorphous phases are obtained. In general, the particle size can be tailored with the concentration of the ferric salt, pH, solvent and ions present in the solution.[83,119] Furthermore, hot-injection of iron(III) chloride salt at 100 ºC leads to hematite

nanostructures with axial ratios around 3.[120] The main disadvantages of the direct synthesis of hematite is the long reaction time (several days) and the poor yield. Additives such as urea overcome these disadvantages reducing the synthesis time and increasing the yield (because of the hydroxyl anions release that promotes β-FeOOH precipitation) resulting in structures with an aspect ratio close to 10. [121,122] [122]

At the beginning of the last decade synthetic methods to grow 1D Fe_3O_4 nanostructures based in organic media and surfactants have experienced a great upsurge. Direct routes for the growth of elongated particles start with the formation of nuclei with octahedral shape. The exposition of {111} facets permits the anisometric growth along the [111] direction.[123] Another option is the growth along the [100] direction by elongation of the octahedral edges. For example, seeded-growth of a mixture of iron(0) pentacarbonyl with trioctylphosphine (TOP) to a suspension

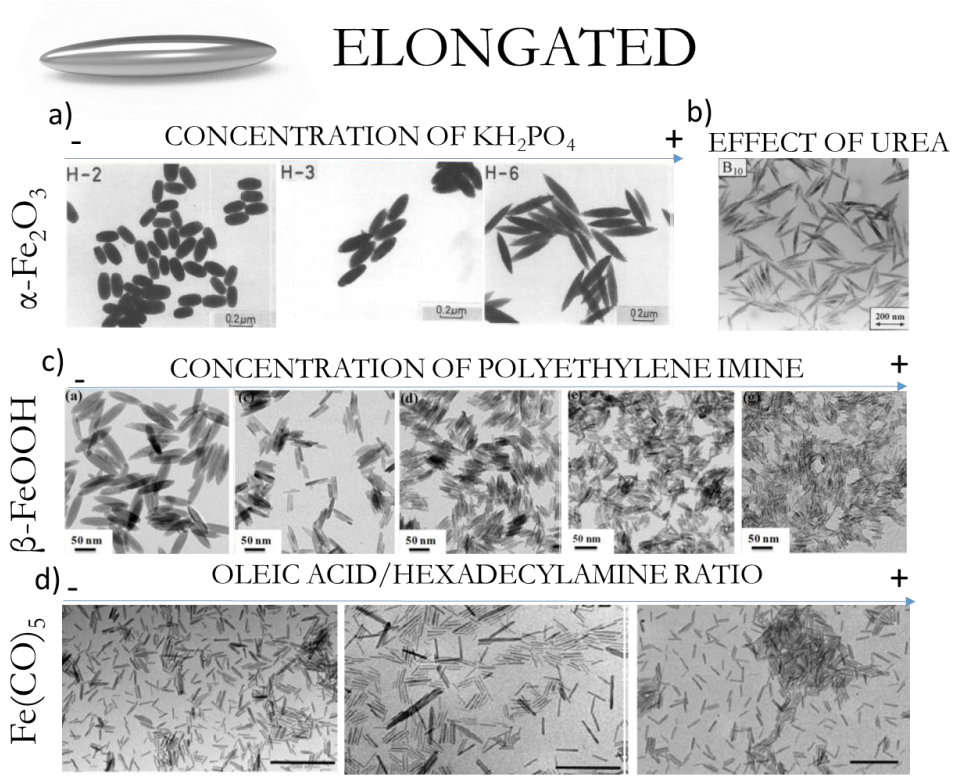

Fig. 7. TEM images of Fe_3O_4 elongated nanoparticles with different sizes modulated by tailoring different reaction parameters. a) Concentration of KH_2PO_4. Adapted/reprinted with permission from [36], © 2010, by Cambridge University Press; b) Effect of urea; adapted/reprinted with permission from [122] © 1999, by Elsevier; c) Concentration of polyethylenene imine; adapted/reprinted from [115], ©2015, by The Royal Society of Chemistry; d) Oleic acid/hexadecylamine ratio. adapted/reprinted with permission from [124], copyright (2016) American Chemical Society.

containing 2 nm Fe particles capped with trioctylphosphine oxide (TOPO) at high temperatures, followed by a reflux with dodecyl dimethylammonium bromide (DDAB) leads to Fe nanorods of 11 x 2 nm.[123] By increasing the concentration of DDAB it is possible to reach magnetite nanoparticles 27 nm in length without changing the diameter. The formation of the rod shape can be understood by the unidirectional coalescence of the spherical nanoparticles induced by the strong attachment of the DDAB molecules to the central part of the particle.

The synthesis of iron oxide nanowhiskers (20 x 2 nm) can be done by selective decomposition of iron(III) oleate in 1-octadecene in the presence of a surfactant mixture composed by oleic acid, oleylamine and TOPO.[110] In this synthesis route, the temperature (150 ºC) is too low to produce the decomposition of iron(III) oleic complex which is reported to take place at around 300 ºC.[92] Consequently, an alternative mechanism suggests that these nanowhiskers were produced by hydrolysis of iron(III) oleate complex. In this sense, a further step forward in the synthesis was the exchange of the iron(III) oleate by iron pentacarbonyl with a more controllable decomposition and reactivity. The addition of iron(0) pentacarbonyl to a mixture of hexadecylamine, oleic acid and 1-octanol in a solvothermal synthesis heated at 200 ºC for 6 hours renders rods of 63 x 6.5 nm in size (axial ratio~10). Length and axial ratio can be increased up to 140 x 12 nm (axial ratio ~12) by increasing the amount of hexadecylamine from 0.2 to 0.6 g probably due to the amount of water generated during the hydrolysis (Fig. 7). However, it is worth to note that the 1-D nanostructure formation requires an optimum amount of oleic acid and hexadecylamine. In summary, the proposed mechanism of this reaction is as follows. First, oleic acid is involved into two different reactions, i) formation of Fe(0)-oleic complex and ii) formation of a amide via reaction with hexadecylamine which renders water molecules. Then, part of the Fe(0)-oleic complex generates Fe nuclei, which rapidly oxidizes to FeO and the rest is hydrolysed by the water molecules generated before leading to Fe_3O_4. Due to the slow water releasing rate, the cluster concentration is below the nucleation threshold so there is a heteronucleation of the initial Fe_3O_4 nanorods on the surface of the FeO nuclei. Finally, another important parameter to control the final dimension and aspect ratio is the autoinduced pressure inside the reactor that can be tailored by changing the filling percentage of the reaction vessel. When the reaction volume decreases from the 80 to 53%, the length decreases from 163 to 56 nm and the axial ratio from 12 to 5.6 approximately.[124]

2.3. Disk-shaped nanoparticles

The synthesis of Fe_3O_4 nanodisks/nanoflakes/nanoplates has been reported through a two-step methodology consisting on the formation of α-Fe_2O_3 by the solvothermal route and further

reduction to Fe_3O_4 (Fig. 8). The formation of hematite nanodisks can be achieved by the hydrolysis of iron(III) chloride in a mixture of water/ethanol with the presence of sodium acetate. This reaction is carried out under hydrothermal conditions at 180 ºC for 12 hours growing nanodisks with 226 x 26 nm size (aspect ratio, i.e. thickness/diameter ~ 0.11).[125] Diameter and thickness can be controlled by the amount of water in the solvent and sodium acetate in the formation of hematite.[126] Thus, nucleation is delayed in absence of water forming spherical particles at first instance, which rapidly transform to iron oxide structures with circle-pancake shape instead of hexagonal plates after several days. Water acts as an accelerating agent, which leads to an increase of the thickness and decrease on the diameter. Diameter and thickness of nanodisks changes from 400 x 8 nm to 40 x 40 nm respectively when the volume of water added increases from 0.3 to 2.5 mL. The decrease of the alcohol polarity also leads to a decrease in the aspect ratio. Finally, sodium acetate also regulates the growth of the nanodisks because it strongly coordinates to surface atoms on (001) planes of hematite. If sodium acetate is not present or is just in a minimum amount in the reaction, small particles are synthesized. However, for a certain range, it coordinates to (0001) facets leading to decrease in the aspect ratio (thickness decreases as the diameter increases). Based in the same strategy magnetite nanodisks were synthesized by using Na_2SiO_3 instead of sodium acetate, and heating in a microwave digestion system for 30 minutes at temperatures higher than 140 ºC, achieving nanodisks of 100 x 60 nm.[127]. Smaller nanoplates of 35 nm in lateral size with a thickness of 10-13 nm were synthesized in two steps (Fig. 8). The first step consists on the reaction of iron(III) chloride with polyviniylpyrrolidone (PVP) in ethanol at 240 ºC under solvothermal conditions to lead to maghemite nanoparticles. In a second step, using n-octanol as solvent, the addition of more PVP and hydrazine completes the transformation to magnetite by heating up to 180 ºC for 6 hours.[128]. Nanoplate size can be controlled through the first reaction by tailoring the temperature and the reaction time. However, if the temperature of the reaction is 180 ºC, hematite is obtained instead of magnetite.

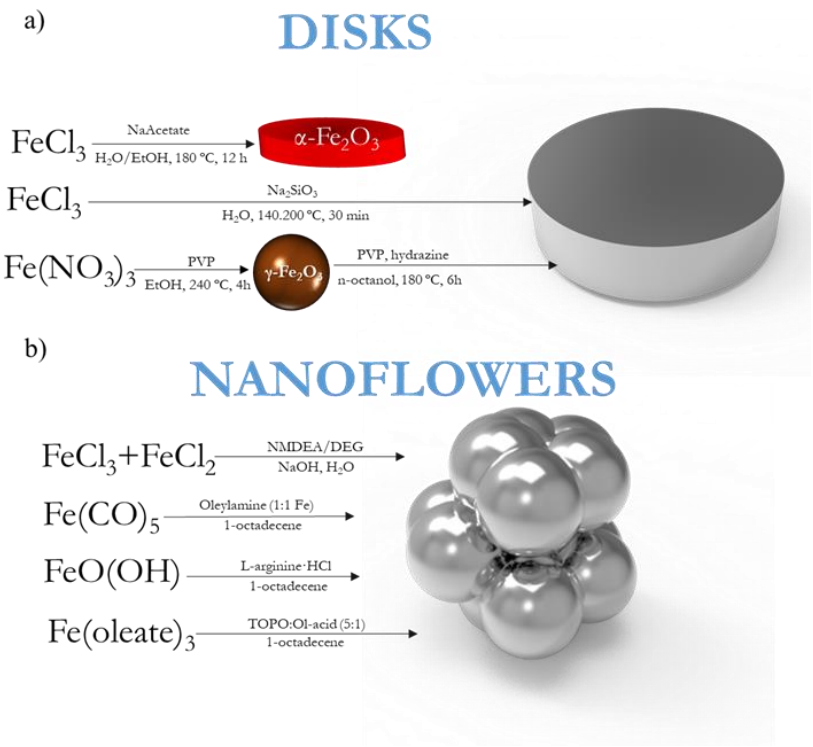

Fig. 8. Synthesis routes to obtain magnetite nanodisks/plates and nanoflowers. (PVP = Polyvinyl pyrrolidone, NMDEA = N-methyldiethanolamine, DEG = Diethyelene glycol).

2.4. Flower-like nanoparticles

Magnetite nanoparticles are able to aggregate in a hierarchical way that can form 3D structures with flower-like morphology. This morphology consists on the controlled aggregation of superparamagnetic iron oxide cores which form the final particles. Apart from the core size, another important parameter is the final aggregate size of the particles and the degree of fusion between cores. Both sizes are controlled and tailored essentially by selecting the synthetic route and the reagents involved in the reaction. There are two clear strategies to synthesize the 3D flower-like Fe_3O_4 nanostructures that can be differentiated in the final size: the polyol route and thermal decomposition (Fig. 8 and 9).

The polyol method has been used in the growth of flower-like nanostructures through alkaline hydrolysis of iron salts at high temperatures and slow rates. Briefly, this synthesis consist in the alkaline hydrolysis of both iron(II) and iron(III) chlorides using polyols as solvents at temperatures between 210 and 220 ºC. Interestingly, the inclusion of N-methyldiethanolamine (NMDEA) in the solvent mixture with ethylene glycol (EG) or alone makes possible the formation

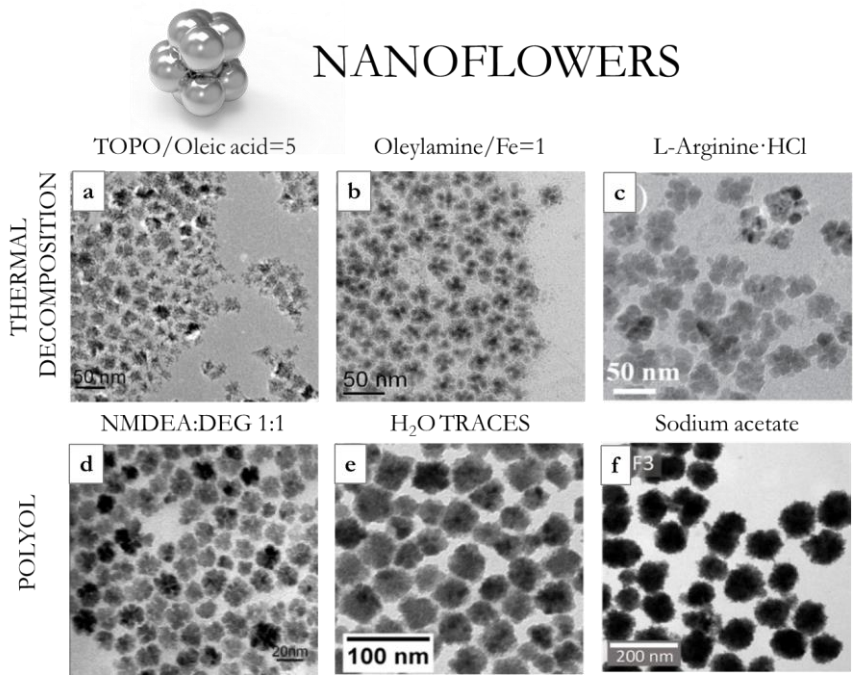

Fig. 9. TEM images of diverse nanoflower-like Fe_3O_4 nanoparticles synthesized under different conditions; a) Thermal decomposition; b-d) Polyol method. Sources: a) adapted/reprinted with permission from [129], © 2012, by The Royal Society of Chemistry; b) adapted/reprinted with permission from [130], copyright (2017) American Chemical Society; c) adapted/reprinted with permission from[131], © 2017, by Wiley; d) adapted/reprinted with permission from[132], copyright (2004) American Chemical Society.

of flower-like Fe_3O_4 nanoparticles, otherwise spherical single core Fe_3O_4 particles are grown. The generation of primary units of 4-6 nm quickly agglomerates to 11-16 nm cores that aggregate up to 55 nm particles depending on the amount of NaOH and the time at 220 ºC. [22,133] Starting from an iron(II) salts in polyol media, in the presence of different polymers such as polyvinylpyrrolidone (PVP), or citrate and using an autoclave for long time heating at high temperature, larger flower-like particles between 50 and 250 nm in size composed of 5-15 nm cores are obtained. PVP and sodium acetate (NaAc) can be used to increase the stability of the as-synthesized colloid, achieving flower-like nanoparticles with tuneable size and shape.[134–138] Besides, this type of flower-like nanoparticles can be obtained with a carbon shell structure using ferrocene as a single reactant.

[139,140] Interestingly, by forcing the magnetic interaction of the cores using a polymeric matrix, flower-like nanoparticles of regular size can be achieved.[63,141]

Fe_3O_4 nanoflowers can be also synthesized by thermal decomposition in organic media. For example, the decomposition of iron(0) pentacarbonyl in 1-octadecene in the presence of oleylamine with a equimolar ratio of Fe and oleylamine leads to 17 nm aggregates composed by small crystals of around 5 nm.[142] The low concentration of oleylamine that cannot prevent the agglomeration of the particles points as the reason for the formation of these Fe_3O_4 nanoflowers. Also, the use of L-arginine monohydrochloride in the decomposition of FeO(OH) in 1-octadecene leads to 40 nm flower-like aggregates. Ostwald ripening seems to be responsible for the formation of the aggregates and chloride ions from L-arginine seem crucial for reaching the flower-like structure.[143] Moreover, the decomposition of iron(III) oleate in a surfactant mixture of trioctylphosphine oxide (TOPO) and oleic acid (5:1 in molar ratio) renders aggregates of Fe_3O_4 with a size around 20 nm composed of small 5 nm nanocrystals. In this scenario, TOPO induces a burst nucleation at 290 ºC (synthesis temperature) leading to a huge number of nuclei that no further grow so, in order to minimize surface energy, the nuclei tend to aggregate.[129] Also calixarene molecules have been shown to stabilize intermediate reaction stages, leading to flower-like structures before magnetite particles are transformed to octahedrons. [144]

2.5. Other shapes

In this section those morphologies which cannot be fully identified with the aforementioned ones are covered (Fig. 10, 11 and 12). The most studied nanoparticles from this group are the hollow ones. The synthesis of **hollow nanoparticles** emerged at the beginning of this century for their possible applications in catalysis, lithium-ion batteries and drug delivery. There are different approaches to achieve the hollowed morphology, including hollow nanorings, nanotubes and also rods, but all of them are based on the carving of a sacrificial template by different mechanisms (Fig. 10).

The most common hollow nanostructures are **hollow spheres** (Fig. 10). Etching can be carried out using Fe_3O_4 nanoparticles as template. Heating magnetite nanoparticles in technical TOPO at 300 ºC for 2 h leads to hollow nanoparticles. It seems that the responsible for this carving effect is the presence of alkyl phosphonic acid as impurity which coordinates to the surface Fe ions of the particles, dissolves the ions by forming an iron-phosphonate complex and generates a pseudo-Kirkendall process where there is an inward diffusion of phosphorous and oxygen and outward diffusion of Fe ions.[145] Fe_3O_4 nanoparticles in a range of 11-24 nm have been

successfully etched leading to equivalent size structures with a minimum shell thickness of 3 nm, while particles smaller than 10 nm are dissolved.

Using core/shell Fe/Fe_3O_4 nanoparticles as sacrificial template, it is also possible to fabricate hollow Fe_3O_4 nanoparticles inducing a Kirkendall reaction by flowing oxygen into the reaction at high temperatures (Fig. 10). There are different ways to mix the colloidal Fe/Fe_3O_4 suspension with oxygen, i.e. flowing Ar enriched with O_2 (20%, 20 mL/min)[146], decomposing trimethylamine N-oxide $(CH_3)_3NO$) at 210 ºC[147] or at the expense of oxygen captured inside a sputtering deposition chamber.[148] It has been observed that the existence of a passivated layer of Fe_3O_4 is necessary to start the oxidation due to the unbalanced interfacial diffusion of oxygen and Fe atoms.[77] Hollowing mechanism begins once the Fe/Fe_3O_4 nanoparticles are in contact with O_2 because it triggers the outward diffusion of Fe ions to the outer shell and oxygen ions inward. Fe ions diffuse faster so Fe_3O_4 collects at the metal oxide interface leaving vacancies behind which coalesces into a single central cavity. With this approach hollow Fe_3O_4 nanoparticles from 4 to 20 nm with a shell thickness between 3 and 4 nm have been synthesised controlling the extension of the oxidation process by controlling temperature and time.

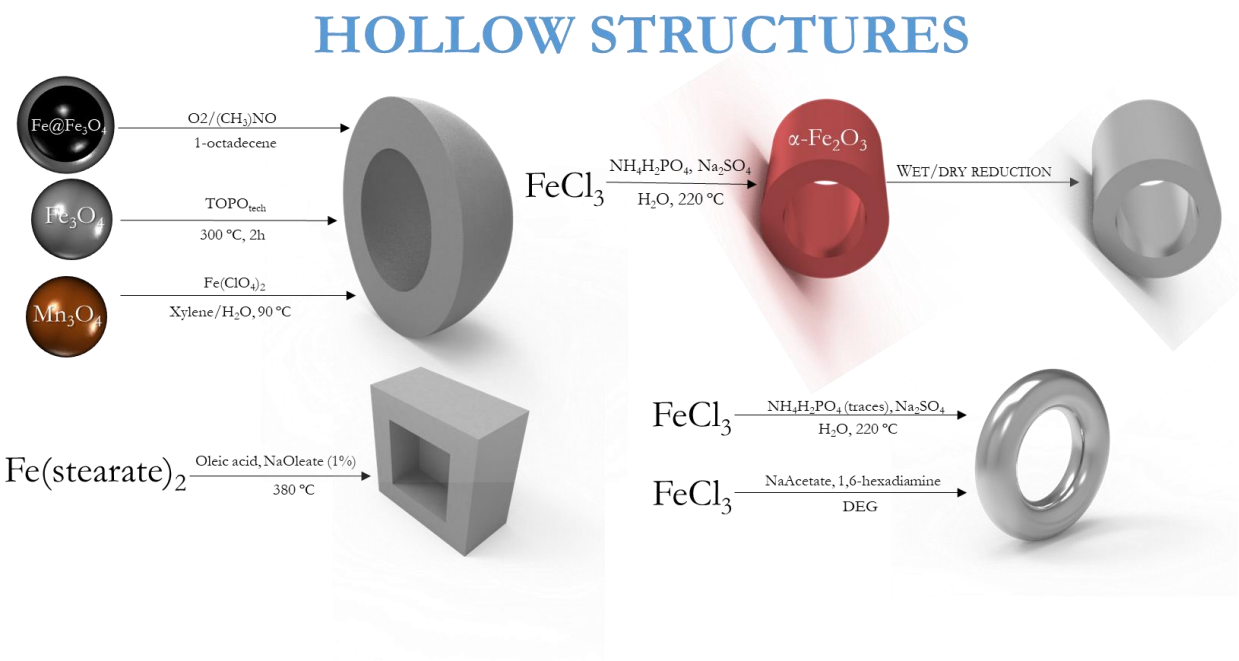

Fig. 10. Scheme of the synthesis routes for the growth of hollow Fe_3O_4 nanostructures (nanospheres, nanoframes, nanotubes and nanorings).

Another approach using the same template Fe/Fe_3O_4 is to induce a corrosion by the generation of a Molten salt derived sodium oleate.[149] The decomposition of iron(II) stearate in the presence of oleic acid with the addition of 1% of sodium oleate at 380 ºC generates 21 nm

hollow magnetite nanocubes. At high temperatures, sodium oleate decomposes and Na reacts with O_2 and H_2O forming Na_2O and NaOH[150,151] which are responsible for the continuous etching of Fe nanoparticles. It is noteworthy that only Fe {110} facets undergo prominent etching maybe due to absorption or underpotential deposition of Na species on this facet. Changing the amount of oleic acid and the heating rate seems to be crucial to grow hollow Fe_3O_4 with different sizes (15-50 nm) and shapes (**hollow stars**).

Sacrificial templates can be made of metal oxides different from the previously described iron ones (Fig. 10). This approach has the advantage that at intermediates stages of the reaction hollow bi-phasic metal oxide nanoparticles can be achieved. For example, 21 nm Mn_3O_4 nanoparticles can be used as seeds for the deposition of γ-Fe_2O_3 (Fig. 10). The mixture of Mn_3O_4 in xylene with a solution of iron(II) perchlorate at 90 ºC triggers a galvanic reaction[152] through the xylene-water interface where iron(II) cations oxidize to iron(III) and manganese(III) species reduces to manganese(II) which are dissolved leading to opposite diffusion of electrons (inward) and manganese(II) (outward) through the pin holes created at the interface. At the end of the reaction, all the Mn_3O_4 is dissolved and 23 nm γ-Fe_2O_3 remains. Moreover, a more simple version of this approach using MnO/Mn_3O_4 core/shell nanoparticles and trimethylamine N-oxide instead of water in an all-organic environment also leads to hollow γ-Fe_2O_3 nanoparticles at the end of the galvanic reaction.[153]

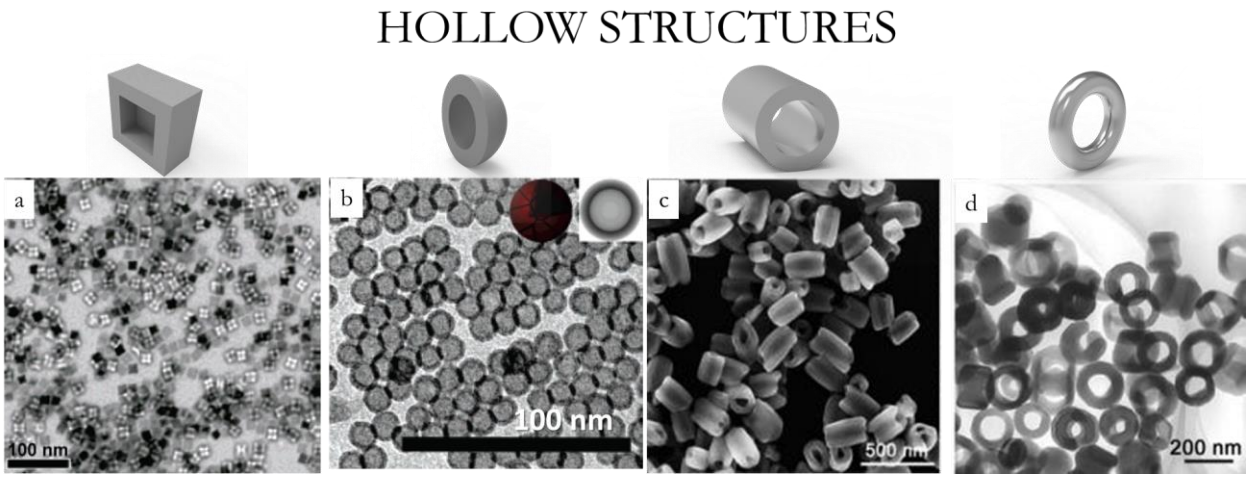

Fig. 11. Transmission electron and scanning electron microscopy (TEM/SEM) images of diverse hollow nanostructures and their ideal representations; a) Nanocubes: Adapted/reprinted with permission from [149]. Copyright (2007) American Chemical Society; b) Nanospheres; Adapted/reprinted with permission from [146]. Copyright (2007) American Chemical Society; c) Nanotubes; Adapted/reprinted with permission from [154]. Copyright (2008) American Chemical Society; d) Nanorings. Adapted/reprinted with permission from [154]. Copyright (2008) American Chemical Society.

It is worth mentioning that hollowing process can be achieved with the electron beam of the electron microscope. Poor crystalline Fe/Fe_3O_4 particles derived from the decomposition of iron(0) pentacarbonyl in a mixture of TOPO and hexadecylamine leads to hollow particles once exposed to the electron beam for 2 minutes. It seems that the beam creates a quasi-melting state were Fe atoms diffuse and voids coalesce creating a single void to minimize the surface area.[155] Thus, a poor crystalline structure with lots of defects is the origin of this carving effect. Moreover, an excess of oleylamine in Fe/Fe_3O_4 nanoparticles also creates hollow particles.[156] In this case an increase from 14.5 to 17 nm is achieved in the final particles with near 4 nm of thickness.

Fe_3O_4 nanorings and nanotubes can be achieved using hematite (α-Fe_2O_3) as sacrificial template. The hydrolysis of iron(III) chloride in water with the presence of $NH_4H_2PO_4$ and Na_2SO_4 carried out under hydrothermal conditions at 220 ºC for several hours leads to α-Fe_2O_3 nanotubes with a height up to 250 nm and diameters up to 170 nm.[154,157] In a second step, α-Fe_2O_3 nanotubes can be transformed to Fe_3O_4 by annealing at 360 ºC under a mixture of H_2 and Ar flow. The mechanism of the reaction can be understood as a coordination-assisted dissolution process. In the first stage of the reaction phosphate groups induce an anisotropic growth through the [001] axis because of the selective binding to (100) and (110) facets. In the case of sulphate groups, their affinity to Fe is much weaker than phosphates so do not play a key role. However, at some point in the reaction, a dissolution of α-Fe_2O_3 tips towards the interior until hollow tubes are formed. In this stage, sulphate ions play a key role assisting the dissolution. Tips have a high surface energy and are easily attacked by the protons in acidic solution (pH 1.8 is reached due to the chloride ions from the Fe precursor). By changing the ratio between phosphate and sulphate ions it is possible to tailor the aspect ratio of the nanotubes, reaching a nanoring structure when the concentration of phosphate ions is low. Interestingly, Fe_3O_4 nanorings between 15 and 50 nm can be also obtained in one step through the hydrolysis of iron(III) chloride in ethyleneglycol in the presence of sodium acetate and 1,6-hexadiamine under solvothermal conditions at 200 ºC.[158]

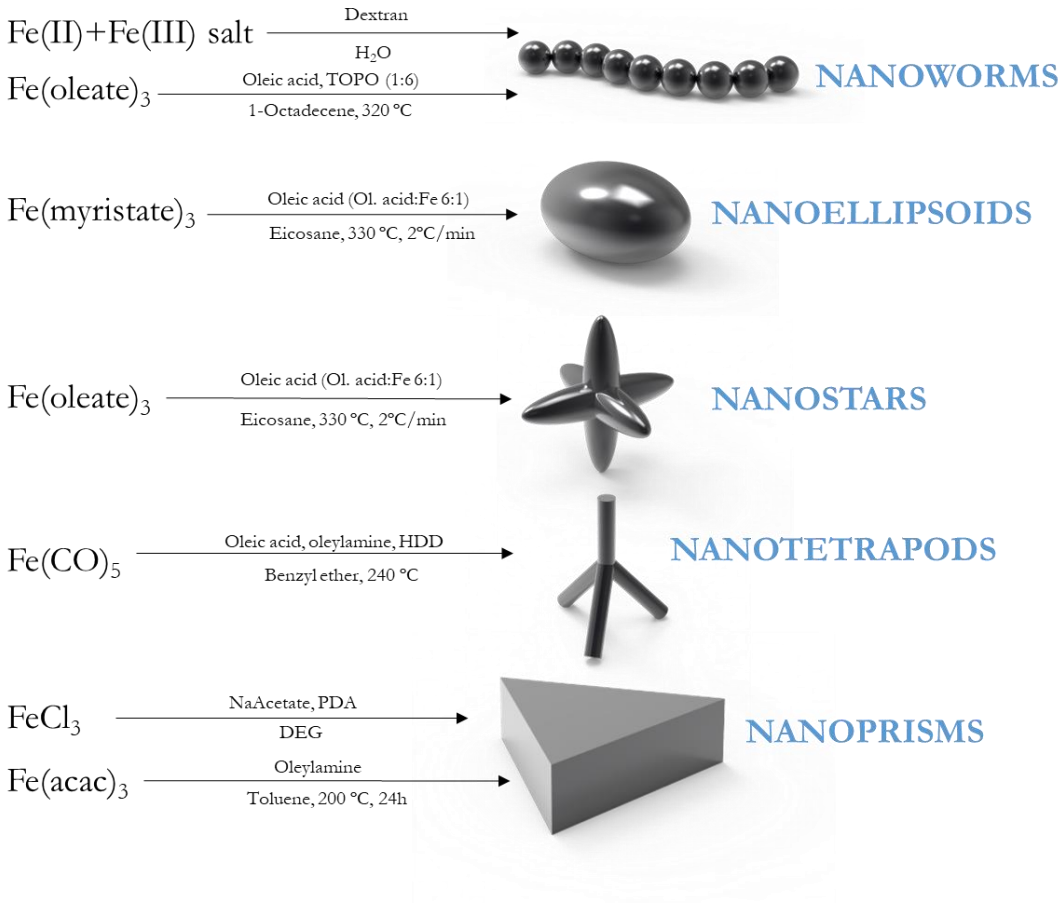

Fig. 12. Scheme of the synthesis routes for the generation of magnetite nanoworms, nanoellipsoids, nanostars, tetrapods and nanoprisms.

Apart from hollow morphologies, there are several shapes which have been growth occasionally under extreme synthetic conditions (Fig. 12). For example, **Fe_3O_4 nanoworms** can be synthesized by coprecipitation of high–concentrated solutions of iron(II) and iron(III) salts in water in the presence of dextran (Mw~20 kDa). These worms can reach a length of 50 nm as a result of the string of 5 nm spheres. When higher molecular weight dextran was used, multibranched structures with a size of 100 nm were grown.[159] An alternative to grow Fe_3O_4 nanoworms [160] using thermal decomposition approach can be accomplished decomposing iron(III) oleate in 1-octadecene with a mixture of oleic acid and TOPO (molar ratio~ 1:6) at 320 ºC for 5 hours. The final nanoworms could reach a final length of 200 nm from the aggregation of spherical particles. This aggregation was possible because of the presence of weakly-bound TOPO on the iron oxide surfaces.

Fe_3O_4 nanostars with 50 nm branches can be accomplished through the decomposition of iron(III) oleate in eicosane in the presence of oleic acid with a slow heating rate (2 ºC·min^{-1}) and a final reflux temperature of 350 ºC.[161] The key point for achieving a star-shape morphology relies

on the oleic acid:Fe ratio, which is extremely high (6), i.e. around the threshold to get nanoparticles. Authors justify this shape due to an uneven growth of nanoparticles around the nuclei because of the large concentration of oleic acid adsorbed in the nanoparticle surface. Using higher oleic acid:Fe ratios does not lead to nanoparticles because the oleic acid solubilizes the Fe precursor inhibiting the nucleation. Interestingly, **Fe_3O_4 ellipsoids** can be grown following the same synthetic route but using iron(III) myristate instead of iron(III) oleate**.**

Multribranched **Fe_3O_4 tetrapods** with sizes between 3 and 30 nm in length and a fixed diameter around 3-3.5 nm can be grown by slowly heating iron(0) pentacarbonyl in 1-octadecene in the presence of a ligand mixture composed by oleic acid, oleylamine and 1,2 hexadecanediol (in a molar ratio 3:3:5) at temperatures below 240 ºC.[162] The length can be modulated with the amount of iron(0) pentacarbonyl and the number of branches can be modulated with the amount of oleic acid.

Fe_3O_4 nanoprisms can be synthesized through the hydrolysis of iron(III) chloride in the presence of sodium acetate, 1,3-propanediamine (PDA) and ethyleneglycol (EG).[163] EG/PDA ratio are the key parameters to determine the final size and morphology. Fe_3O_4 nanoprisms with edges between 50 and 70 nm and thickness with 15-20 nm can be synthesized using a mixture EG/PDA=20 mL/2mL. However, an EG/PDA mixture of 35 mL/5mL leads to Fe_3O_4 octahedrons. Another synthetic route using organic solvent lies on the decomposition of iron(III) acetylacetonate in toluene with the presence of oleylamine at 200 ºC for 24 hours.[164] The oleylamine controls the anisotropic growth of the nanocrystals to the final nanoprism shape and the molar ratio between the oleylamine and the Fe precursor (15:1) leads to 22 nm nanoprisms in lateral size with 10 nm in thickness.

3. Ligands

The synthesis of monodisperse size and shape-controlled particles requires the separation in time of nucleation and growth stages as previously mentioned and it has been the subject of numerous works (Fig. 13). [17,26,27,31,42,165–173] Ligands (often called capping agents/molecules/stabilizers/adsorbates) play a key role in all the stages of the synthesis process. Ligands compile the group of small molecules, surfactants or polymers with functional groups that coordinate to metal cations through covalent-coordinating bonds donating electrons to the electron-poor metal atoms or by simple chemisorption. Some examples of ligands are surfactants such as carboxylic acids (oleic acid, decanoic acid), amines (oleylamine, dodecylamine, quaternary ammonium salts), phosphines (TOP, TOPO) or polymers (dextran, PVP).

Prior nucleation, ligands are responsible for solubilizing the cations forming metal complexes or metal hydroxides often referred as "monomers", "reactive species" or "solute" in the bibliography, stabilizing the oxidation state of the cation and preventing them from undesired or earlier nucleation. Some examples regarding the formation of these monomers are i) the decomposition of unstable precursors such as iron pentacarbonyl in the presence of ligands such as oleic acid, which forms a Fe-oleic acid complex, soluble in organic media that delays nucleation [30], ii) redox reactions that will determine the iron oxide phase,[174] iii) hydrolysis of iron salts in alkaline media leading to polycations hydroxides involved in the formation of akaganeite, goethite or hematite [175] and iv) alkolysis in organic polar media such as the formation of Fe-alkoxide in glycol that gives rise to the formation of 3D nanoflowers.[132] The concentration of these monomers increases by the sudden or progressive change of a physicochemical parameter (mainly temperature or pH) leading to nucleation when its concentration overcomes the supersaturation limit. At that moment, the monomer concentration is depleted. (Fig.13).

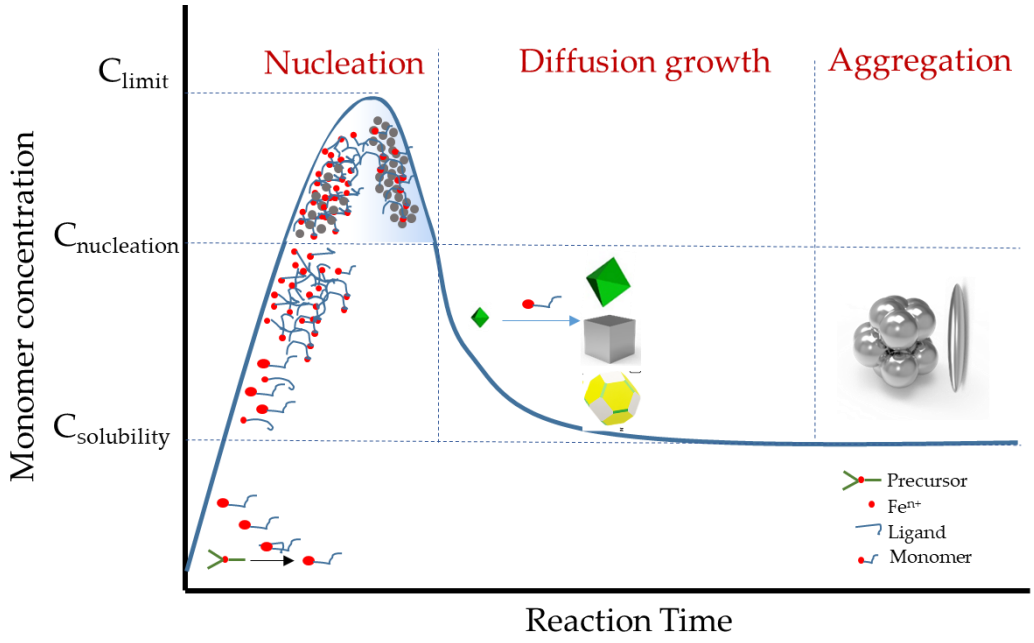

Fig. 13. Formation mechanism of some anisometric nanoparticles in solution. Adapted with permission from [176]. Copyright (1950) American Chemical Society.

Once the nuclei are formed, ligands still have a key role in regulating the growth of the particles their shape evolution, and stabilizing the particles in solution. The absence of ligands leads to an uncontrolled growth achieving large and irregular particles in order to diminish the surface energy. Ligands dynamically adsorb on certain facets by interaction with the particle surface cations decreasing their surface energy. The growth rate along this direction is reduced or inhibited so other growth directions are favoured. The fact that certain ligands only bind to certain facets depends on

the characteristics of the facets (e.g. atom, density of atoms and charge) (Fig. 13) and the functional groups that adsorbs or coordinates (functional group, type of electron-donor, type coordination).[167]

It should be taken into account that the growth rate of the different facets is exponentially proportional to its surface energy (Wulff construction model).[177]In the case of magnetite nanocrystals, the primary nuclei have octahedral morphology as it is the structure with less surface

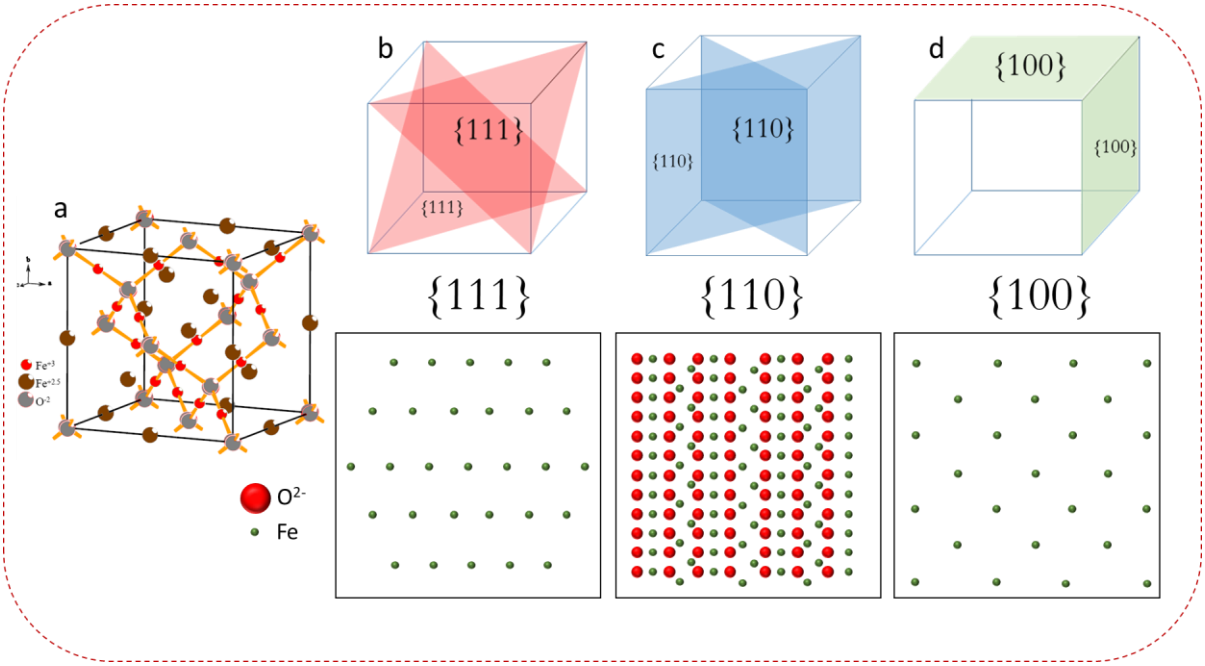

Fig. 14. a) Crystal structure of magnetite. Atomic configuration of low-index facets for cubic crystal systems, b) {111}, c){110} and d){100}. Adapted with permission from [97]. ©2010, by The Royal Society of Chemistry.

energy (octahedrons expose (111) facets, which have less surface energy) (Fig. 13 and 14). Cubic symmetry favours isotropic nanostructures whereas anisometric morphologies are favoured for nuclei presenting monoclinic, orthorhombic or hexagonal crystal structures.[167] It is known that for cubic crystals, the (100) facets are more energetic than (110) and (111) so its growth rate is faster. Then, the key factor to modulate the crystal shape is modulating the growth rate between [100] and [111] direction, so faster growth of [111] direction over [100] leads to the exposure of (100) facets, i.e. cubic shape nanoparticles (Figure 13).[93] Conversely, if the growth is faster on [100] direction over [111] leads to octahedral particles. In general, the faces with more energy are always the ones perpendicular to the longest axis so the growth rate is much faster along the longest axis.[178] As it was mentioned, the use of specific ligands which selectively binds to specific facets is an effective strategy for achieving the target morphology. The effect of the nature and concentration of the ligands on the morphology of magnetite nanoparticles are summarized in **Tables 1-2**.

Finally, the growth regime of the reaction given by the temperature and the monomer concentration are also important parameters to control the shape of the nanoparticles (Fig. 16).[179,180]. Low monomer concentration and high temperatures favours thermodynamic regimes that lead to isotropic structures. However, high flux of monomers and low temperatures are associated with kinetically controlled regimes that favour the growth of anisometric nanostructures.

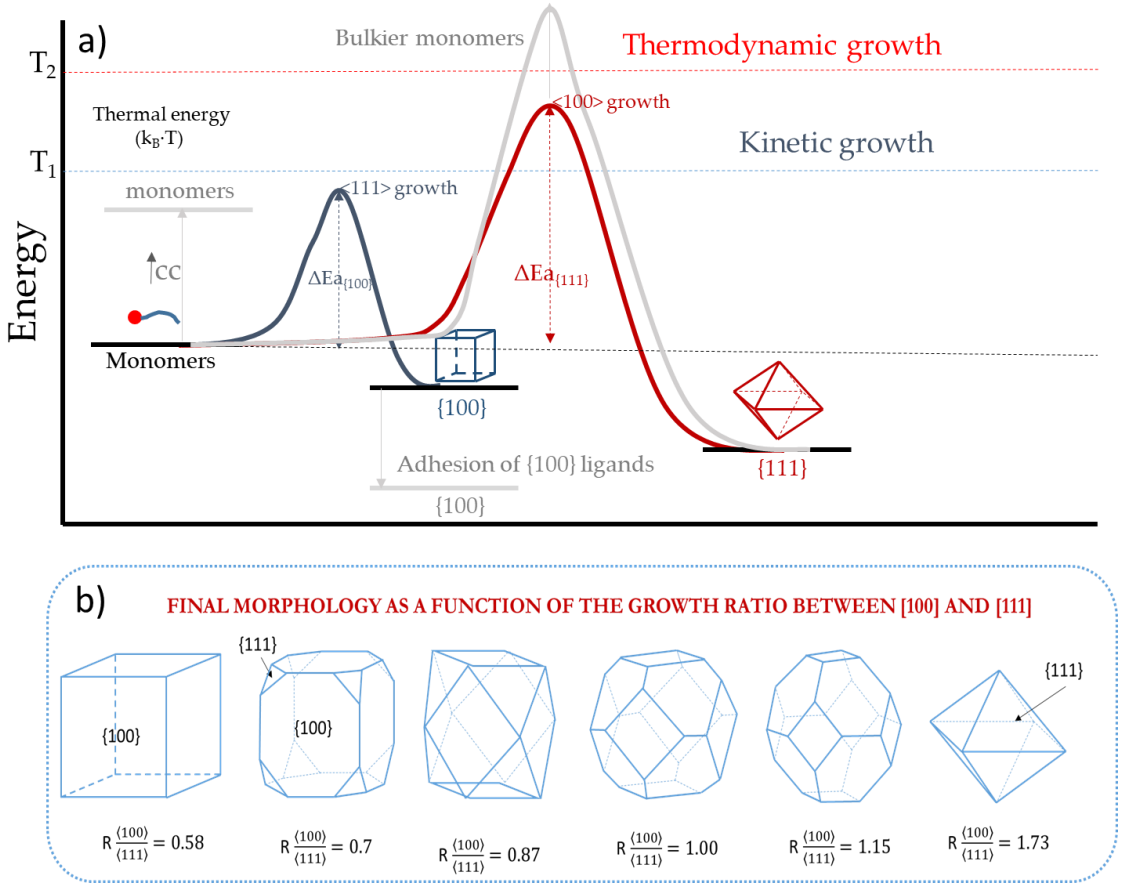

Fig. 15. a) Growth regime of nanoparticles with cubic symmetry and final morphology as a function of the different reaction parameters; b) Final morphology of the nanoparticles as a function of R (ratio between the growth rate along the [100] and the [111] direction). Adapted with permission from [97]. ©2010, by The Royal Society of Chemistry.

3.1. Tips for cubic-shaped nanoparticles

There are two main strategies to grow **cubic nanoparticles**. The first one deals with the manipulation of the reaction conditions, changing the concentration of precursors, reflux time, surfactant/precursor ratio and heating rate. The second deals with the use of **ligands with specific affinity to the selected facets (100)** such as **sodium oleate, decanoic acid, TOPO or chloride ions** which lower their surface energy promoting growth along [111] direction. However, these strategies work only in certain conditionsand keeping the ligands in relative low concentration

(otherwise the ligand will saturate the facets with more affinity and link to others). In the case of sodium oleate, undesirable phases such as FeO (wüstite) can be generated as it will be detailed in the Structural Properties Section (Section 4.1). Larger sizes up to 180 nm can be achieved in organic media using **low heating rates** (0.8 ºC·min^{-1}), **high concentrations of Fe precursor** (0.3 M) and **low surfactant/precursor ratio** (~2).

Using aqueous routes (precipitation in aqueous media), a **quasi-stoichiometric ratio** between **$FeSO_4$** and the **base** leads to 170 nm particles grown by **aggregation mechanism**. On the other side, the achievement of small cubic particles around down to 6.5 nm can be performed using **high heating rates** (20-35 ºC·min^{-1}), **high surfactant/Fe ratios** (around 5 or 6), **short refluxing times** (10-20 minutes) or lo**w Fe precursor concentrations** (0.044 M). Interestingly, it has been observed that **lineal carboxylic acids** such as decanoic and 4-diphenyl carboxylic acid act as inhibitors leading to a reduction of the final particle size.

3.2. Tips for elongated nanoparticles

For **elongated nanoparticles,** the growth mechanism depends on the solvent and/or the precursors involved. In aqueous media, the growth of elongated particles takes place by the aggregation of primary particles using an iron oxide or oxohydroxide intermediate thatacts as shape-template. When **hematite (α-Fe_2O_3)** was used as shape template, particle size can be controlled with the **nature** and **concentration of the iron(III) salt**, the **concentration of phosphate ions** that promotes elongated growth through c-axis achieving ellipsoidal shapes, the **addition of urea** and the **aging time that promotes the formation** of smaller or larger α-Fe_2O_3 nanoparticles, respectively. For example nanoparticles of around 600 nm in length with 80 nm in diameter can be achieved by using high concentrations of $KH_2PO_4$and large ageing times, with aspect ratios up to 10. The addition of urea leads to the formation of around 300 x 60 nm particles.Smaller hematite particles could be achieved by using **low amounts of phosphate ions** and **short aging times** reaching sizes down to 95 nm with aspect ratios of 2.

When using **goethite (α-FeOOH)** as shape template particles lengths between 300-60 nm and diameters between 25-10 nm can be achieved showing aspect ratios between 10-6. The OH/Fe ratio in the first oxidation stage**, the Fe(II) salt concentration** and the **carbonate or sodium hydroxide concentration** in the second stage seem to be critical for tailoring the final size. In the case of **akaganeite (β-FeOOH) nanoparticles**, the **concentration of iron(III) chloride** should be higher than **0.1 M**. Large elongated particles up to 500 nm in length and 50 nm in diameter (aspect ratio=10) can be synthesized at **high temperatures (100 ºC)** with an **aging time of 24 hours**.

Strategies to decrease the nanoparticles size include **lowering the concentration of Fe(III) chloride to 0.1 M**, the **inclusion of polyethylene imine** in the reaction (acting as inhibitor), **the reduction of ageing times** (few hours) and the increase of the pH by adding NH_4OH. These strategies allow lower the dimensions to 30 nm in length and 4 nm in width (aspect ratio around 7).

Table 1
Role of different ligands as a function of the reaction conditions to reach the target morphology

Shape	Iron precursor	Solvent polarity	Ligand	Comments
Spherical	$Fe(CO)_5$/ $Fe(oleate)_3$	Organic apolar media	Oleic acid	Under thermodynamic regime.[74,77]
	$Fe(acac)_3$		Oleic acid/oleylamine	In coordinated solvents [76]
	$Fe(acac)_3$		Oleylamine	In excess in the reaction [181]
Cubic	$Fe(oleate)_3$	Organic apolar media	Na(K)-Oleate	Binds selectively to (100) facets[92]
	$Fe(oleate)_3$		Chloride, bromide	Stabilizes (100) facets[97]
	$Fe(acac)_3$		Oleic acid	High supply of monomers (kinetic regime)[88]
	$Fe(acac)_3$		Decanoic acid	Preference binding to (100) facets. Used as growth inhibitor [89]
	$Fe(acac)_3$		4-biphenylcarboxylic acid	Preference binding to (100) facets. Used as growth inhibitor [88]
	$Fe(acac)_3$		TOPO	As impurity, it selectively binds to (100) facets [96]
Octahedra	$Fe(oleate)_3$	Organic apolar media	Quaternary ammonium salts	Generation of TOA cations which selective binding to (111) facets [100]
	$Fe(acac)_3$		Oleylamine	In nearly equimolar ratios to precursor, binds selectively to (111)facets [99]
	$Fe(acac)_3$		Oleic acid/oleylamine 1:1 mixture	In excess leads to truncated octahedral [182]
Elongated	$FeCl_3$	Aqueous	Sodium (potassium) dihydrogen phosphate	C-axis growths due to selective binding on (110) & (100) facets [36,108]
	$Fe(ClO_4)_3$		Urea	Source of OH^- ions. Favours c-axis growth (α-Fe_2O_3) [122]
	$FeSO_4$		Sodium carbonate	C-axis growths due to selective binding on goethite (001) facets [111]
	$FeSO_4$		Polyethyleneimine	Specific adhesion on lateral planes, inhibits growth [115,116]
	$FeSO_4$		Sodium acetate (NaAc)	Allows growth on [001] direction [112]
	$Fe(CO)_5$	Organic apolar media	Hexadecylamine/oleic acid	Generates water through condensation and hydrolyses Iron(0)-oleic complex.[183]
	$Fe(oleate)_3$		TOPO	Weak binding to nanoparticles, easy to remove [110]
	$Fe(CO)_5$		DDAB	Strong binding to central region leading to coalescence & growth of Fe edge particles [123]
	$Fe(oleate)_3$		Oleic acid	Induces elongated nanostructures when heating at 150 ºC [110]
Disk	$FeCl_3$	Aqueous	Sodium acetate (NaAc) Ethanol	C-axis growths due to specific adsorption on (0001) hematite facets [126]
Flower	$Fe(CO)_5$	Organic apolar media	Oleylamine	At low concentrations cannot prevent agglomeration due to incomplete capping [142]
	FeO(OH)		L-arginine monohydrochloride	Chloride ions are critical for the formation of flowers [143]
	$Fe(oleate)_3$		TOPO	At high concentrations induces a burst nucleation at 290 ºC and aggregates [129]

In organic media, using iron(III) oleate or iron(0) pentacarbonyl, the mechanism seems to be much more complex. Briefly the growth is carried out by diffusion of iron oleic complex to iron oxide nuclei previously formed. Largest particles can be achieved by **increasing the reaction time at 200 ºC** (avoiding the total decomposition of the iron oleic complex), the **amount of hexadecylamine** or the volume of the reaction up to 80 % inside the reactor (solvothermal approach). Under these conditions, sizes up to 140 nm x 12 nm can be achieved. On the other side, lowering the filling percentage of the reaction vessel down to 50%**, lowering the amount of hexadecylamine** and the temperature of reaction leads to nanowhiskers of 20 x 2 nm.

3.3. Tips for disk-shaped nanoparticles

The growth of Fe_3O_4 disk shape nanoparticles occurs through reduction of previously synthesized α-Fe_2O_3 nanoparticles with the target morphology, which is achieved under hydrolysis of iron(III) chloride in a mixture of water/ethanol with the presence of sodium acetate. The growth of hematite takes place by diffusion of amorphous ferric hydroxide ions onto hematite initial nuclei. The amount of **water, the polarity of the alcohol and the presence of sodium acetate** seem to be critical to control the diameter and thickness of the nanodisks that can grow up to 400 x 8 nm. Low aspect ratios (thickness/diameter) are **favoured using a poor mixture of water in ethanol and large amounts of sodium acetate**. Large aspect ratios (thickness/diameter) are favoured with water, minimum amounts of sodium acetate and using alcohol with high polarity. These conditions allow reaching structures of 40 nm x 40 nm in size.

3.4. Tips for flower-like nanoparticles

With the **polyol method**, the flower-like structures grow by aggregation of primary particles in the presence of **N-methyldiethanolamine (NMDEA)** mixed with **ethylene glycol**. For the growth of large aggregate size particles, it is interesting to use a solvent mixture of EG and NMDEA with a larger proportion of the last one, over stoichiometric amounts of NaOH, heating steps instead of continuous heating and adding water at the beginning of the reaction. The size of the aggregates can be up to 55 nm formed by cores of 11 nm. However, small aggregates can be achieved with low ageing times, under stoichiometric amount of NaOH.

Flowers synthesized in organic media through thermal decomposition lead to small aggregates ranging from 17 to 40 nm always composed of small particles of around 5 nm. The smallest aggregate size was achieved using an **equimolar amount of oleylamine** with **iron pentacarbonyl** while the **largest ones** were synthesized with **iron(III) oleate** using **L-arginine monohydrochloride**

3.5. Tips for other morphologies

Hollow nanoparticles always require special and, in some cases, extreme conditions to carve the particle. Some examples are the generation of **nanoframes** and **hollow spheres**. In the case of **nanoframes**, a reaction temperature of 380 ºC is needed to decompose sodium oleate and the sodium acts as a Molten salt. In the case of **hollow spheres**, inducing Kirkendall effect on oxidizable Fe nanoparticles (Fe/Fe_3O_4) by passing/generating O_2 *in situ* leads to an inward diffusion of oxygen and outward diffusion of the iron cations.

Nanostars are formed at high oleic acid:Fe ratios, just below the limit of nucleation because if oleic acid is present in a big excess, it solubilizes the monomers and inhibits the nucleation of the particles. **Nanoworms** are formed by oriented attachment of small primary particles where the growth by diffusion was not possible because of the strong binding of certain ligands such as TOPO or the effect of bulky ligands like dextran, who drives the oriented attachment to form the nanoworm morphology.

Table 2
Role of different ligands reach hollow, star, tetrapods, prime and worm nanoparticles.

Shape	Iron precursor	Solvent polarity	Ligand	Comments
Hollows	$Fe(CO)_5$	Organic apolar media	Trimethylamine N-oxide	Generates O_2 from decomposition at high T and induce hollow structures by Kirkendall effect[147]
	$Fe(oleate)_2$		Sodium oleate	Corrosion by Molten salts derived from decomposition at high temperature [149]
	$Fe(oleate)_3$		TOPO	Coordinates to outer Fe cations, dissolves them and induces an outward flow of Fe and an inward flow of O and P [145]
	$FeCl_3$	Aqueous media	Ammonium dihydrogen phosphate	Induces anisotropic growth of hematite along [001]. Selective binding to (100), (110) and (012) facets of α-Fe_2O_3 [157]
	$FeCl_3$		Sodium sulphate	Coordinates and dissolves the edges of the α-Fe_2O_3. Leads to smaller nanotubes [154]
Star	$Fe(acac)_3$	Organic apolar media	Oleic acid	At high ligand:precursor ratio.[162]
Tetrapods	$Fe(CO)_5$	Organic apolar media	Oleic acid-oleylamine-hexadecanediol	At T<240 ºC acts as templating for anisotropic growth [162]
Prisme	$Fe(acac)_3$	Organic apolar media	Dodecylamine (DDA)	At low DDA concentrations, binds selectively to (111) facets.[102]
	$FeCl_3$		Sodium acetate (NaAc)	Binds to (001) facets inhibiting the growth [126]
	$FeCl_3$	Organic polar media	1,3-propanediamine (PDA)	Induces octahedral shapes by stabilization of the (111) EG[163]
			Ethylenglycol	Induces flat shapes together with NaAc under hydrothermal conditions.[163]
Worms	$Fe(oleate)_3$	Organic apolar media	TOPO	Excess of TOPO leads to aggregation of small spheres due to weak binding of TOPO at 320 ºC[160]

4. Properties

4.1. Structural properties

The nanocrystal structure is determined by the synthesis route chosen and the growth mechanism. There are different techniques that allow the examination of the nanocrystal structure. One is the scanning and transmission electron microscopy (SEM, TEM), including dark field imaging, high resolution TEM (HRTEM) and related fast Fourier transformation (FFT). They provide local valuable information for the evaluation of the crystallinity, crystal morphology, symmetry and the crystallographic axes in anisometric nanoparticles. In addition, X-ray diffraction provides an overall characterisation of the crystal structure of the sample and statistical measurements. Other interesting techniques such as Infrared and Raman spectroscopy for analysing surface bonds, and Mossbauer spectroscopy, especially interesting for Fe compounds, for determining the iron state, will not be discussed in this review.

Nanocubes are formed by the faster growth of the particles along the [111] direction over the [100] leading to surfaces composed of (100) facets in the case of perfect nanocubes (Fig. 15). This can be corroborated by the observation of (400) lattice fringes lying parallel to the edge of the cube by HRTEM.[184] Moreover, it is also common to identify the (220) and (111) planes, which are disposed in diagonal within the nanocube.[92,96,97,185] Interestingly, when forming a superlattice, the (220) and (440) XRD peaks show an enhanced intensity with respect to the bulk ones and the (311) decreases because each nanocube has a preferred crystal orientation with [110] planes parallel to the substrate.[90]

Particular attention deserves the structure of Fe_3O_4 nanocrystals synthesized from Fe(III) oleate in eicosane under the presence of oleic acid and sodium oleate [95,186]. In this particular case and due to the reducing atmosphere, magnetite is grown from wüstite through topotaxial growth over shared planes ((200) WÜSTITE //(400) MAGNETITE and (220) WÜSTITE //(440) MAGNETITE) of both iron oxide phases.[187,188] Magnetite grows in small subdomains with a high number of defects and antiphase boundaries. This high amount of dislocations created a high number of crystalline boundaries leading to the formation of a mosaic texture, which explains the limited structural coherence in the XRD patterns in comparison to those of pure magnetite structure synthesized by thermal decomposition. [189]

In the case of Fe_3O_4 nanocubes synthesized by a biogenic route trying to imitate the magnetosomes, their morphology can be described as pseudo-cubic, with (100) facets but also (110) typical from dodecahedron and (111) typical from octahedron (Fig. 16).[190] It has been observed

that the protein Mms6, located in the magnetosome membrane, modifies the crystal morphology from octahedral to cuboctahedral through stabilization of the (100) facets because the negatively-charged C-terminal domain strongly binds to iron and controls magnetite formation.[191–193]

Contrary to nanocubes**, octahedral particles** are formed from the faster growth on [100] direction leading to nanoparticles enclosed on eight (111) facets, which are the less energetic for face-cantered cubic systems. Typical family planes observed by HRTEM are (111), (-111) and (220).[99] The octahedrons can be slightly truncated exposing (110) facets and when forming self-assembled monolayers, they are supported by contacting two vertices of two adjacent nanoparticles in the first row. During thermal decomposition of iron pentacarbonyl, the addition of capping ligands such as dodecylamine (DDA) can tune the morphology of the crystals to diamond-like nanocrystals. In this case the nanocrystals grow along the [110] zone axis with separation angles of 70° and 90° between the planes, which is a dodecahedron truncated along the [111] and [100] directions.[102] Triangular nanocrystals are also achieved, showing (220) planes along the [111] zone axis, which points that it is a tetrahedron with highly truncated (111) facets.

Solvothermal process reported to directly synthesize **magnetite nanorods** using iron pentacarbonyl ($Fe(CO)_5$), oleic acid, and hexadecylamine exhibiting (222) and (311) planes by HRTEM of Fe_3O_4. The growth takes place along [110] axis (Fig. 16).[115] However, indirect methodologies lead to elongated structures with different growth directions (Fig. 16). The reported lattice spacing for magnetite rods coming from hematite reveals that the long axis is the [001] axis.[126] Interestingly, akaganeite (β-FeOOH) rods reduced to magnetite via wet reduction in trioctylamine exhibit an interplanar spacing of 0.20 nm along the long axis which reveals that the growth direction is the [311].[80] However, when akaganeite nanorods were reduced in the presence of hydrazine under microwave irradiation the growth direction of the long axis is parallel to the [001] direction.[194] Finally, magnetite elongated nanoparticles with spindle shape reduced from goethite, show that the (311) planes forms an angle of 30º with the longest axis [110].[79] A typical feature observed for elongated nanoparticles obtained by shape-templating from other oxides is the porosity that arises from the dehydration during the annealing at high temperatures to reach the target magnetic iron oxide. This porosity is important as it increases the surface area of the crystals and the pores act as nucleation points for the magnetization reversal.

In the case of **disks** and **nanoplates**, the final magnetite crystal properties depend on the hematite that acts as template for the final Fe_3O_4 disks/nanoplates. The study of hematite nanoplates by HRTEM and related FFT patterns reveals that the basal plane is the (001) (Fig. 16). [126] Magnetite disks, obtained after a hydrogen-wet method, confirm the single crystal nature of their

precursor, which has been shown independent from the reduction method (dry/wet) [79]. Moreover, the formation of pores randomly distributed has been observed in the magnetite structure for both types of reductions, which is associated to the formation of tunnels by the removal of oxygen. Magnetite is formed in the surrounding areas parallel to the tunnel generation.[195] The nanodisks obtained by this route possess (220) lateral planes and (111) planes in the basal surface.[196] It is noteworthy that the alignment of the nanodisks produces modification in the relative intensities of the X-ray diffraction pattern, in comparison with the standard Fe_3O_4, showing enhanced intensities for (111) and (222) peaks, whereas the intensities of (220), (400) and (440) were reduced.[125] Fe_3O_4/γ-Fe_2O_3 nanoplates obtained by solvothermal method and a post-reduction step in hydrazine, renders basal planes corresponding to (111) surfaces of a spinel-structured iron oxide hindering the growth along the [111] direction. [197] Besides, the flattening of the nanoplates was assigned to the (220) and (311) planes of γ-Fe_2O_3.[42] The authors claimed that in the Fe-terminated (111) surfaces of the nanoparticles, the absorption of PVP can take place due to its strongest polarity as it exposes alternated octahedral coordinated Fe^{3+} and O^{2-} layers so Fe^{3+} ions can interact with other functional groups. It was deduced that the adhesion of PVP to the (111) facets reduces the growth rate along the [111] direction.

Hollow iron oxide spheres obtained by Kirkendall effect of initial Fe/Fe oxide core/shell particles are polycrystalline with no preferential orientation of the individuals. [198] However, hollow nanoframes obtained by "molten salt corrosion" are oriented crystal aggregates and dissolution proceed in a certain direction, causing prominent etching only in (110) facets.[149] However, a different behaviour arises from the use of sacrificial templates of iron oxides. In the case of hematite nanorings synthesized by Ostwald ripening and subsequent oriented dissolution, their crystal structure and such oriented dissolution has attracted the attention of scientific community. It was reported that there is a preferential dissolution of the tip of the (100) plane (highest concentration of exposed Fe^{3+} ions) and then on (001) planes among the normal low index planes (Figure 16).[199] Usually, certain ions are used in order to form binuclear, bidentate complexes with iron, adhering on (110) and (100) surfaces and preventing the iron atoms to detach from the surfaces.

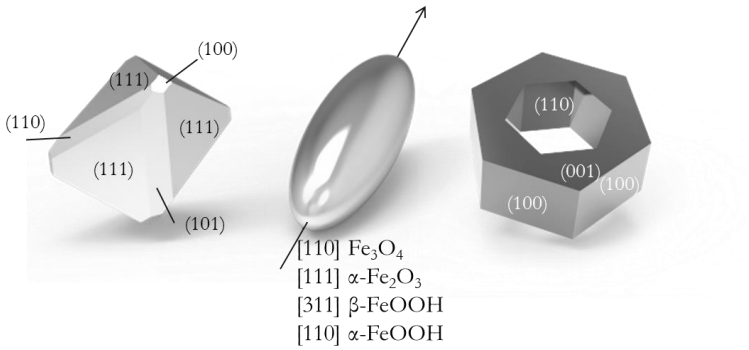

Fig. 16. Magnetite with hexa-octahedral crystal habit elongated along one of the <111> axes from the magnetotactic bacterium. Longest dimension of the elongated nanoparticles as a function of the precursors and crystal structure of the hexagonal nanorings.

Fe_3O_4 nanorings obtained after dry reduction in a furnace are single-crystal and present two crystallographic orientations ([111] and [112]) from respective lattice spacing of 0.48 and 0.29 nm in their basal plane. After the phase transformation, [001] α-Fe_2O_3 crystallographic direction transforms to [111] and [112] Fe_3O_4 direction, being the latter one observed directly by electron microscopy for the first time (Fig. 16).[154] Absorption spectroscopy on HRTEM revealed also that the Fe atoms are homogeneously distributed without change of valence. For the case of hollow rods, obtained from the direct transformation of hematite, a perfect single crystal structure is obtained. The reported lattice spacing for hematite rods is 0.253 nm, which corresponds to the (110) planes. SAED and HRTEM analyses have revealed that the nanorods grow along the <001> direction. After the phase transformation, [001] and [110] crystal directions of α-Fe_2O_3 leads to [111] and [311] in magnetite. Lastly, hollow structures obtained through galvanic replacement reactions in metal oxide nanocrystals showed that, in the case of Mn_3O_4 square prisms, whose top and side surfaces were enclosed by (001) and (100) facets, respectively, where transformed to **γ-Fe_2O_3 nanocages** with a hollow interior and holes and crystalline structure with highly ordered continuous lattice fringes in their shell.

N**anoflowers structure** critically depends on the synthesis process used that determines for example the degree of contact between cores within a particle. In fact if the continuity of the crystal orientation is ensured along the particle, magnetic ordering across the interfaces is favoured.[131] For one-step surfactant assisted hydrothermal process, the reported HRTEM analysis reveals that each particle behaves as a single crystal with spinel structure with similar crystalline orientation.[200,201] However, high temperature organic precursor decomposition with a second injection of TOPO and hexane produces nanoflowers composed of many small (5 nm) iron oxide

nanocrystals, causing a ring dot pattern of the FFT typical of polycrystals.[129] Polyol process in the presence of NMDEA allows obtaining nanoflowers composed of large cores (approximately 11 nm). This was clearly indicated by the Fourier transform of the HRTEM of monocrystalline nanoflowers, showing misalignments from 1 to 3° between the cores and defect holes, possibly containing traces of solvents used for the synthesis. Nevertheless, the authors claimed that 30% of the nanoflowers are still polycrystalline.[22] Lastly, self-assembled 3D flowerlike iron oxide nanostructures formed by the assembly of microspheres, caused a ring dot pattern of the FFT.[202]

Table 3

Magnetic properties of different iron oxide nanoparticles with cubic shape.

Author/year/reference	Length (nm)	Ms_{RT} ($emu \cdot g^{-1}$)	Hc_{RT} (Oe)	Hc_{5K} (Oe)
Guardia/2010 [203]	13	------	0	400
	45	------	50	200
	180	------	50	50
Yang&Ogawa/2008 [185]	6.5	39	------	190
	15	80	------	500
	30	83	100	790
Kovalenko/2007/[92]	7	29	0	------
Kim&Hyeon/2009 [88]	25	------	20	------
	50	------	75	------
	79	------	90	------
	100	------	110	------
	150	------	100	------
	170	------	113	------
Gao/2010 [96]	12	60.3	------	------
Moya/2015[204]	16	82	9	320
	50	90	82	327
	104	91	94	598
Pardo/2015[184]	27	------	------	333
	48	------	------	460
	94	------	------	609
Andres-Verges/2008[85]	30	83	50	------
	33	83	90	------
	45	87	80	------
	76	92	106	------
Vereda/2013 [205]	54	82	80	------
Nishio/2007 [206]	31	82	------	------
	40	88	------	------
	46	90	------	------
	102	92	------	------

4.2. Magnetic properties

In general, Fe_3O_4 nanocubes synthesized in organic media by thermal decomposition exhibit saturation magnetisation values (M_S) close to the bulk ones (M_S= 92 emu·g^{-1}) for sizes larger than 13 nm (Fig. 17, Table 3).[203] It has been observed that nanocubes saturate at much lower field (0.2 T) than spheres (1 T).[92] In the zero field cool/ field cool curves (ZFC/FC), it is also observed an important difference in the blocking temperature (T_B), being larger for spheres (235 K) than for nanocubes (190 K) and corroborated by Mossbauer spectroscopy. Surface anisotropy, enhanced for spheres, seems to be responsible for the different magnetic behaviour. [94] Size is another important factor governing the magnetic behaviour. Thus, 100 nm nanocubes exhibit coercivities around 110 and 600 Oe at room temperature and 5 K respectively.[184,204] Contrary to expected, coercivity increases for sizes larger than the monodomain. This is due to the formation of chain superstructures where the coercivity is proportional to the length of the chain and inverse to the separation between cube facets.[207,208] Moreover, Verwey transition is observed in the ZFC/FC curves for 16 nm Fe_3O_4 nanocubes prepared by thermal decomposition in organic media [204] but no for nanocubes of similar size (20 nm) synthesized in water using precipitation in alkaline media, in spite of having pure magnetite as demonstrated by Mossbauer spectroscopy.[85] However, magnetic properties in terms of M_S and H_C do not differ significantly (Table 3).

The magnetic properties of **elongated Fe_3O_4** or **γ-Fe_2O_3 nanoparticles** present special features respect to their spherical counterparts mainly due to the enhancement of the effective anisotropy as the shape term appears in addition to the magnetocrystalline one. This means that only two possible directions (along the largest dimension) are possible for the magnetic moment. In theory, it leads to an increase of the blocking temperature and coercivity of the particles. However, there are other factors such as the surface state or the existence of crystal defects or pores, determined by the synthesis approach and/or reduction strategy that should be taken into account. Magnetic properties of these anisometric particles and spheres with equivalent volumes, either Fe_3O_4 or γ-Fe_2O_3, have been compared (Table 4). For example, for Fe_3O_4 elongated nanoparticles synthesized in organic media by solvothermal route exhibit the Verwey transition (T_V) around 120 K, even for rods with small dimensions down to 41x7 nm (volume equivalent to a spherical particle

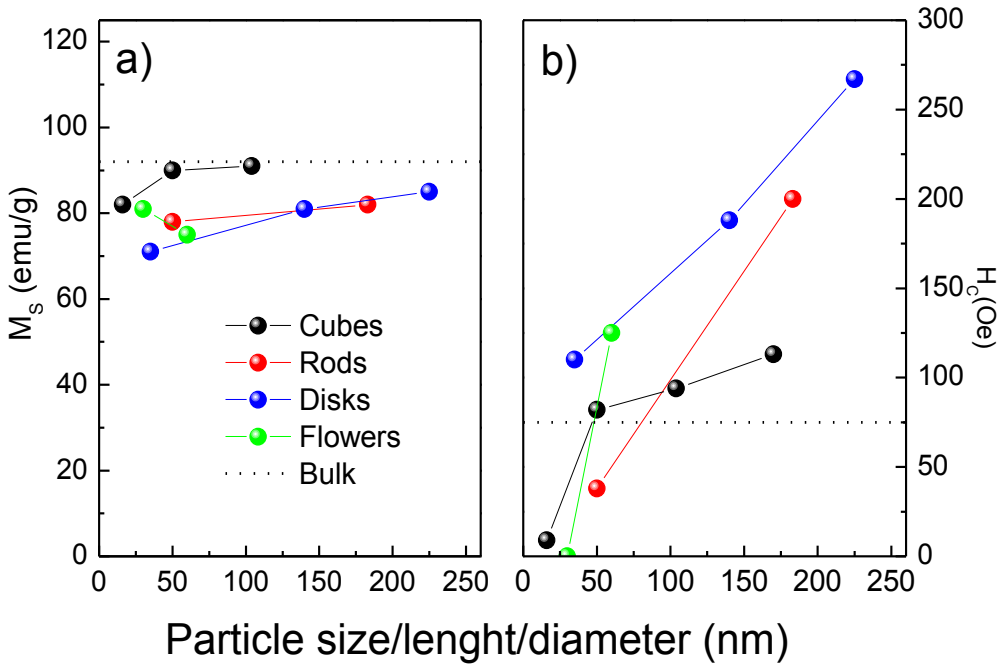

Fig. 17. Magnetic properties at room temperature of magnetite nanoparticles with different morphologies; a) Saturation magnetisation (M_S), and b) Coercive field (H_C) as a function of the particle size. Dot lines represents M_S and H_C of bulk magnetite taken from [48].

of around 14 nm).[124,209] The Verwey transition marks a structure change from cubic (above T_V) to monoclinic (below T_V) having a clear impact in their physical properties.[210] For spherical particles smaller than 30 nm is not common to observe the Verwey transition because of the surface spin canting, defects or lack of stoichiometry.[74,211]The presence of the Verwey transition is a clear sign of highly crystalline and stoichiometric magnetite.

Table 4.

Magnetic properties of different iron oxide nanoparticles with elongated shape. Spherical size means the diameter of a sphere with the same volume than the elongated particle

Reference	Length (nm)	Width (nm)	Aspect ratio	Spherical Size(nm)	M_{Srt} (emu/g)	Hc (Oe)
R. Das/2016 [124]	41	7	5.9	14.4	86	0
	65	6	10.8	15.2	84	0
	56	10	5.6	20.3	87	0
H.Sun/2012 [183]	63	6.5	9.7	15.8	20	46.5
Si/2014[212]	58	8	7.3	17.7	62.15	------
	250	64	3.9	115	62.15	------
Macher/2014[213]	20	2	10.0	5	25	0
Chandra/2017[209]	72	8	9.0	19	86	412
	72	8	9.0	19	86	412
Bomati/2008[118]	40	7	5.7	14.3	25	-------
	65	10	6.5	21.3	25	-------
	100	18	5.6	36	40	-------
	140	20	7.0	430	50	650
YJ. Chen/2009 [214]	1000	80	12.5	202	59	266
Wang/2010[215]	200	50	4.0	90	68	
Milosevic/2011[194]	38	12	3.2	20	18	55
Mohapatra/2015[115]	30	4	7.5	8.9	50	0
	40	6	6.7	12.9	54	0
	50	8	6.3	16.9	58	0
	60	10	6.0	20.8	63	0
	70	12	5.8	24.7	66	0
Geng/2016[80]	50	10	5.0	19	78	38
	400	40	10.0	98	--------	334
Lentijo/2017[116]	212	46	4.6	87	83	789(10K)
	21	5.7	3.7	10	69	497
	17	5	3.4	8.6	15	511
H. Gavilan/2017[79]	183	33	5.5	66	60	0
	183	33	5.5	66	82	200

A proof of their high crystallinity are the high M_S values (84-87 emu/g) for rods with dimensions larger than 40x7 nm,[124] which are close to the bulk one. It is also remarkable that blocking temperatures have not been found below 300 K, due to the effect of the dipolar interactions, which leads to a negligible coercivity at room temperature (0-50 Oe).[183] Interestingly, Fe_3O_4 rods (72x8 nm) grown epitaxially on $SrTiO_3$ substrate exhibit biaxial magnetic anisotropy with one order of magnitude between the hard and the easy axis.[209] Moreover, the T_V increased for the same rods when grew epitaxially on a substrate (120 K) than without substrate being the presence of antiphase boundaries the main responsible for the T_V shift to lower temperatures.[216] Different behaviour was observed for ultrathin nanorods (called nanowhiskers) of 20x2 nm grew by the hydrolysis of iron(III) oleate in the presence of oleylamine at 150 ºC.

Magnetization loops at room temperature show a paramagnetic component due to the high surface-to-volume ratio (around 2) and low crystallinity.[213]

When the synthetic route chosen to get Fe_3O_4 is *via* goethite or akaganeite, the nanostructures are not as well crystallized as their equivalents grown from hematite or by solvothermal method, and present pores. In general, M_S values range from 20 to 60 emu/g due to their surface spin disorder .[80,115,116,118,194,214,215] The smallest rods where the Verwey transition can be observed are 40x6 nm (equivalent to 13 nm spherical particles)[115] and it is more usual to observe the blocking temperatures in such nanostructures, contrary to the nanostructures synthesized by solvothermal method. Thus, blocking temperatures of 80 and 110 K were measured for 30x4 nm and 40x6 nm respectively[115] but for longer rods, the ZFC and FC do not converge showing ferromagnetism at room temperature and registering coercivity values up to 350 Oe at room temperature for 400x40 nm due to the large diameter of the nanostructures.[116] **Magnetite nanobelts** obtained by reduction of α-FeOOH of 50 nm in diameter and several μm of length exhibit a high M_S at 300 K (81emu/g) and a coercivity of 170 Oe.[109]

Nanoplates/disks/rings with diameters between 3-15 times larger than their thickness are reported to exhibit magnetic vortex structures (Fig. 18). In this configuration, the majority of the spins align circularly in plane forming a flux closure while the ones located at the centre are aligned out of plane leading to weak interacting structures without any stray field and with coercivities and remanent magnetizations close to zero being ideal for theranostic applications. The stabilization of this vortex depends on the diameter, the thickness and also the extension of the inner cavity in the case of nanorings.[125] Once an external field is applied, the magnetic vortex state can be transformed into another state, which depends on the morphology of the nanostructure. In the case of nanorings the hysteresis loop consists in a two-step process involving onion-vortex transition and vortex-reverse onion state (Fig. 19).[125,217] In nanodisks, the evolution is more complex. At zero field from a saturate state, there is a transition to c-state were the vortex core is located close to the edge of the particle. An increase of H leads to a shift of the vortex from the edge to the centre forming a vortex state in the particles. A further increase leads to a shift of the vortex to the opposite edge and finally the vortex disappears once the nanodisk is saturated. It is noteworthy that the vortex configuration is a

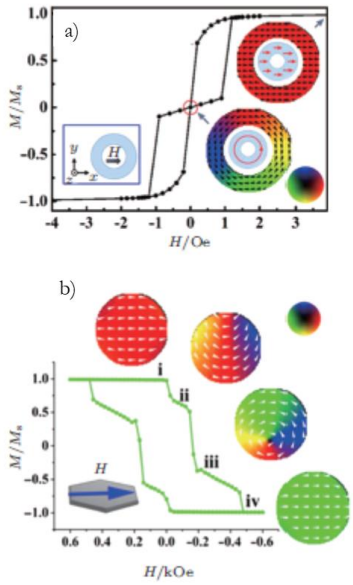

Fig.18. Magnetic stated during switching when field is parallel to, a) nanorings, reprinted with permission from [217], ©2012, by AIP Publishing; b)nanodisks. Cartoons are schematic diagrams of the domain structures. Reprinted with permission from [125], ©2015, by Wiley.

stable state in nanorings rather than in nanodisks. In the case of the nanoplates/disks, in spite of their large size, the saturation magnetization is below the bulk one (92 emu/g). Small nanoplates of 35 nm in diameter and aspect ratio 3 (equivalent diameter=27 nm) have a M_S of 71 emu/g. [128] On the contrary, large nanodisks with a diameter of 225 nm and an aspect ratio of 14, displays a M_S of 85 emu/g, much closer to the bulk one.[125] Differences in the M_S are given again by the structure of the oxide or oxohydroxide precursor and the further annealing which gives the final Fe_3O_4 phase. In all cases and spite of their magnetic configuration, plates and disks exhibit high values of H_C at room temperature. Coercivity ranges from 110 to 267 Oe for the 35 nm nanoplates and 225 nm nanodisks, following a linear trend with the size.[79,125,128]

Table 5. Magnetic properties of different iron oxide nanoparticles with disk/plate like morphology.

Author/year/eference	D (nm)	t (nm)	Aspect ratio	Spherical size (nm)	M_{SRT} (emu/g)	H_{CRT} (Oe)	H_{C5K} (Oe)
Lu/2009 [128]	35	11.5	3.04	27	71	110	------
Gavilan/2017[79]	140	22	6.36	86	81	188	628
Yang/2015[125]	225	16	14.06	125	85	267	490

Superferrimagnetism is the main property ascribed to **Fe_3O_4/γ-Fe_2O_3 nanoflowers,** which makes them ideal for biomedical applications, especially as hyperthermia and MRI contrast agents. Superferrimagnetism arises from the exchange interaction between the cores that are in close

contact within the particle. The remanent magnetization of these nanoflowers is weaker compared to single core particles with similar cluster size.[218] The other characteristic is that their saturation magnetization values are close to the bulk ones given by the use of high temperature synthesis routes that reduce the presence of spin disorders and canting. In all cases, the nanoflowers exhibit residual coercivities [219] or are superparamagnetic as a consequence of the super exchange interaction between the core within the particle and they have a very high magnetic moment per particle.

Magnetic properties of **hollow iron oxide nanoparticles** depend in a great extension of the hollowing procedure. For example, Fe_3O_4 nanoparticles, with at least 10 nm in size, etched with TOPO technical grade at 300 ºC, have experienced a dramatic change of their magnetic properties from superparamagnetic to paramagnetic. This change is due to the inward diffusion of P atoms on the nanoparticle leading to amorphous iron oxide. Another interesting feature is the loss of M_S from 50 to 3 emu/g.[145] For those iron oxide particles hollowed by using Kirkendall effect-based techniques using Fe nanoparticles/clusters as templates, the magnetic properties dramatically change, not only because of the phase change (from Fe to Fe_3O_4 to γ-Fe_2O_3) but also for the promotion of surface spin canting and the change to a polycrystalline nature of the particles.[148] Thus, saturation magnetization drops from 80 to 47.9 emu/g from solid 13 nm Fe/Fe_3O_4 nanoparticles to their equivalent 16 nm hollow Fe_3O_4 ones after oxidation with trimethylamine N-oxide. Moreover, these hollow structures were not able to saturate under a field of 1.5 T.[147]

An evidence of how important is the reduction method, α-FeOOH nanoparticles of 183x33 nm were subjected to both dry (treatment at high temperatures under hydrogen/argon gas) and wet (treatment at high temperature in organic media in the presence of oleic acid) treatments leading to Fe_3O_4 needles. In the case of the needles obtained by wet reduction, the M_S measured at 300 and 10 K were much lower (60 and 70 emu/g respectively) than the values obtained for the needles reduced by the dry method (82 and 90 emu/g).[79] Interestingly, for the sample obtained by wet reduction the histeresis loop presents a wasp-waisted shape with a negligible coercivity (observed at low sweeping field rate) due to the mixture of single and multidomain remanence states.[220] In the case of the needles obtained by dry reduction there are no sights of such behaviour probably due to the less pronounced defects and pores within the reduced needles.

In general, it can be concluded that magnetic properties of magnetite and maghemite nanoparticles are strongly dependent not only on the nanoparticle size and shape but also on the chosen synthesis route and, in particular, to the reduction conditions if other iron oxides/oxihydroxides have been chosen as shape templates. Thus, in the case of elongated

nanoparticles with sizes below 150 nm in length, they show coercivity values at room temperature similar to other morphologies probably due to incoherent magnetisation reversal process. Nanocubes exhibit higher M_S values than other morphologies and are closer to the bulk value (96 emu/g). On the other hand, the low coercivities and remanent magnetization values observed for nanoflowers are due to their superferrimagnetic behavior (Fig. 17). In theory, nanorings/disks exhibit lower coercivity due to their magnetic vortex structure but the reality shows that there are other factors such as the internal structure, defects and pores that also accounts for the final magnetic properties.

4.3. Nanotoxicity

Magnetite and maghemite nanoparticles have been proposed for biomedical applications and the main advantage they present over other magnetic compounds is their low toxicity. This is a consequence of the existence in the body of metabolic pathways able to deal with iron atoms.[221] Specialized proteins are able to store and transfer iron released from the nanoparticles during their degradation process. In fact, iron oxide and oxyhydroxide nanoparticles are currently being used as iron supplements. In addition, the Food and Drug Administration (FDA) of the USA has also approved iron oxides as contrast agents for magnetic resonance imaging (MRI).[222]

Generally, most of the studies evaluating the toxicity of iron oxide magnetic nanoparticles reinforce the idea of their low cytotoxicity, in spite of the difficulty comparing toxicity studies from the literature due to the lack of standardization (several iron concentrations, cell lines and assays are randomly used). The cytotoxic effects reveal for magnetite and maghemite, if any, are usually negligible or limited to extreme conditions such as very high doses (> 0.5 mg Fe/ml) or long exposure times (> 120 h).[223] However, in most cases only the decrease in cell viability is evaluated and other potential toxic effects (genetic or carcinogenic among others) are not generally studied. Likewise, no signs of additional toxicity have been found for the different anisometric nanoparticles in agreement with the observations reported for spherical ones.

In the case of 19 nm **nanocubes**, cytotoxicity using the Trypan Blue test has been tested in human adenocarcinoma cells (KB cells). Cell viability was decreased to 70 % when the cells were incubated with poly-(maleic anhydride alt-1-octadecene) coated nanoparticles (1 g/L, 24 h).[224] The same group studied the cell viability by the Alamar Blue assay with three malignant cell lines, SKOV3 (ovarian cancer), PC3 (prostate cancer), and A431 (epidermoid cancer) using 20 nm nanocubes, indicating the low toxicity of this material.[64] The degradation of similar sized nanocubes has also been followed *in vitro* (in SKOV3 ovarian and PC3 prostatic carcinoma cells)

and *in vivo* in a murine model observing the formation of ferritin and proving the activation of iron metabolism routes to deal with iron coming from the nanoparticles degradation.[225] Calcein staining and Magic Red caspase detection kits were used in a human lung carcinoma cell line (A549) and cytotoxicity has just been observed in the case of hyperthermia application using nanocubes forming multi-core structures.[226] 10 nm nanocubes have been tested for *in vitro* toxicity using a L929 mouse cell line and the Alamar Blue assay and no toxicity was found with concentrations below 100 μg Fe/mL. [227] Toxicity studies of these nanocubes in rats have also shown high biocompatibility as the nanoparticles are efficiently removed from the body by renal excretion.[227]

In general **elongated iron oxide particles** with high aspect ratio would be thought to be more toxic than those with lower ones. Few examples can be found in the literature suggesting higher cytotoxicity effects of elongated nanoparticles in comparison with spherical ones associated with cellular damage, in a similar way as the performed by uric acid crystal deposition.[228]. In particular, **nanorods** have shown a higher degree of membrane damage than spherical ones in mouse macrophage cells.[165] However, these results have to be cautiously analysed as in spite of the different shape, particles also presented very different size and surface area. In addition, in this study, cell viability decreased both for nanorods and nanospheres. It is also worth mentioning that very high doses of other elongated formulations based on iron oxyhydroxides (akaganeite) nanoparticles as part of their composition are well tolerated in animal models.[229] On the contrary, there are examples of iron oxide nanorods with high aspect ratio (an average length of 10 μm) whose cytotoxicity has been studied showing that, even though the nanorods are internalized and located in the perinuclear region, cell viability remained at 100% level within the experimental conditions (NIH/3T3 fibroblast cells using the MTT assay with iron concentrations between 10 μM and 10 mM after 24 h incubation time).[230] PEGylated maghemite (γ-Fe_2O_3) nanotubes have also revealed excellent biocompatibility properties assessed by MTT and flow cytometry.[231]

Cytotoxicity of citrate-coated multicore **maghemite nanoflowers** has been checked in MCF-7 cells incubated during 30 min with concentrations between 0.2 and 5 mM by the Alamar Blue assay showing no significant differences with the control cells.[133] A more complete cytotoxicity assay has been performed using U87n human glioma cell lines, assessing the internalization of the nanoflowers (29 nm particle size) by confocal microscopy, TEM, fluorescence and bioluminesce imaging and flow cytometry. This study also corroborated the low toxicity of the nanoflowers.[232] **Multicore nanoflowers** of around 140 nm have been assessed in two cell lines (Hep G2 and Caco-2) by the MTT assay and have proved that cell viability is only reduced at the

highest dose tested (640 μg/mL).[233] This material has also been administered to a Xenopus Laevis animal model, where a strong dependence on the particle coating and the accumulation in the animal has been found. Although the particles were not lethal in the doses evaluated, several malformations were observed in the embryos. This work highlights the necessity of using simple animal models to assess nanoparticles toxicity that may not be found using just cell cultures.

Cytotoxicity had been assessed **for hollow nanospheres** of 13 nm and OVCAR8 and OVCAR8-ADR cells through MTT studies and no considerable toxicity was found for 72 h, with Fe concentrations up to 16 mM.[234] In addition, hollow nanospheres have been administered to a mouse model showing no apparent signs of toxicity one month after the injection.[158] In the case of tripod particles, cytotoxicity has been compared with spherical particles and it has been found to be low by the MTT assay in Hepa 1-6 and HeLa cells at different time points up to 24 h and using concentrations between 22 and 350 μg Fe/ mL.[235]

In general, it can be concluded that other parameters such as the concentration, the nature of the nanoparticles coating or the incubation time have stronger effects on the nanoparticles toxicity than their shape.[236] Therefore, the effect of the shape on the nanoparticles toxicity is relatively limited and maybe just slightly relevant in the case of high aspect ratio conditions. Beside, contradictory results are found in the literature regarding the influence of the shape and aspect ratio of nanomaterials on their cellular uptake.[237] Inconsistencies may be due to the general lack of standardization in the methodology assessing the toxicity, leading to comparison of data coming from different experimental setups.

5. Applications

5.1. Hyperthermia

Magnetic hyperthermia using Fe_3O_4/γ-Fe_2O_3 nanoparticles has the advantage of selectively killing tumoral cells over healthy ones just by increasing the temperature up to 42-43 ºC in the target area where the particles are located.[238]Briefly, the particles are able to release heat under the action of an alternating magnetic field. Usual frequencies range from 100 to 700 kHz and field amplitudes up to 500 Oe but there is a safe limit that the product of the frequency by the field should fulfil ($5.1 \cdot 10^9$ $A \cdot m^{-1} \cdot s^{-1}$), otherwise inductive heating through eddy currents are generated and heating becomes non-specific. [239,240] The heating efficiency of a suspension of magnetic nanoparticles is evaluated through the specific absorption rate (SAR) (Fig. 19). There are several heating mechanisms implied in the heat release.[241] Depending on the structural and colloidal properties of the particles (i.e. particle size, shape, aggregation state, interactions), the media and

the AC applied field (frequency and amplitude), the dominant mechanism changes while the others become negligible.

An extensive research has been done in the use of **Fe_3O_4 nanocubes** on magnetic hyperthermia. For example, the heating properties of samples with sizes ranging from 13 to 38 nm were tested under different conditions of field and frequency.[224] The best performance was achieved for 19 nm cubes reaching a SAR of 2277 $W \cdot g^{-1}$ (700 kHz, 300 Oe). Smaller and larger cubes did not register a significant heating ($< 300\ W \cdot g^{-1}$) due to the lack of contribution of hysteresis losses for 13 nm nanocubes, while for the 38 nm cubes the reason was the large anisotropy field and formation of isotropic 3D aggregates. However, when these 38 nm cubes were isolated by gallol-polyethylene glycol (GA-PEG), they exhibited a SAR of 1400 $W \cdot g^{-1}$ (320 kHz and field of 300 Oe).[242] Bacterial magnetosomes of 30 nm in length were also evaluated as nano heaters registering values up to 960 $W \cdot g^{-1}$ at 410 kHz and 125 Oe.[240] Much larger nanocubes, 60 nm in size coated by chitosan, leads to a SAR value of 2614 $W \cdot g^{-1}$ under an AC field of 1 MHz and 8.2 Oe due to the contribution of the hysteresis losses mechanism. [226] It should be mentioned in this case that sizes are of the order or slightly above the domain size so magnetization reversal mechanism should be domain wall motion.

For ferromagnetic nanoparticles where hysteresis losses are the dominant mechanism, aggregation is in general an undesired effect diminishing the heating efficiency.[243] Direct studies performed on cubic nanoparticles reveal that SAR values decreases when particles are arranged forming 3D clusters which look like magnetic beads.[63] However, it has been demonstrated theoretical and experimentally that if the particles are forming chain-like structures and aligned in the direction of the field, SAR values increase at least five times in high viscosity medium.[244] The comparison of structures with different morphologies but same volume reinforces the latter assumption. It was found that 24 nm spheres dissipate less heat than 19.5 nm cubes and this was attributed to the formation of chain-like aggregate structures in the case of the cubes. However, comparing heating properties of 53 nm spheres and 43 nm cubes it was found better heating properties for the spherical ones because the cubes were forming strong and isometric aggregates.[245]

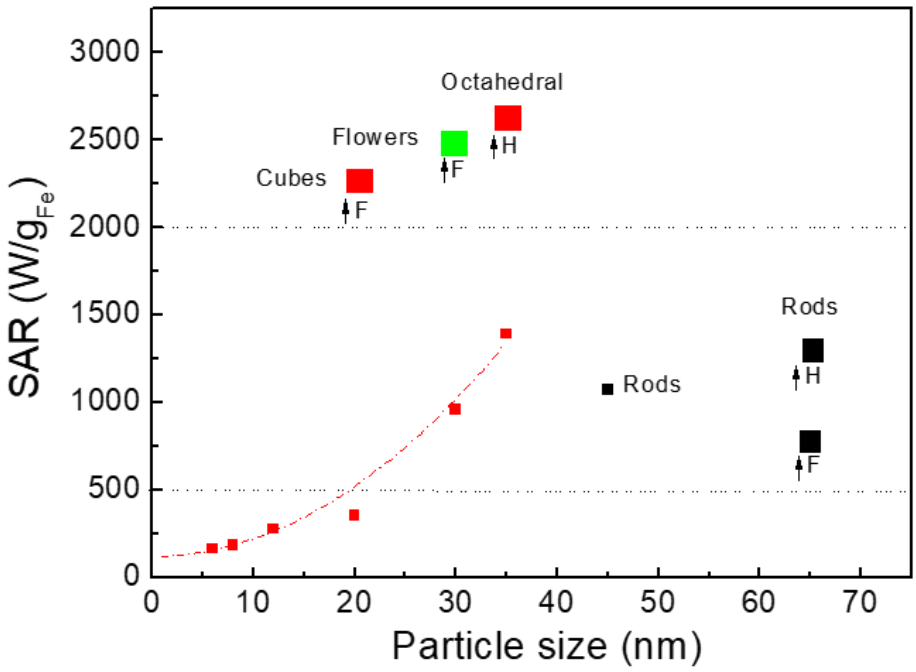

Fig. 19. Specific adsorption rate values (SAR) obtained under moderate values of field and frequency (<300 Oe and <300 kHz) for magnetite nanoparticles of different shape (Cubes in red, elongated in black and flowers in green). Red line show the effect of the size on the SAR values for cube-like shape nanoparticles. The effect of the field conditions are also shown for cubes, rods and flowers (high frequency (F) and high field (H)). (Data and references shown in Table 6).

In the last years, magnetic hyperthermia has been combined with photothermal therapy bringing positive effects as it is known that Fe_3O_4 presents some absorption in the NIR range (Fig. 20a).[246] By using a NIR laser of 808 nm with a power density of 2.5 $W \cdot cm^{-2}$ combined with an alternant magnetic field (900 kHz, 250 Oe) to a suspension of non-aggregated 20 nm nanocubes, SAR values around 4850 $W \cdot g^{-1}$ are obtained. It is worth to note that the SAR value measured using only magnetic hyperthermia is around 1000 $W \cdot g^{-1}$ and, in principle, there is no coupling between the magnetic and electric field as the iron oxide is not a good magnetoplasmonic material. [64]

Octahedral Fe_3O_4 particles (12 nm) presented also enhanced SAR values comparing to the spherical ones as a result of their better magnetic properties (higher M_S and susceptibility). Thus, 6-12 nm octahedrons exhibit values from 163 to 275 $W \cdot g^{-1}$ (247 kHz, 310 Oe) due to the susceptibility losses mechanism (Néel and Brown relaxation).[247] SAR values from around 40 nm octahedrons measured at 358 kHz at different fields goes from 157 $W \cdot g^{-1}$ at 200 Oe to 2483 $W \cdot g^{-1}$ at 800 Oe (Fig. 19).[248] When the particle size of the octahedrons increases to 98 nm, the measured SAR reached 2629 $W \cdot g^{-1}$.

Elongated Fe_3O_4 nanoparticles have received a great attention due to their larger effective anisotropy given by their high aspect ratio. Values up to 1072 $W \cdot g^{-1}$ have been measured for rods of 45x10 nm (390 kHz, 415 Oe) synthesized by reduction of akaganeite (β-FeOOH) nanoparticles. Besides, larger rods (400x40 nm) displayed lower SAR values due to its higher switching field to reverse the magnetic moment.[80] In the case of iron oxide nanorods made by solvothermal approach (65x6 nm), their SAR value reaches 1300 $W \cdot g^{-1}$ (310 kHz, 800 Oe) showing that, if the field amplitude is large enough to reverse the magnetic moment, SAR values increases with the aspect ratio. In contrast, low aspect ratio elongated particles (41x7 nm) only reached SAR values of 540 $W \cdot g^{-1}$.[124] Interestingly, it has been reported that the elongated morphology of Fe_3O_4 rods (200x50 nm) could induce cancer cell death on HeLa cells under mechanical oscillations under exposure to a 35 kHz oscillating magnetic field.[61] This low frequency is associated to the Brownian motion of the nanorods, i.e. physical rotation or vibration leading to mechanical disruption of the cell membrane.[60]

Fe_3O_4 hexagonal nanoplates with a side length of 150-200 nm and a thickness of 10-15 nm synthesized by hydrothermal method in one step display a SAR value of 245 $W \cdot g^{-1}$ (180 kHz, 12 Oe).[249] However, for nanodisks of similar sizes (225 nm in diameter and 26 nm in thickness) when the frequency and applied field increases, a boost of the SAR value up to 4400 $W \cdot g^{-1}$ (488 kHz, 580 Oe) can be observed. [125]This high performance is due to the parallel alignment of the nanodisks with the magnetic field. The dominant heating mechanism was hysteresis loss induced by a vortex domain structure originated by the circular arrangement of the spins. [197,250] This vortex domain structure has the advantage of providing a negligible remanent magnetization so agglomeration due to dipolar interactions is avoided. In conclusion, parallel orientation and vortex domain structure are the responsible for the high SAR values observed for this morphology. However, nanodisks of 12x3 nm lack of this vortex domain configuration and exhibit low SAR values (125 $W \cdot g^{-1}$) in spite of using high frequency and field (310 kHz, 800 Oe).

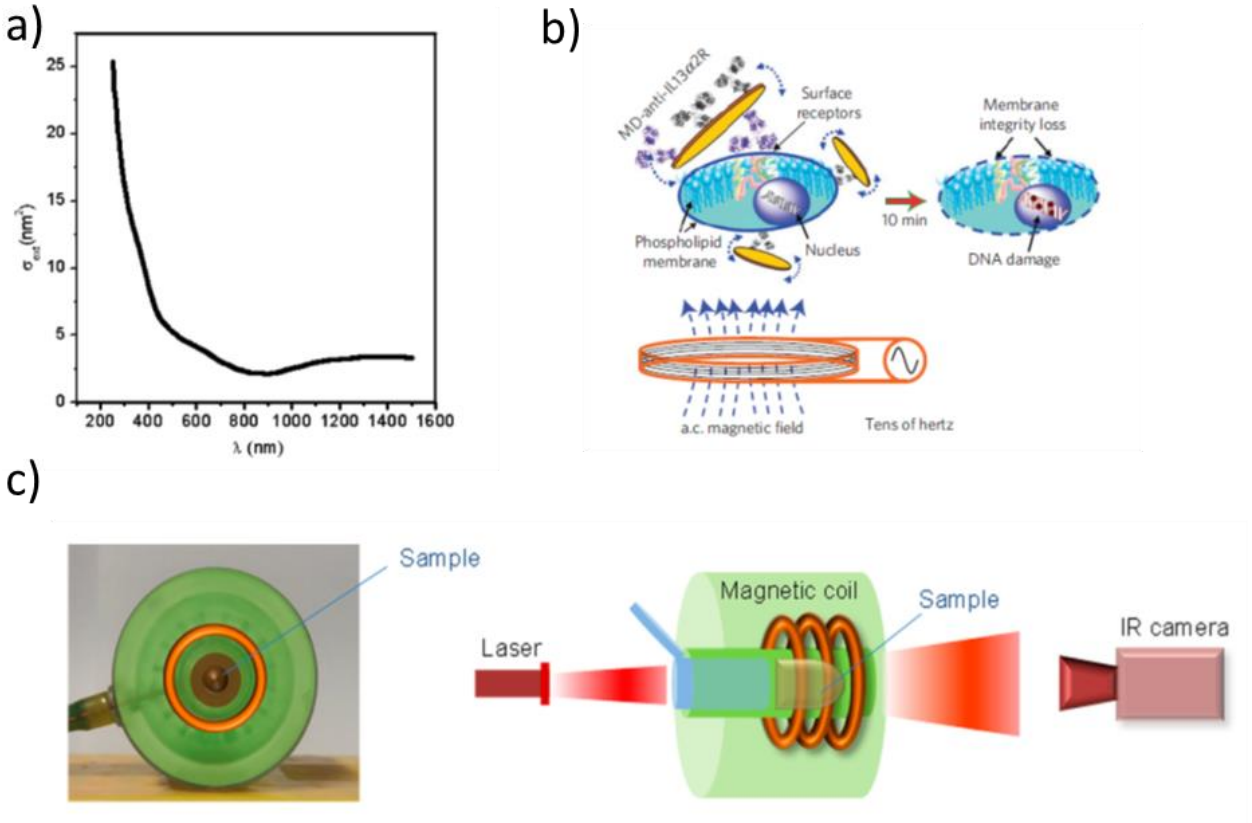

Fig. 20. a) UV-VIS-NIR spectrum of Fe_3O_4. Reprinted with permission from [246]. Copyright (2003) American Chemical Society; b) Scheme of the magnetochemical cancer-cell destruction system using disk-shaped magnetic particles possessing a spin-vortex ground state. Reprinted with permission from [251]. ©2010, by Springer Nature; c) Scheme of the experimental device for combined hyperthermia experiments, consisting of a magnetic coil in which the sample is placed so that it can be illuminated by the near-infrared (NIR) laser (808 nm). Reprinted with permission from [64]. Copyright (2016) American Chemical Society.

Like elongated nanoparticles, **nanodisks morphology** could induce cell death through magneto-mechanical effects (Fig. 20b).[251] Nanodisks of Permalloy coated with gold (1 μm in diameter and 60 nm thickness) where able to exert mechanical forces to the cell under a low alternating field of maximum 60 Hz and 90 Oe and induce the cell death by apoptosis in N10 glioma cells. Cell death mechanism, either apoptotic or necrotic, can be regulated by the magnitude of the magnetic field. Alternating magnetic fields of low frequency induce a shift of the disk vortex structure, creating an oscillation and transmit a mechanical force to the cell. This strategy opens a new pathway where magnetic iron oxide nanodisks could be applied.

Superparamagnetic **flower-like particles** of 50 nm consisting in spherical aggregates of 11 nm grown by the polyol method exhibit a large SAR value of 1790 $W \cdot g^{-1}$, much larger than the SAR measured for single 11 nm particles (48 $W \cdot g^{-1}$). For this special morphology, as the aggregate

size increases the SAR becomes larger but a compromise should be reached between colloidal stability and heating performance. It is clear that the improvement of the SAR values comes from the cooperative interaction of these superparamagnetic cores within the particle.[22]

Table 6.

Hyperthermia performance of Fe_3O_4 nanoparticles with different morphology under AC magnetic fields with different frequency and amplitude.

Morphology	Author/Year/reference	Size (nm)	Frequency (kHz)	Field (Oe)	SAR ($W \cdot g^{-1}$)
Cubes	Guardia 2014[242]	35	320	300	1391
	Hergt 2005 [240]	30	410	125	960
	Tong 2017 [252]	40	325	250	2560
	Guardia 2012 [224]	20	700	300	2277
	Bae 2012 [226]	60	1000	8	2614
	Espinosa 2016 [64]	20	900	250	4850**
Octahedrons	Mohapatra 2015[247]	6	247	310	163
		8	247	310	184
		12	247	310	275
	Lv 2015[248]	13	358	800	1220
		22	358	800	2483
		43	358	800	2629
		98	358	800	750
Rods	Geng 2016[80]	45x10	390	415	1072
	Das 2016[124]	65x5.7	310	800	1300
		41x7	310	800	540
Nanoplates	Ma 2013[249]	150-200 x10-20	180	12	253
	Yang 2014[125]	225x26	488	580	4400
	Nemati 2017[253]	12x3	310	800	125
Flower-like	Hugounenq 2012 [22]	50 (11 nm single core)	700	270	1790

** SAR calculated under the action of a 808 nm laser

In general, the morphologies that exhibit better heating performance under an alternating magnetic field are the nanocubes and octahedrons. SAR values have been enhanced going from around 100-200 $W \cdot g^{-1}$ up to over 3000 $W \cdot g^{-1}$ improving materials and magnetic conditions. Interestingly, two recent strategies have been shown to amplify the heating efficiency of magnetite

suspensions, the formation of chain-like structures and the combination of magnetic hyperthermia with photothermal therapy. In the latter case, it is important to retain the Fe_3O_4 phase on the nanocubes as its absorbance in the NIR range decreases when oxidizes. Interestingly, in terms of SAR values, elongated nanoparticles have not shown high SAR values as expected due to the magnetic shape anisotropy contribution. Nevertheless, for this morphology it is interesting the possibility of promoting cell death under magneto-mechanical forces exerted to the cell membrane by application of alternating magnetic fields of low frequency (20-70 kHz), enough to promote physical rotation of the particles. The same mechanisms could be expanded to nanodisks, but in this case using smaller frequencies of tenths of Hz due to their larger volume.

5.2. Magnetic Resonance Imaging

It is well known that magnetic nanoparticles, either magnetite or maghemite, can act as contrast agents leading to a negative contrast as a consequence of the shortening of the relaxation time (T2) of the nearby water protons induced by the local field from the magnetic nanoparticles. Indeed, there are different formulations for superparamagnetic iron oxide nanoparticle suspensions such as Feridex, Endorem or Resovist approved by the FDA. Unfortunately, they were removed from market due to the lack of clinical use. [254] However, their comeback is not discarded if the toxicity and side effects from gadolinium complex is confirmed.[255]. To evaluate the performance of a contrast agent, one of the parameters is the measurement of the longitudinal or transversal relaxivity (r_1 or r_2 respectively) as it measures the perturbation of the local field generated by the magnetic nanoparticles on the relaxation time of the water protons

Small nanocubes coated by DMSA with different sizes exposing (100) facets revealed that the transversal relaxivity (r_2) increases with particle size rising from 76 $mM^{-1}\cdot s^{-1}$ for 7 nm nanocubes up to 298 $mM^{-1}\cdot s^{-1}$ for 21 nm ones, revealing that the relaxation takes place in the motional averaging regime (MAR).[256] However, single Fe_3O_4 nanocubes 23 nm in size and prepared by thermal decomposition presents r_2 values up to 398 $mM^{-1}\cdot s^{-1}$, much larger than clustered in beads of 200 nm in size, exhibiting relaxivities around 161 $mM^{-1}\cdot s^{-1}$ so the relaxation lies in the dephase regime (SDR).[63] The reason for such decrease lies on their lower magnetic moment per bead compared to the single cubes. Larger nanocubes around the domain size of Fe_3O_4 (58 nm) surrounded by PEG-phospholipid exhibit a r_2 of 324 $mM^{-1}\cdot s^{-1}$ (Fig. 21).[257]

Elongated magnetite nanoparticles exhibit a great performance in MRI only at high fields (3 T) (Table 7). For example, Fe_3O_4 rods of 25 and 50 nm in length (with 5 nm in diameter) coming from the decomposition of iron(III) acetylacetonate and coated by PEI have r_2 values of 670 and

905 $mM^{-1}\cdot s^{-1}$ respectively.[258] This boost enhancement arises from the high M_s and high surface to volume ratio of the nanostructures leading to an enhancement of the water molecules diffusion around the particles. In the same way, magnetite nanorods of 70x12 nm in size, coming from the reduction of β-FeOOH rods, displays a r_2 constant of 608 $mM^{-1}\cdot s^{-1}$. Smaller rods of 30x4 nm exhibit a relaxivity constant of 312 $mM^{-1}\cdot s^{-1}$.[115]

Hollow iron oxide nanoparticles of 11 nm with a void of 5 nm carved under the etching done by TOPO, shows poor performance as T2 contrast agent because the r_2 goes from 60 $mM^{-1}\cdot s^{-1}$ before etching, to 1.25 $mM^{-1}\cdot s^{-1}$ once the particles have been carved by TOPO. **Fe_3O_4 nanoring structure** is also another type of morphology which is not favoured for the application of contrast agents for MRI.[145] Iron oxide nanorings with a magnetization out-of-plane register r_2 values of 74 and 55 $mM^{-1}\cdot s^{-1}$ for 200 and 100 nm nanorings respectively.[259]

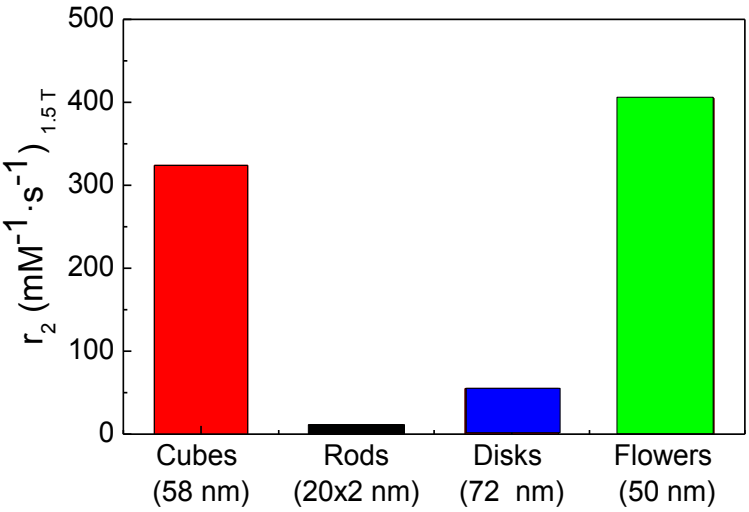

Fig. 21. r_2 relaxivity values at 1.4 or 1.5 T fields for magnetic nanoparticles of different shapes.

The growth of **flower-like γ-Fe_2O_3 nanoparticles** by the polyol method has brought an improvement on the relaxometric properties of the particles for MRI when evaluated for T2 contrast agents (Fig. 21). Thus, 10 nm particles clustered in small aggregates of around 30 nm and coated by citric acid, exhibit a r_2 constant of 365 $mM^{-1}\cdot s^{-1}$, 1.8 times higher than single core nanoparticles made by the same method.[133]This improvement is due to the cooperative behaviour of the magnetic moment which increases the intensity of the local magnetic. It has been observed from theoretical studies that the spin-spin relaxation occurs in the motional average regime (MAR) for clusters up to 120 nm and the r_2 increases with the particle size. However, if the particles are highly aggregated or are too big, the magnetic particles generate a strong magnetic field, the nearby

protons are completely dephased (static dephase regime, SDR)[260] and do not contribute to the MR signal For larger clusters with similar core size it has been observed greater r_2 values up to 405 $mM^{-1}\cdot s^{-1}$ for 50 nm clusters and 508 $mM^{-1}\cdot s^{-1}$ in the case of clusters of around 86 nm.[219] Larger particles (15 nm) with a cluster size of 39 nm show r_2 values up to 418 $mM^{-1}\cdot s^{-1}$.[200].

During the last years, the number of studies based on the possibilities of iron oxide as T1 contrast agents has increased.[261] Magnetic iron oxide T1- contrast agents, lead to bright contrast, as it was proposed for gadolinium complexes[262] or MnO nanoparticles,[263] but is proposed as a safer alternative to gadolinium-based T1 contrast agents.[261] For example, ultrathin iron oxide nanowhiskers (20x2 nm) growth by the hydrolysis of iron(III) oleate and oleylamine at 150 ºC and capped by tween-80, show interesting properties as T1 contrast agents due to its high r_1 (6.3 $mM^{-1}\cdot s^{-1}$) and low r_2 (11.15 $mM^{-1}\cdot s^{-1}$). The reason for such behaviour lies on its nearly paramagnetic behaviour due to its ultra-small diameter.[213]

In summary, there are two morphologies showing great performance for T2-contrast agents, i.e. elongated nanostructures and flower-like nanoparticles (Fig. 21). In the first case, the large magnetic shape anisotropy together with the high surface-to-volume ratio seems to be the origin of the NMR enhancement. In the case of the nanoflowers, the superferromagnetism arising from the clustered morphology seems to be responsible for it. Cluster size and morphology, which sets the crystal facets exposed to nearby water molecules, have been shown to be critical parameters for the performance of such magnetic particles as MRI T2 contrast agents. A new alternative based on the exploitation of the near-paramagnetic properties of elongated and low crystalline magnetic iron oxide nanoparticles opens a new scope for magnetic iron oxide nanoparticles and their used as T1-contrast agents.

Table 7. Summary of the different relaxivity rates of iron oxide nanoparticles with different morphologies and under different fields.

Morphology	Author/Year/reference	Size (nm)	Field (T)	r_1 ($mM^{-1}\cdot s^{-1}$)	r_2 ($mM^{-1}\cdot s^{-1}$)	r_2/r_1
Cubic	Zhou/2015[256]	7	0.5	25	76	3
		15	0.5	19	80	4.2
		21	0.5	27	298	11
	Materia/2015[63]	23 single	1.0	24.2	398	16.4
		23 (200nm beads)	0.5	2.25	161	72
	Lee/2011 [257]	58	1.5	----	324	----
Elongated	Mohapatra/2015[115]	30x4	3	----	312	----
		70x12	3	----	608	----
	Orza/2017[258]	25x5	3	----	670	----
		50x5	3	----	905	----
	Macher/2014[213]	20x2	1.4	6.3	11.15	1.8
Flowers	Lartigue/2012[133]	10(30 nm cluster)	0.2	----	365	----
	Kostopoulo/2014[219]	8-10 (50 nm cluster)	1.4	----	405	----
		8-10 (86 nm cluster)	1.4	----	508	----
	Thomas/2016[200]	15 (39 nm cluster)	3	----	418	----
Hollows	An/2008[145]	11 (void of 5 nm)	1.5	0.16	1.25	7.8
Disk/rings	Liu/2015[197]	72	1.5	0.59	55.1	93
		162	1.5	0.44	73.8	167

5.3. Drug delivery

Magnetic nanoparticles can deliver active compounds to targeted organ/tissue or cells, active or passively. The active targeting depends on the attachment of ligands to the nanoparticles surface, which bind specifically to certain receptors on the targeted cells. [264,265] On the other hand, passive targeting depends on the enhanced permeability and retention effect (EPR effect), explaining their diffusion and accumulation in sites with compromised vascular system.[266] The use of anisometric nanoparticles for drug delivery relies on their high surface-to-volume ratio in combination with enhanced magnetic response and also the possibility of cargo in the case of the hollowed structures. Thus, drug delivery can be combined with magnetic heating to control the drug release and with MRI to follow the treatment and biodistribution/degradation of the particles.

Iron oxide nanocubes (19-22 nm) have been used as drug carriers [267] with a thermoresponsive polymer shell (Poly(N-isopropylacrylamide)), via RAFT (reversible addition-fragmentation chain transfer) polymerization, loading an anticancer drug, Doxorubicin (Dox),

which could be released due to the heat generated by the nanocubes under an alternating magnetic field. The drug loading was around 45 % with respect to the initial Dox amount. For the release it was found that only 8% of the drug loaded was released over 24 hours at 37 ºC, and more than 90 % was released in less than 5 hours when the temperature was raised until 50 ºC, clearly demonstrating that the release was heat triggered. In the same study, triggered drug release was remotely controlled by an alternating magnetic field, AMF (220 kHz and 250 Oe) with an iron concentration of 3.8 $g \cdot L^{-1}$, where about 25% of the drug was released over 4 hours. During the AMF exposure the temperature of the solution reached 80 ºC in the first 15 minutes.

Moreover, 18 nm iron oxide nanocubes were loaded in the shell of polyelectrolyte microcapsules of 4.6 μm diameter with Cascade Blue-labelled dextran and the release was performed by applying an AMF (300 kHz, 300 Oe) [268]. Upon 90 minutes of exposure time the final temperature was about 90 ºC using a concentration of 4.8 $g \cdot L^{-1}$. Some capsules were damaged due to the heat and got partially broken resulting in the release of free magnetic nanoparticles from the capsule wall, as well as the release of Cascade Blue-labelled dextran. For a controlled release of the cargo, an iron concentration of 2.7 $g \cdot L^{-1}$ allowed a suitable temperature increase for opening the walls of the capsules, with a final temperature above 80 ºC. However, the AMF treatment did not release all the cargo molecules, which could be due to the structure of the polyelectrolyte capsules. Some cargo molecules can stay attached to the charged polyelectrolytes of the matrix, even after disruption of the wall.

Iron oxide nanoflowers with a diameter of 1 μm coated by a carbon shell, [269] were tested for loading acetaminophen, an antipyretic and analgesic drug. The porous and heavily functionalized carbon shell with carboxyl and hydroxyl groups provides a pathway for molecules to diffuse or bind together by hydrogen bonding. The drug loading is affected by the mesoporous structure, surface property and morphology, being increased with the increase of the specific surface area and pore volume of the material. In the case of these nanoflowers with a pore diameter of 65 nm the acetaminophen loading was around 30% (saturation) in 2 hours, with a loading degree of 26% in 1 hour. For the release rate the process was carried out in PBS at 37ºC, showing an initial burst release of 74% in 2 hours and reaching 80% after 4 h.

Hollow microspheres of rattle-type magnetic carbon (Fe_3O_4@C) were synthesized and investigated as drug carriers [270]. The final size of these microcapsules loaded with Doxorrubicin was estimated to be 235 nm. The release of the drug occurs by diffusion and almost all the drug was released within 12 hours (82 %). The shell thickness (12 nm, 28 nm, and 40 nm) had influence on

this release, the thinner carbon shell releases faster 82% (12 nm), 74% (28 nm) and 69% (40 nm) respectively to the shell thickness.

Porous hollow nanoparticles of Fe_3O_4, with an average size of 16 nm, prepared by controlled oxidation of amorphous core/shell Fe nanoparticles in the presence of the oxygen-transfer reagent trimethylamine N-oxide (Me_3NO) was used as a cisplatin delivery vehicle. [271] The release by diffusion through the pores could be easily controlled by adjusting the pore sizes and medium pH, since the acidic medium results in wider pore opening and faster release of cisplatin. The shell has a thickness of about 3 nm and a hollow interior about 10 nm in diameter, with pores of around 2-4 nm. The pH-sensitive pore opening can accelerate the cisplatin release in the acidic endosomes/lysosomes once the nanoparticles are internalized. For example, at pH 7.4 the nanoparticles show a gradual release with $t_{1/2}$ = 16 h (the time needed for the release of 50% of the dose) while at pH 5 the cisplatin release is accelerated with $t_{1/2}$ = 4 h. Likewise, **hollow iron oxide nanoparticles** were used to encapsulate Dox which has also a pH-dependent drug release behaviour. [234] The nanoparticles synthesis renders particles with an average hydrodynamic diameter of about 120 nm (with the doxorubicin encapsulated) and with a charge of +16 mV. [271] Dox release rate was measured at room temperature with two different pH values (pH 7.4 and 5). After 24 h incubation at pH 7.4 only 30% of the doxorubicin was released, while the release rate at pH 5 was much faster, where over 80% of doxorubicin was released.

Magnetic hollow spheres of Fe_3O_4 nanosheets (2-4 μm) were prepared by precursor-templated conversion method, with surface modified with poly (ethylene glycol) (PEG). [272] Ibuprofen was used for drug loading where the release behavior was investigated in a simulated body fluid (SBF) over a time period of 136 h. The drug was progressively released by desorption and diffusion. At pH 7.4 about 37% of the loaded drug was released for the first 24 h and 67% for 72 h, and then the drug release rate decreased and reached a value 74% for 136 h.

5.5. Others

5.5.1. Magnetic recording media

In the second half of the 20th century, magnetic recording media were based in acicular iron oxide magnetic nanoparticles (γ-Fe_2O_3) with a length size between 100 and 500 nm and aspect ratios from 6 to 10. They were used as magnetic recording material because of its chemical stability, high magnetic moment aligned with the largest dimension of the particle, high Curie temperature (590-675 ºC) to keep moderate coercivity (not too high to allow successful writing, not too small to resist changes or degradation of signals).[58,273] Elongated morphology was preferred as shape

anisotropy is the main contributor to the effective anisotropy, being up to two orders of magnitude higher than the magnetocrystalline one for particles with axial ratio larger than 6. On the other side, the microstructure of the particles, including defects, pores and inhomogeneities were shown to decrease the effective anisotropy.[274,275] These features are inherent to the synthetic routes employed for the growth the magnetic iron oxides using lepidocrocite (γ-FeOOH) or goethite (α-FeOOH) as shape templates and further its dehydratation that is the main cause of pore and defects formation.[276,277] An alternative route deals with the hydrothermal treatment of $Fe(OH)_3$ which leads to hematite (α-Fe_2O_3) bypassing the formation of iron oxihydroxides and the formation of pores.[278–280] In the last decade of the 20th century, iron oxides, as well as chromium dioxide particles, were replaced by metal particulate materials, which possess twice the magnetization of iron oxides and higher coercivity.[281–284]

5.5.2. Water treatment

One of the major challenges in the environmental field is the water treatment for the removal of heavy metal ions like As, Pb, Hg, Cr, Cd and Ni, which cause harmful effects on humans and animals.[285] Moreover, organic pollutants such detergents, pesticides, all of them from human source, can be also found in water and represent another type of environmental threats. They mainly consist in chlorinated and non-chlorinated aliphatic and aromatic molecules.[286] Traditional methods for water treatment include centrifugation, coagulation, filtration, reverse osmosis. Whereas, the use of iron oxide nanoparticles for water remediation as absorbents of metal ions presents several advantages such as their relatively low cost, the efficient recovery of the material by a simple magnetic separation procedure and also its high specific surface area. [287] It has been demonstrated that the absorption capacity of As(III) and As(V) increases from 0.6 to 59.5 mg $As \cdot g^{-1}$ as the magnetite particle size decreases from 300 to 11 nm because of the exposed surface area but also because the surface become more reactive (decrease of tetrahedral site occupancy).[288–290] The main mechanism related with the absorption of pollutants is the surface is the complexation and/or electrostatic interaction, followed by ion exchange between the iron surface and the toxic ions.[291,292] The performance of the iron oxide nanoparticles depends on the crystalline structure (Fe_3O_4 or γ-Fe_2O_3), particle concentration, surface coating and presence of interfering ions (especially nitrate and phosphate ions).[293,294]

Due to its porous 3D morphology and high specific surface area, micron-sized nanoflowers have shown great potentiality in the absorption of As(V) and Cr(VI). Depending on the phase, it has been found values for the absorption of As(V) of 4.65 and 4.75 $mg \cdot g^{-1}$ and4.38 and 3.86 $mg \cdot g^{-1}$ for the absorption of Cr(VI) in the cases of Fe_3O_4 and γ-Fe_2O_3 respectively.[202] These nanoflowers

have been also tested for the absorption of Orange II reaching absorption values around 43.5 $mg \cdot g^{-1}$. Hollow iron oxide nanocubes with a length of 7 nm and a shell thickness of around 2 nm have shown a powerful capacity for the absorption of As(V) (326 $mg \cdot g^{-1}$) and As(III) (190 $mg \cdot g^{-1}$).[148] Hollow spheres between 200-300 nm in diameter and 20 nm shell thickness were tested for the absorption and removal of Neutral Red dye reaching values up to 90 $mg \cdot g^{-1}$.[295]

Despite these encouraging results, magnetic nanoparticles have important limitations in their use for water remediation, mainly related to the large quantities required for this application and the difficulties to fulfil the regulations for obtaining drinking water .[285]

5.5.3. Spintronics

Magnetite is a high-valuable material for application in spintronics because it is classified as a half-metallic ferromagnet (band gap of 0.1-0.15 eV) with high values of spin polarization but also favourable Curie temperature (T_C= 850 K). [296] It is predicted by Density functional theory (DFT) a value of -100% spin polarization at the Fermi level for the bulk.[297]

Recently, if has been observed that 8 nm Fe_3O_4 nanoparticles with octahedral shape capped with oleylamine exhibit interesting results in tunnelling magnetoresistance (TMR).[298] The oleylamine surface layer between the particles acts as insulating barrier providing multiple tunnel injection junctions where intergranular tunnelling is possible. TMR at room temperature reaches 38 % increasing up to 69 % at 180 K, much higher than those measured for spherical 8 nm particles coated with oleylamine (24 % at room temperature and 41 % at 180 K). The better performance of octahedral particles is consequence of their better stoichiometry at the surface, presenting less defects which increase the spin polarization of the material and so the TMR. Moreover, the fact that {111} facets are exposed facilitates the strong coupling of oleylamine molecules on them. Apart from the metallic character of the material surface, interface effects phenomenology determines the final performance in spintronics.[299]

5.5.4. Microwave absorption

During the latest times, there has been an upsurge of electronic devices and communications (i.e. smartphones, satellite broadcasting, local area network (LAN), radars, etc…) operating in the gigahertz range (GHz) which has the main drawback of the electromagnetic noise leading to poorer communications. Moreover, microwave radiation induces a considerable amount of health threats to organisms causing the breakdown of DNA strands, increasing heart rate, weakening the immune responses and inducing cancer.[300] In this regards, iron oxide magnetic nanoparticles have shown high microwave absorption and low reflection over a broad frequency range. Tuning their microwave absorption properties is possible by controlling the nanoparticle size and shape and

consequently their magnetic properties, that is high saturation magnetization values and low coercivity that favour larger permeability.[301] The development of Fe_3O_4 composites with large anisotropy may exceed the Snoeck limit, having high permittivity and reaching better MW absorption properties.[302]

Fe_3O_4 nanodisks with a thickness of 30 nm have shown an increase of the permittivity with the diameter (from 80 to 500 nm) and resonance frequency. [303] However, the permeability shows an opposite trend (2.0 for the 80 nm and 1.8 for 500 nm disks at 0.1 GHz) due to the increase in shape anisotropy as the diameter grows. The smallest nanodisks (30x 80 nm) exhibit a high microwave absorption as a consequence of its lower permittivity (RL <-10 dB) with wide frequency bandwidth of about 2–18 GHz) with a sheet thickness of around 2.1 mm. Fe_3O_4. In the same way, **nanorods of Fe_3O_4/Fe/SiO_2** of 1 µm x 80 nm present properties as microwave absorbers since the reflection loss below -10 dB is up to 6.96 GHz with a sheet thickness of 2 mm.[214] **Porous magnetite flowers** with a diameter of 2.5 µm composed of cores of 50 nm present a bandwidth with a RL <-10 dB of 3.8 GHz with a minimum of -28.31 dB at 13.26 GHz.

It can be concluded that the performance of Fe_3O_4 for microwave absorption may require high anisotropy material which also contain certain porosity in their structures increasing the interfacial area throughout the composite.[304]

5.5.5. Li-ion batteries

The use of Fe_3O_4 as material for the design of Li-ion batteries (LIBs) is due to its high theoretical capacity (900-1000 $mA \cdot h \cdot g^{-1}$), low cost, environmental friendly and high rate performance.[56,305] The current generation of LIBs is based on electrode materials in which Li is stored by insertion between structural layers during charging and extracted from the layers during discharging without significant structural change, which gives excellent cycling performance. The electrochemical reaction between Li and magnetite occurs as follows

$$Fe_3O_4 + 8Li^+ + 8e^- \longleftrightarrow 3Fe^0 + 4Li_2O$$

Fe_3O_4 presents several drawbacks for their application as LIBs such as stress due to volume changes after lithium ions charge and discharge and the high surface area of nanomaterials which causes aggregation of the iron oxide nanoparticles and electrolyte decomposition forming a thick solid electrolyte interphase on the electrode surface.[306] Fortunately, the use of high porous and/or hollow nanostructures with high surface area have shown good properties as LIBs material because they shorten the diffusion pathway of Li ions and electrons and also increase the electrochemical

reaction area leading to an improvement penetration of the electrolyte and accommodates the strain caused by the lithium inclusion/removal.

For example, high porous **Fe_3O_4 nanorods** with lengths within 400 and 700 nm and diameters between 20 and 80 nm coming from the reduction of goethite nanorods exhibit a high reversible capacity of 843.5 $mA \cdot h \cdot g^{-1}$ after the 50^{th} cycle at 0.1 C (10 h discharge time) due to the high dense porous structure and the elongated morphology.[56]

A composite of **Fe_3O_4 nanoflowers** in carbon with a diameter of 2 μm and sheets of 50 nm in thickness exhibits high capacities up to 1030 $mA \cdot h \cdot g{-}1$ at a density-rate of 0.2 C (5 h discharge time) up to 150 cycles.[307] Noteworthy, it has been observed a different electrochemical activity in the facets exposed to the media by the Fe_3O_4 nanostructures. Thus, {220} facets which can be found in nanoprisms are more electroactive than {111} which are characteristic of octahedrons.[308] Moreover, comparing nanorods, nanoplates and spherical particles, the nanorods present a higher electrochemical activity and larger working capacities.[183]

Hollow γ-Fe_2O_3 nanoparticles with a void around 15 nm and a shell thickness near 4 nm can host lithium ions serving as cathode material reaching a capacity of 219 $mA \cdot h \cdot g^{-1}$ with a Coulombic efficiency of 99.7 %. [309] In the case of smaller **hollow particles** (5.7 nm in void with less than 2 nm in shell thickness) capacities up to 132 $mA \cdot h \cdot g^{-1}$ were displayed, being the high concentration of vacancies and chemical stability of γ-Fe_2O_3 during the voltage window the reasons for these high capacity values.

6. Conclusions and future remarks

The performance of magnetic iron oxide nanoparticles in their different applications requires the design of more complex synthetic routes. One of the strategies that has received a great attention in the last years is the synthesis of magnetic iron oxides with morphologies different from the spherical one. The growth of monodispersed magnetic iron oxide nanoparticles with different geometries leads to enhanced properties, i.e. enhanced magnetic anisotropy, larger specific area, and the origin of new ones like the magnetic structure in vortex domains or magnetomechanical properties. Those properties are very advantageous not only in theranostic applications (MRI and magnetic hyperthermia) but also in others like magnetic recording media, environmental remediation, Li-ion batteries, spintronics and microwave absorption.

This review summarizes the colloidal synthetic routes that lead to magnetic nanoparticles with morphologies different from the spherical one and analyses the key parameters on each route that govern the control of the particle size and shape. Although the final size and shape of the

nanocrystals can be interpreted in terms of classical nucleation and growth theory, it is worth to note that there are several factors that govern the growth and subtle changes could lead to a change in morphology. There is no unique route to obtain a specific morphology, so the final choice should depend on the target size, capping molecules and dispersant. Moreover, factors like time, energy consumption, environmental issues, cost and scalability should be considered when translating this processes into the industry. Thermal decomposition and solvothermal approach can lead to almost all the morphologies presented in the review. Thermal decomposition has the advantages of producing monodisperse nanoparticles with a high crystallinity. However, it needs the use of organic solvents which are not environmentally friendly, and for the application in biomedicine, a further step for water transference and colloidal stabilization is needed. On the other side, solvothermal methods are able to produce nanoparticles stable in water, with protocols less sophisticated than the particles made by thermal decomposition, and using solvents more environmentally friendly. Nevertheless, the synthesis is not scalable, requires a long time and requires in many cases a final step for the reduction of the resulting nanoparticles, from hematite to magnetite.

Structural and magnetic properties of the anisometric nanoparticles depend on the choice of the synthetic route. For example, in the case of elongated nanoparticles, porous structures can be achieved by using shape-templating routes and further reduction to magnetite, in contrast, elongated nanoparticles grown by solvothermal method are generally highly crystalline. Regarding the magnetic properties, it is remarkable the finding of magnetic vortex spin configurations in nanodisks which leads to negligible interparticle interactions and can be very advantageous for biomedical applications.

Most of the research on magnetic nanoparticles for biomedicine until the last decade has been carried out with spherical particles, focusing on particle and aggregate size, the synthetic route chosen and the coating. Since the last decade, the number of literature regarding the synthesis and applications in biomedicine of non-spherical particles has boosted, demonstrating the interest respect to their spherical equivalents. For example, the use of magnetic nanocubes and nanodisks in magnetic hyperthermia leads to an increment in the SAR values, also showing a great performance in *in vitro* studies. Interestingly, the potential of these particles can be increased if magnetic hyperthermia is combined with photothermal therapy or if the nanocubes are integrated into a hybrid heterostructure with gold particles. In the case of the nanodisks, the benefits come not only from the high SAR values, but also for the possibility to induce physical rotation or vibration when subject to an alternating magnetic field of few Hz inducing a mechanical effect on the cell

membranes which induces the apoptotic cell death. The same mechanism could be also applied to elongated nanoparticles.

The synthesis of anisometric magnetic iron oxide nanoparticles also brings benefits for MRI. On one hand, due to the high specific area, elongated nanoparticles are a promising geometry leading to higher r_2 values. Magnetic nanoflowers, due to its spatial clustered configuration which enables the superferromagnetism, have also exhibited a great potentiality. On the other hand, these nanoparticles can manifest a great performance as T1-contrast agents. In this sense, magnetic particles with poor magnetic properties such as nanowhiskers have shown excellent performance due to their low r_2/r_1 values.

Although there are a vast number of synthetic routes leading to anisometric magnetic iron oxide nanoparticles showing a great performance in biomedicine, there is room for improvement to control how these materials are produced. These synthetic processes should evolve to become more robust, reproducible and scalable in order to fulfil the requirements of the FDA before they reach the clinical practice. Moreover, an accurate and standardized systematic cytotoxicity assessment is needed to understand the interaction of cells with nano-objects with special geometries.

Acknowledgements

This work was supported by the European Commission Framework Program 7 (NanoMag project, No. 604448). We acknowledge the Spanish Ministry of Economy and Competitiveness through MAT2014-52069-R, MAT2016-77391 and MAT2017-88148-R,grants, and Consejo Superior de Investigaciones Científicas through PIE-201760E007 project. L.G. acknowledges financial support from the Ramón y Cajal subprogram (RYC-2014-15512). M.E.F.B. acknowledges the Brazilian agency CNPq for her grant within the Science without Borders Program (232947/2014-7). A.G.R. thanks the Generalitat the Catalunya through 2017-SGR-292 project. The ICN2 is funded by the CERCA programme / Generalitat de Catalunya. The ICN2 is supported by the Severo Ochoa programme of the Spanish Ministry of Economy, Industry and Competitiveness (MINECO, grant no. SEV-2013-0295). We acknowledge Miguel Ruiz for the design of most of the figures displayed in this review.

References

[1] D. V. Talapin, J.-S. Lee, M. V. Kovalenko, E. V. Shevchenko, Prospects of Colloidal Nanocrystals for Electronic and Optoelectronic Applications, Chem. Rev. 110 (2010) 389–458.

[2] J. Yang, M.K. Choi, D.-H. Kim, T. Hyeon, Designed Assembly and Integration of Colloidal Nanocrystals for Device Applications, Adv. Mater. 28 (2016) 1176–1207.

[3] D. Kim, J. Kim, Y. Il Park, N. Lee, T. Hyeon, Recent Development of Inorganic Nanoparticles for Biomedical Imaging, ACS Cent. Sci. 4 (2018) 324–336.

[4] D.H. Ortgies, F.J. Teran, U. Rocha, L. de la Cueva, G. Salas, D. Cabrera, A.S. Vanetsev, M. Rähn, V. Sammelselg, Y. V. Orlovskii, D. Jaque, Optomagnetic Nanoplatforms for In Situ Controlled Hyperthermia, Adv. Funct. Mater. 28 (2018) 1704434.

[5] X. Yang, M. Yang, B. Pang, M. Vara, Y. Xia, Gold Nanomaterials at Work in Biomedicine, Chem. Rev. 115 (2015) 10410–10488.

[6] S. Schauermann, N. Nilius, S. Shaikhutdinov, H.-J. Freund, Nanoparticles for Heterogeneous Catalysis: New Mechanistic Insights, Acc. Chem. Res. 46 (2013) 1673–1681.

[7] I. Venditti, Gold Nanoparticles in Photonic Crystals Applications: A Review, Materials (Basel). 10 (2017) 97.

[8] D. Astruc, F. Lu, J.R. Aranzaes, Nanoparticles as Recyclable Catalysts: The Frontier between Homogeneous and Heterogeneous Catalysis, Angew. Chemie Int. Ed. 44 (2005) 7852–7872.

[9] M. Haase, H. Schäfer, Upconverting Nanoparticles, Angew. Chemie Int. Ed. 50 (2011) 5808–5829.

[10] B. Pelaz, C. Alexiou, R.A. Alvarez-Puebla, F. Alves, A.M. Andrews, S. Ashraf, L.P. Balogh, L. Ballerini, A. Bestetti, C. Brendel, S. Bosi, M. Carril, W.C.W. Chan, C. Chen, X. Chen, X. Chen, Z. Cheng, D. Cui, J. Du, C. Dullin, A. Escudero, N. Feliu, M. Gao, M. George, Y. Gogotsi, A. Grünweller, Z. Gu, N.J. Halas, N. Hampp, R.K. Hartmann, M.C. Hersam, P. Hunziker, J. Jian, X. Jiang, P. Jungebluth, P. Kadhiresan, K. Kataoka, A. Khademhosseini, J. Kopeček, N.A. Kotov, H.F. Krug, D.S. Lee, C.M. Lehr, K.W. Leong, X.J. Liang, M. Ling Lim, L.M. Liz-Marzán, X. Ma, P. Macchiarini, H. Meng, H. Möhwald, P. Mulvaney, A.E. Nel, S. Nie, P. Nordlander, T. Okano, J. Oliveira, T.H. Park, R.M. Penner, M. Prato, V. Puntes, V.M. Rotello, A. Samarakoon, R.E. Schaak, Y. Shen, S. Sjöqvist, A.G. Skirtach, M.G. Soliman, M.M. Stevens, H.W. Sung, B.Z. Tang, R. Tietze, B.N. Udugama, J.S. VanEpps, T. Weil, P.S. Weiss, I. Willner, Y. Wu, L. Yang, Z. Yue, Q. Zhang, Q. Zhang, X.E. Zhang, Y. Zhao, X. Zhou, W.J. Parak, Diverse Applications of Nanomedicine, ACS Nano. 11 (2017) 2313–2381.

[11] E. Matijević, Monodispersed colloids: preparations and interactions, in: Interfaces, Surfactants Colloids Eng., Steinkopff, Darmstadt, 1996: pp. 38–44.

[12] T. Sugimoto, Monodispersed Particles, Elsevier Science BV, 2001.

[13] H. Li, H. Xia, W. Ding, Y. Li, Q. Shi, D. Wang, X. Tao, Synthesis of Monodisperse, Quasi-

Spherical Silver Nanoparticles with Sizes Defined by the Nature of Silver Precursors, Langmuir. 30 (2014) 2498–2504.

[14] J. Ulama, M. Zackrisson Oskolkova, J. Bergenholtz, Monodisperse PEGylated Spheres: An Aqueous Colloidal Model System, J. Phys. Chem. B. 118 (2014) 2582–2588.

[15] J. Yang, T. Ling, W.-T. Wu, H. Liu, M.-R. Gao, C. Ling, L. Li, X.-W. Du, A top–down strategy towards monodisperse colloidal lead sulphide quantum dots, Nat. Commun. 4 (2013) 1695.

[16] A. Kuijk, A. van Blaaderen, A. Imhof, Synthesis of Monodisperse, Rodlike Silica Colloids with Tunable Aspect Ratio, J. Am. Chem. Soc. 133 (2011) 2346–2349.

[17] Y.W. Jun, J.S. Choi, J. Cheon, Shape control of semiconductor and metal oxide nanocrystals through nonhydrolytic colloidal routes, Angew. Chemie - Int. Ed. 45 (2006) 3414–3439.

[18] F. Dumestre, B. Chaudret, C. Amiens, M.C. Fromen, M.J. Casanove, P. Renaud, P. Zurcher, Shape control of thermodynamically stable cobalt nanorods through organometallic chemistry, Angew. Chemie - Int. Ed. 41 (2002) 4286–4289.

[19] Z.A. Peng, X. Peng, Nearly Monodisperse and Shape-Controlled CdSe Nanocrystals via Alternative Routes: Nucleation and Growth, J. Am. Chem. Soc. 124 (2002) 3343–3353.

[20] Z. Wang, L.L. Daemen, Y. Zhao, C.S. Zha, R.T. Downs, X. Wang, Z.L. Wang, R.J. Hemley, Morphology-tuned wurtzite-type ZnS nanobelts, Nat. Mater. 4 (2005) 922–927.

[21] N.G. Bastús, E. Gonzalez, J. Esteve, J. Piella, J. Patarroyo, F. Merkoçi, V. Puntes, Exploring New Synthetic Strategies for the Production of Advanced Complex Inorganic Nanocrystals, Zeitschrift Für Phys. Chemie. 229 (2015).

[22] P. Hugounenq, M. Levy, D. Alloyeau, L. Lartigue, E. Dubois, V. Cabuil, C. Ricolleau, S. Roux, C. Wilhelm, F. Gazeau, R. Bazzi, Iron Oxide Monocrystalline Nanoflowers for Highly Efficient Magnetic Hyperthermia, J. Phys. Chem. C. 116 (2012) 15702–15712.

[23] T.K. Sau, A.L. Rogach, Nonspherical Noble Metal Nanoparticles: Colloid-Chemical Synthesis and Morphology Control, Adv. Mater. 22 (2010) 1781–1804.

[24] M. V. Kovalenko, L. Manna, A. Cabot, Z. Hens, D. V. Talapin, C.R. Kagan, V.I. Klimov, A.L. Rogach, P. Reiss, D.J. Milliron, P. Guyot-Sionnnest, G. Konstantatos, W.J. Parak, T. Hyeon, B.A. Korgel, C.B. Murray, W. Heiss, Prospects of Nanoscience with Nanocrystals, ACS Nano. 9 (2015) 1012–1057.

[25] W. Qi, Nanoscopic Thermodynamics, Acc. Chem. Res. 49 (2016) 1587–1595.

[26] T. Sugimoto, Formation of Monodispersed Nano- and Micro-Particles Controlled in Size, Shape, and Internal Structure, Chem. Eng. Technol. 26 (2003) 313–321.

[27] J. Lee, J. Yang, S.G. Kwon, T. Hyeon, Nonclassical nucleation and growth of inorganic

nanoparticles, Nat. Rev. Mater. 1 (2016) 16034.

[28] L. Gutiérrez, F.J. Lázaro, A.R. Abadía, M.S. Romero, C. Quintana, M. Puerto Morales, C. Patiño, R. Arranz, Bioinorganic transformations of liver iron deposits observed by tissue magnetic characterisation in a rat model, J. Inorg. Biochem. 100 (2006) 1790–1799.

[29] L. Qiao, Z. Fu, J. Li, J. Ghosen, M. Zeng, J. Stebbins, P.N. Prasad, M.T. Swihart, Standardizing Size- and Shape-Controlled Synthesis of Monodisperse Magnetite (Fe 3 O 4) Nanocrystals by Identifying and Exploiting Effects of Organic Impurities, ACS Nano. 11 (2017) 6370–6381.

[30] B.H. Kim, J. Yang, D. Lee, B.K. Choi, T. Hyeon, J. Park, Liquid-Phase Transmission Electron Microscopy for Studying Colloidal Inorganic Nanoparticles, Adv. Mater. 30 (2018) 1703316.

[31] S.G. Kwon, Y. Piao, J. Park, S. Angappane, Y. Jo, N.-M. Hwang, J.-G. Park, T. Hyeon, Kinetics of Monodisperse Iron Oxide Nanocrystal Formation by "Heating-Up" Process, J. Am. Chem. Soc. 129 (2007) 12571–12584.

[32] V. Privman, D. V Goia, J. Park, E. Matijević, Mechanism of Formation of Monodispersed Colloids by Aggregation of Nanosize Precursors, J. Colloid Interface Sci. 213 (1999) 36–45.

[33] J. Chen, B. Lim, E.P. Lee, Y. Xia, Shape-controlled synthesis of platinum nanocrystals for catalytic and electrocatalytic applications, Nano Today. 4 (2009) 81–95.

[34] C. Yang, J. Wu, Y. Hou, Fe_3O_4 nanostructures: synthesis, growth mechanism, properties and applications, Chem. Commun. 47 (2011) 5130.

[35] M. Ocaña, R. Rodriguez-Clemente, C.J. Serna, Uniform colloidal particles in solution: Formation mechanisms, Adv. Mater. 7 (1995) 212–216.

[36] M.P. Morales, T. Gonzalez-Carreno, C.J. Serna, The formation of & alpha-Fe_2O_3 monodispersed particles in solution, J. Mater. Res. 7 (1992) 2538–2545.

[37] M.A. Verges, A. Mifsud, C.J. Serna, Formation of rod-like zinc oxide microcrystals in homogeneous solutions, J. Chem. Soc. Faraday Trans. 86 (1990) 959.

[38] C.J. Murphy, T.K. Sau, A.M. Gole, C.J. Orendorff, J. Gao, L. Gou, S.E. Hunyadi, T. Li, Anisotropic Metal Nanoparticles: Synthesis, Assembly, and Optical Applications, J. Phys. Chem. B. 109 (2005) 13857–13870.

[39] E.C. Dreaden, A.M. Alkilany, X. Huang, C.J. Murphy, M.A. El-Sayed, The golden age: gold nanoparticles for biomedicine, Chem. Soc. Rev. 41 (2012) 2740–2779.

[40] Y. Xia, W. Li, C.M. Cobley, J. Chen, X. Xia, Q. Zhang, M. Yang, E.C. Cho, P.K. Brown, Gold Nanocages: From Synthesis to Theranostic Applications, Acc. Chem. Res. 44 (2011) 914–924.

[41] S. Pud, A. Kisner, M. Heggen, D. Belaineh, R. Temirov, U. Simon, A. Offenhäusser, Y. Mourzina, S. Vitusevich, Features of Transport in Ultrathin Gold Nanowire Structures, Small. 9 (2013) 846–852.

[42] Y. Yin, A.P. Alivisatos, Colloidal nanocrystal synthesis and the organic–inorganic interface, Nature. 437 (2005) 664–670.

[43] L.-M. Lacroix, C. Gatel, R. Arenal, C. Garcia, S. Lachaize, T. Blon, B. Warot-Fonrose, E. Snoeck, B. Chaudret, G. Viau, Tuning Complex Shapes in Platinum Nanoparticles: From Cubic Dendrites to Fivefold Stars, Angew. Chemie Int. Ed. 51 (2012) 4690–4694.

[44] K.M. Bratlie, H. Lee, K. Komvopoulos, P. Yang, G.A. Somorjai, Platinum Nanoparticle Shape Effects on Benzene Hydrogenation Selectivity, Nano Lett. 7 (2007) 3097–3101.

[45] S. Ener, E. Anagnostopoulou, I. Dirba, L.-M. Lacroix, F. Ott, T. Blon, J.-Y. Piquemal, K.P. Skokov, O. Gutfleisch, G. Viau, Consolidation of cobalt nanorods: A new route for rare-earth free nanostructured permanent magnets, Acta Mater. 145 (2018) 290–297.

[46] E. Anagnostopoulou, B. Grindi, L.-M. Lacroix, F. Ott, I. Panagiotopoulos, G. Viau, Dense arrays of cobalt nanorods as rare-earth free permanent magnets, Nanoscale. 8 (2016) 4020–4029.

[47] Nguyen TK Thanh, Magnetic Nanoparticles: From Fabrication to Clinical Applications, CRC Press, 2012.

[48] B.D. Cullity, Introduction to Magnetic Materials, John Wiley & Sons, Inc., 2009.

[49] A. Ali, H. Zafar, M. Zia, I. ul Haq, A.R. Phull, J.S. Ali, A. Hussain, Synthesis, characterization, applications, and challenges of iron oxide nanoparticles, Nanotechnol. Sci. Appl. Volume 9 (2016) 49–67.

[50] M. Colombo, S. Carregal-Romero, M.F. Casula, L. Gutiérrez, M.P. Morales, I.B. Böhm, J.T. Heverhagen, D. Prosperi, W.J. Parak, Biological applications of magnetic nanoparticles, Chem. Soc. Rev. 41 (2012) 4306.

[51] M.R. Ghazanfari, M. Kashefi, S.F. Shams, M.R. Jaafari, Perspective of Fe_3O_4 Nanoparticles Role in Biomedical Applications, Biochem. Res. Int. 2016 (2016).

[52] M. Mohapatra, S. Anand, Synthesis and applications of nano-structured iron oxides / hydroxides – a review, Int. J. Eng. Sci. Technol. 2 (2010) 127–146.

[53] A.G. Roca, R. Costo, A.F. Rebolledo, S. Veintemillas-Verdaguer, P. Tartaj, T. González-Carreño, M.P. Morales, C.J. Serna, Progress in the preparation of magnetic nanoparticles for applications in biomedicine, J. Phys. D. Appl. Phys. 42 (2009) 224002.

[54] P. Tartaj, M. a del P. Morales, S. Veintemillas-Verdaguer, T. Gonz lez-Carre o, C.J. Serna, The preparation of magnetic nanoparticles for applications in biomedicine, J. Phys. D. Appl.

Phys. 36 (2003) R182–R197.

[55] D. Lisjak, A. Mertelj, Anisotropic magnetic nanoparticles: A review of their properties, syntheses and potential applications, Prog. Mater. Sci. (2018).

[56] J. Liu, Z. Wu, Q. Tian, W. Wu, X. Xiao, Shape-controlled iron oxide nanocrystals: synthesis, magnetic properties and energy conversion applications, CrystEngComm. 18 (2014) 6303–6326.

[57] G.I. Frolov, Film carriers for super-high-density magnetic storage, Tech. Phys. 46 (2001) 1537–1544.

[58] M.P. Sharrock, Recent advances in metal particulate recording media: Toward the ultimate particle, IEEE Trans. Magn. 36 (2000) 2420–2425.

[59] R. Horimizu, H. Inoue, I. Matsuyama, M. Katsumoto, Oxidation kinetics of acicular iron particles for magnetic recording media, J. Magn. Magn. Mater. 114 (1992) 202–206.

[60] X. Yao, K. Sabyrov, T. Klein, R. Lee Penn, T.S. Wiedmann, Evaluation of magnetic heating of asymmetric magnetite particles, J. Magn. Magn. Mater. 381 (2015) 21–27.

[61] D. Cheng, X. Li, G. Zhang, H. Shi, Morphological effect of oscillating magnetic nanoparticles in killing tumor cells, Nanoscale Res. Lett. 9 (2014) 195.

[62] A.O. Fung, V. Kapadia, E. Pierstorff, D. Ho, Y. Chen, Induction of Cell Death by Magnetic Actuation of Nickel Nanowires Internalized by Fibroblasts, J. Phys. Chem. C. 112 (2008) 15085–15088.

[63] M.E. Materia, P. Guardia, A. Sathya, M. Pernia Leal, R. Marotta, R. Di Corato, T. Pellegrino, Mesoscale assemblies of iron oxide nanocubes as heat mediators and image contrast agents, Langmuir. 31 (2015) 808–816.

[64] A. Espinosa, R. Di Corato, J. Kolosnjaj-Tabi, P. Flaud, T. Pellegrino, C. Wilhelm, Duality of Iron Oxide Nanoparticles in Cancer Therapy: Amplification of Heating Efficiency by Magnetic Hyperthermia and Photothermal Bimodal Treatment, ACS Nano. 10 (2016) 2436–2446.

[65] C.S.B. Dias, T.D.M. Hanchuk, H. Wender, W.T. Shigeyosi, J. Kobarg, A.L. Rossi, M.N. Tanaka, M.B. Cardoso, F. Garcia, Shape Tailored Magnetic Nanorings for Intracellular Hyperthermia Cancer Therapy, Sci. Rep. 7 (2017) 14843.

[66] R.M. Cornell, U. Schwertmann, The Iron Oxides, 2003.

[67] J. Majzlan, K.-D. Grevel, A. Navrotsky, Thermodynamics of Fe oxides: Part II. Enthalpies of formation and relative stability of goethite (α-FeOOH), lepidocrocite (γ-FeOOH), and maghemite (γ-Fe 2 O 3), Am. Mineral. 88 (2003) 855–859.

[68] A. Navrotsky, L. Mazeina, J. Majzlan, Size-Driven Structural and Thermodynamic

Complexity in Iron Oxides, Science. 319 (2008) 1635–1638.

[69] M.P. Morales, C. Pecharroman, T.G. Carreño, C.J. Serna, Structural Characteristics of Uniform γ-Fe2O3 Particles with Different Axial (Length/Width) Ratios, J. Solid State Chem. 108 (1994) 158–163.

[70] P.B. Braun, A Superstructure in Spinels, Nature. 170 (1952) 1123–1123.

[71] K.V.P.M.. Shafi, A.. Ulman, A.. Dyal, X.Z.. Yan, N.L.. Yang, C.. Estournes, L.. Fournes, A.. Wattiaux, H.. White, M. Rafailovich, Magnetic Enhancement of γ-Fe_2O_3 Nanoparticles by Sonochemical Coating, Chem. Mater. 14 (2002) 1778.

[72] R. Massart, E. Dubois, V. Cabuil, E. Hasmonay, Preparation and properties of monodisperse magnetic fluids, J. Magn. Magn. Mater. 149 (1995) 1–5.

[73] R. Massart, Preparation of aqueous magnetic liquids in alkaline and acidic media, IEEE Trans. Magn. 17 (1981) 1247–1248.

[74] J.-H.J.-G.J. Park, K. An, Y. Hwang, J.-H.J.-G.J. Park, H.-J. Noh, J.-Y. Kim, J.-H.J.-G.J. Park, N.-M. Hwang, T. Hyeon, Ultra-large-scale syntheses of monodisperse nanocrystals, Nat. Mater. 3 (2004) 891–895.

[75] F.X. Redl, C.T. Black, G.C. Papaefthymiou, R.L. Sandstrom, M. Yin, H. Zeng, C.B. Murray, S.P. O'Brien, Magnetic, electronic, and structural characterization of nonstoichiometric iron oxides at the nanoscale., J. Am. Chem. Soc. 126 (2004) 14583–14599.

[76] S. Sun, H. Zeng, Size-Controlled Synthesis of Magnetite Nanoparticles, J. Am. Chem. Soc. 124 (2002) 8204–8205.

[77] T. Hyeon, S.S. Lee, J. Park, Y. Chung, H. Bin Na, Synthesis of Highly Crystalline and Monodisperse Maghemite Nanocrystallites without a Size-Selection Process, J. Am. Chem. Soc. 123 (2001) 12798–12801.

[78] A. Pineau, N. Kanari, I. Gaballah, Kinetics of reduction of iron oxides by H2, Thermochim. Acta. 447 (2006) 89–100.

[79] H. Gavilán, O. Posth, L.K. Bogart, U. Steinhoff, L. Gutiérrez, M.P. Morales, How shape and internal structure affect the magnetic properties of anisometric magnetite nanoparticles, Acta Mater. 125 (2017) 416–424.

[80] S. Geng, H. Yang, X. Ren, Y. Liu, S. He, J. Zhou, N. Su, Y. Li, C. Xu, X. Zhang, Z. Cheng, Anisotropic Magnetite Nanorods for Enhanced Magnetic Hyperthermia, Chem. - An Asian J. 11 (2016) 2996–3000.

[81] M.A. Blesa, M. Mijalchik, M. Villegas, G. Rigotti, Transformation of akaganeite into magnetite in aqueous hydrazine suspensions, React. Solids. 2 (1986) 85–94.

[82] M. Kiyama, Conditions for the Formation of Fe_3O_4 by the Air Oxidation of $Fe(OH)_2$

Suspensions., Bull. Chem. Soc. Jpn. 47 (1974) 1646–1650.

[83] R.S. Sapieszko, E. Matijević, Preparation of well-defined colloidal particles by thermal decomposition of metal chelates. I. Iron oxides, J. Colloid Interface Sci. 74 (1980) 405–422.

[84] C.J. Serna, M.P. Morales, Maghemite (γ-Fe2O3): A Versatile Magnetic Colloidal Material, in: Surf. Colloid Sci., Springer US, Boston, MA, 2004: pp. 27–81.

[85] M. Andrés Vergés, R. Costo, A.G. Roca, J.F. Marco, G.F. Goya, C.J. Serna, M.P. Morales, Uniform and water stable magnetite nanoparticles with diameters around the monodomain–multidomain limit, J. Phys. D. Appl. Phys. 41 (2008) 134003.

[86] M. Kosmulski, pH-dependent surface charging and points of zero charge II. Update, J. Colloid Interface Sci. 275 (2004) 214–224.

[87] M. Kosmulski, The pH-dependent surface charging and points of zero charge. V. Update, J. Colloid Interface Sci. 353 (2011) 1–15.

[88] D. Kim, N. Lee, M. Park, B.H. Kim, K. An, T. Hyeon, Synthesis of Uniform Ferrimagnetic Magnetite Nanocubes, J. Am. Chem. Soc. 131 (2009) 454–455.

[89] P. Guardia, N. Pérez, A. Labarta, X. Batlle, Controlled synthesis of iron oxide nanoparticles over a wide size range, Langmuir. 26 (2010) 5843–5847.

[90] H. Yang, T. Ogawa, D. Hasegawa, M. Takahashi, Synthesis and magnetic properties of monodisperse magnetite nanocubes, J. Appl. Phys. 103 (2008) 07D526.

[91] P. Guardia, A. Labarta, X. Batlle, Tuning the Size, the Shape, and the Magnetic Properties of Iron Oxide Nanoparticles, J. Phys. Chem. C. 115 (2011) 390–396.

[92] M. V. Kovalenko, M.I. Bodnarchuk, R.T. Lechner, G. Hesser, F. Schäffler, W. Heiss, Fatty Acid Salts as Stabilizers in Size- and Shape-Controlled Nanocrystal Synthesis: The Case of Inverse Spinel Iron Oxide, J. Am. Chem. Soc. 129 (2007) 6352–6353.

[93] Z.L. Wang, Transmission Electron Microscopy of Shape-Controlled Nanocrystals and Their Assemblies, J. Phys. Chem. B. 104 (2000) 1153–1175.

[94] G. Salazar-Alvarez, J. Qin, V. Šepelák, I. Bergmann, M. Vasilakaki, K.N. Trohidou, J.D. Ardisson, W.A.A. Macedo, M. Mikhaylova, M. Muhammed, M.D. Baró, J. Nogués, Cubic versus Spherical Magnetic Nanoparticles: The Role of Surface Anisotropy, J. Am. Chem. Soc. 130 (2008) 13234–13239.

[95] E. Wetterskog, M. Agthe, A. Mayence, J. Grins, D. Wang, S. Rana, A. Ahniyaz, G. Salazar-Alvarez, L. Bergström, Precise control over shape and size of iron oxide nanocrystals suitable for assembly into ordered particle arrays, Sci. Technol. Adv. Mater. 15 (2014) 055010.

[96] G. Gao, X. Liu, R. Shi, K. Zhou, Y. Shi, R. Ma, E. Takayama-Muromachi, G. Qiu, Shape-

Controlled Synthesis and Magnetic Properties of Monodisperse Fe_3O_4 Nanocubes, Cryst. Growth Des. 10 (2010) 2888–2894.

[97] Z. Xu, C. Shen, Y. Tian, X. Shi, H.-J. Gao, Organic phase synthesis of monodisperse iron oxide nanocrystals using iron chloride as precursor, Nanoscale. 2 (2010) 1027.

[98] W.E.M. Elsayed, F.S. Al-Hazmi, L.S. Memesh, L.M. Bronstein, A novel approach for rapid green synthesis of nearly mono-disperse iron oxide magnetic nanocubes with remarkable surface magnetic anisotropy density for enhancing hyperthermia performance, Colloids Surfaces A Physicochem. Eng. Asp. 529 (2017) 239–245.

[99] L. Zhang, J. Wu, H. Liao, Y. Hou, S. Gao, Octahedral Fe_3O_4 nanoparticles and their assembled structures, Chem. Commun. (2009) 4378.

[100] A. Shavel, B. Rodri, J. Pacifico, M. Spasova, M. Farle, L.M. Liz-marza, B. Rodrı, Shape Control in Iron Oxide Nanocrystal Synthesis , Induced by Trioctylammonium Ions Shape Control in Iron Oxide Nanocrystal Synthesis , Induced by Trioctylammonium Ions, (2009) 5843–5849.

[101] A. Shavel, L.M. Liz-Marzán, Shape control of iron oxide nanoparticles., Phys. Chem. Chem. Phys. 11 (2009) 3762–3763.

[102] J. Cheon, N.-J. Kang, S.-M. Lee, J.-H. Lee, J.-H. Yoon, S.J. Oh, Shape Evolution of Single-Crystalline Iron Oxide Nanocrystals, J. Am. Chem. Soc. 126 (2004) 1950–1951.

[103] A. Mitra, J. Mohapatra, S.S. Meena, C. V. Tomy, M. Aslam, Verwey Transition in Ultrasmall-Sized Octahedral Fe_3O_4 Nanoparticles, J. Phys. Chem. C. 118 (2014) 19356–19362.

[104] B. Park, B.H. Kim, T. Yu, Synthesis of spherical and cubic magnetic iron oxide nanocrystals at low temperature in air, J. Colloid Interface Sci. 518 (2018) 27–33.

[105] D. Faivre, D. Schüler, Magnetotactic bacteria and magnetosomes., Chem. Rev. 108 (2008) 4875–98.

[106] R.E. Dunin-Borkowski;, M.R. McCartney, R.B. Frankel, D.A. Bazylinski, M. Pósfai, P.R. Buseck, Magnetic Microstructure of Magnetotactic Bacteria by Electron Holography, Science1. 282 (1998) 1868–1870.

[107] S. Mann, R.B. Frankel, R.P. Blakemor, Structure, morphology and crystal growth of bacterial magnetite, Nature. 310 (1984) 405–407.

[108] M. Ozaki, S. Kratohvil, E. Matijević, Formation of monodispersed spindle-type hematite particles, J. Colloid Interface Sci. 102 (1984) 146–151.

[109] H. Wiogo, M. Lim, P. Munroe, R. Amal, Understanding the formation of iron oxide nanoparticles with acicular structure from iron(III) chloride and hydrazine monohydrate,

Cryst. Growth Des. 11 (2011) 1689–1696.

[110] S. Palchoudhury, W. An, Y. Xu, Y. Qin, Z. Zhang, N. Chopra, R.A. Holler, C.H. Turner, Y. Bao, Synthesis and growth mechanism of iron oxide nanowhiskers, Nano Lett. 11 (2011) 1141–1146.

[111] A.F. Rebolledo, O. Bomatí-Miguel, J.F. Marco, P. Tartaj, A facile synthetic route for the preparation of superparamagnetic iron oxide nanorods and nanorices with tunable surface functionality, Adv. Mater. 20 (2008) 1760–1765.

[112] B. Tang, G. Wang, L. Zhuo, J. Ge, L. Cui, Facile Route to α-FeOOH and α-Fe_2O_3 Nanorods and Magnetic Property of α-Fe_2O_3 Nanorods, Inorg. Chem. 45 (2006) 5196–5200.

[113] K.E. Gonsalves, H. Li, P. Santiago, No Title, J. Mater. Sci. 36 (2001) 2461–2471.

[114] Y. Piao, J. Kim, H. Bin Na, D. Kim, J.S. Baek, M.K. Ko, J.H. Lee, M. Shokouhimehr, T. Hyeon, Wrap–bake–peel process for nanostructural transformation from β-FeOOH nanorods to biocompatible iron oxide nanocapsules, Nat. Mater. 7 (2008) 242–247.

[115] J. Mohapatra, A. Mitra, H. Tyagi, D. Bahadur, M. Aslam, Iron oxide nanorods as high-performance magnetic resonance imaging contrast agents, Nanoscale. 7 (2015) 9174–9184.

[116] S. Lentijo Mozo, E. Zuddas, A. Casu, A. Falqui, Synthesizing Iron Oxide Nanostructures: The Polyethylenenemine (PEI) Role, Crystals. 7 (2017) 22.

[117] S. Xuan, F. Liang, K. Shu, Novel method to fabricate magnetic hollow silica particles with anisotropic structure, J. Magn. Magn. Mater. 321 (2009) 1029–1033.

[118] O. Bomati-Miguel, A.F. Rebolledo, P. Tartaj, Controlled formation of porous magnetic nanorods via a liquid/liquid solvothermal method., Chem. Commun. (Camb). (2008) 4168–4170.

[119] E. Matijević, P. Scheiner, Ferric hydrous oxide sols, J. Colloid Interface Sci. 63 (1978) 509–524.

[120] S. Zhang, W. Wu, X. Xiao, J. Zhou, F. Ren, C. Jiang, Preparation and characterization of spindle-like Fe_3O_4 mesoporous nanoparticles, Nanoscale Res. Lett. 6 (2011) 89.

[121] S. Sacanna, L. Rossi, B.W.M. Kuipers, A.P. Philipse, Fluorescent Monodisperse Silica Ellipsoids for Optical Rotational Diffusion Studies, Langmuir. 22 (2006) 1822–1827.

[122] M. Ocaña, M.P. Morales, C.J. Serna, Homogeneous Precipitation of Uniform α-Fe_2O_3 Particles from Iron Salts Solutions in the Presence of Urea, J. Colloid Interface Sci. 212 (1999) 317–323.

[123] S.-J. Park, S. Kim, S. Lee, Z.G. Khim, K. Char, T. Hyeon, Synthesis and Magnetic Studies of Uniform Iron Nanorods and Nanospheres, J. Am. Chem. Soc. 122 (2000) 8581–8582.

[124] R. Das, J. Alonso, Z. Nemati Porshokouh, V. Kalappattil, D. Torres, M.-H. Phan, E. Garaio,

J.Á. García, J.L. Sanchez Llamazares, H. Srikanth, Tunable High Aspect Ratio Iron Oxide Nanorods for Enhanced Hyperthermia, J. Phys. Chem. C. 120 (2016) 10086–10093.

[125] Y. Yang, X. Liu, Y. Lv, T.S. Herng, X. Xu, W. Xia, T. Zhang, J. Fang, W. Xiao, J. Ding, Orientation mediated enhancement on magnetic hyperthermia of Fe3 O4 nanodisc, Adv. Funct. Mater. 25 (2015) 812–820.

[126] L. Chen, X. Yang, J. Chen, J. Liu, H. Wu, H. Zhan, C. Liang, M. Wu, Continuous shape- and spectroscopy-tuning of hematite nanocrystals, Inorg. Chem. 49 (2010) 8411–8420.

[127] Y. Huang, D. Ding, M. Zhu, W. Meng, Y. Huang, F. Geng, J. Li, J. Lin, C. Tang, Z. Lei, Z. Zhang, C. Zhi, Facile synthesis of α-Fe 2 O 3 nanodisk with superior photocatalytic performance and mechanism insight, Sci. Technol. Adv. Mater. 16 (2015) 014801.

[128] J. Lu, X. Jiao, D. Chen, W. Li, Solvothermal Synthesis and Characterization of Fe3O4 and γ-Fe_2O_3 Nanoplates, J. Phys. Chem. C. 113 (2009) 4012–4017.

[129] S. Palchoudhury, Y. Xu, A. Rushdi, R.A. Holler, Y. Bao, Controlled synthesis of iron oxide nanoplates and nanoflowers, Chem. Commun. 48 (2012) 10499.

[130] G. Hemery, A.C. Keyes, E. Garaio, I. Rodrigo, J.A. Garcia, F. Plazaola, E. Garanger, O. Sandre, Tuning Sizes, Morphologies, and Magnetic Properties of Monocore Versus Multicore Iron Oxide Nanoparticles through the Controlled Addition of Water in the Polyol Synthesis, Inorg. Chem. 56 (2017) 8232–8243.

[131] H. Gavilán, A. Kowalski, D. Heinke, A. Sugunan, J. Sommertune, M. Varón, L.K. Bogart, O. Posth, L. Zeng, D. González-Alonso, C. Balceris, J. Fock, E. Wetterskog, C. Frandsen, N. Gehrke, C. Grüttner, A. Fornara, F. Ludwig, S. Veintemillas-Verdaguer, C. Johansson, M.P. Morales, Colloidal Flower-Shaped Iron Oxide Nanoparticles: Synthesis Strategies and Coatings, Part. Part. Syst. Charact. 34 (2017) 1700094.

[132] D. Caruntu, G. Caruntu, Y. Chen, C.J. O'Connor, G. Goloverda, V.L. Kolesnichenko, Synthesis of Variable-Sized Nanocrystals of Fe3O4 with High Surface Reactivity, Chem. Mater. 16 (2004) 5527–5534.

[133] L. Lartigue, P. Hugounenq, D. Alloyeau, S.P. Clarke, M. Lévy, J.-C. Bacri, R. Bazzi, D.F. Brougham, C. Wilhelm, F. Gazeau, Cooperative Organization in Iron Oxide Multi-Core Nanoparticles Potentiates Their Efficiency as Heating Mediators and MRI Contrast Agents, ACS Nano. 6 (2012) 10935–10949.

[134] J. Liu, Z. Sun, Y. Deng, Y. Zou, C. Li, X. Guo, L. Xiong, Y. Gao, F. Li, D. Zhao, Highly Water-Dispersible Biocompatible Magnetite Particles with Low Cytotoxicity Stabilized by Citrate Groups, Angew. Chemie Int. Ed. 48 (2009) 5875–5879.

[135] J. Liang, H. Ma, W. Luo, S. Wang, Synthesis of magnetite submicrospheres with tunable size

and superparamagnetism by a facile polyol process, Mater. Chem. Phys. 139 (2013) 383–388.

[136] Q. Sun, Z. Ren, R. Wang, W. Chen, C. Chen, Magnetite hollow spheres: solution synthesis, phase formation and magnetic property, J. Nanoparticle Res. 13 (2011) 213–220.

[137] C. Cheng, F. Xu, H. Gu, Facile synthesis and morphology evolution of magnetic iron oxide nanoparticles in different polyol processes, New J. Chem. 35 (2011) 1072.

[138] Q.Q. Xiong, J.P. Tu, Y. Lu, J. Chen, Y.X. Yu, Y.Q. Qiao, X.L. Wang, C.D. Gu, Synthesis of Hierarchical Hollow-Structured Single-Crystalline Magnetite (Fe 3 O 4) Microspheres: The Highly Powerful Storage versus Lithium as an Anode for Lithium Ion Batteries, J. Phys. Chem. C. 116 (2012) 6495–6502.

[139] W. Luo, H. Ma, F. Mou, M. Zhu, J. Yan, J. Guan, Steric-Repulsion-Based Magnetically Responsive Photonic Crystals, Adv. Mater. 26 (2014) 1058–1064.

[140] H. Wang, Y.-B. Sun, Q.-W. Chen, Y.-F. Yu, K. Cheng, Synthesis of carbon-encapsulated superparamagnetic colloidal nanoparticles with magnetic-responsive photonic crystal property, Dalt. Trans. 39 (2010) 9565.

[141] R. Di Corato, P. Piacenza, M. Musarò, R. Buonsanti, P.D. Cozzoli, M. Zambianchi, G. Barbarella, R. Cingolani, L. Manna, T. Pellegrino, Magnetic-Fluorescent Colloidal Nanobeads: Preparation and Exploitation in Cell Separation Experiments, Macromol. Biosci. 9 (2009) 952–958.

[142] S. Yu, G.M. Chow, Synthesis of monodisperse iron oxide and iron/iron oxide core/shell nanoparticles via iron-oleylamine complex, J. Nanosci. Nanotechnol. 6 (2006) 2135–2140.

[143] W. Li, S.S. Lee, J. Wu, C.H. Hinton, J.D. Fortner, Shape and size controlled synthesis of uniform iron oxide nanocrystals through new non-hydrolytic routes, Nanotechnology. 27 (2016) 324002.

[144] F. Vita, H. Gavilán, F. Rossi, C. de Julián Fernández, A. Secchi, A. Arduini, F. Albertini, M.P. Morales, Tuning morphology and magnetism of magnetite nanoparticles by calix[8]arene-induced oriented aggregation, CrystEngComm. 18 (2016) 8591–8598.

[145] K. An, S.G. Kwon, M. Park, H. Bin Na, S.-I. Baik, J.H. Yu, D. Kim, J.S. Son, Y.W. Kim, I.C. Song, W.K. Moon, H.M. Park, T. Hyeon, Synthesis of Uniform Hollow Oxide Nanoparticles through Nanoscale Acid Etching, Nano Lett. 8 (2008) 4252–4258.

[146] A. Cabot, V.F. Puntes, E. Shevchenko, Y. Yin, L. Balcells, M.A. Marcus, S.M. Hughes, A.P. Alivisatos, Vacancy Coalescence during Oxidation of Iron Nanoparticles, J. Am. Chem. Soc. 129 (2007) 10358–10360.

[147] S. Peng, S. Sun, Synthesis and characterization of monodisperse hollow Fe_3O_4 nanoparticles,

Angew. Chemie - Int. Ed. 46 (2007) 4155–4158.

[148] L. Balcells, C. Martínez-Boubeta, J. Cisneros-Fernández, K. Simeonidis, B. Bozzo, J. Oró-Sole, N. Bagués, J. Arbiol, N. Mestres, B. Martínez, One-Step Route to Iron Oxide Hollow Nanocuboids by Cluster Condensation: Implementation in Water Remediation Technology, ACS Appl. Mater. Interfaces. 8 (2016) 28599–28606.

[149] D. Kim, J. Park, K. An, N.-K. Yang, J.-G. Park, T. Hyeon, Synthesis of hollow iron nanoframes., J. Am. Chem. Soc. 129 (2007) 5812–3.

[150] K. Ota, S. Mitsushima, N. Hattori, N. Kamiya, Corrosion of Fe with Sodium Compounds with Molten Sodium Hydroxide and, Bull. Chem. Soc. Jpn. 75 (2002) 1855–1859.

[151] N. Ohtori, T. Furukawa, F. Ueno, n situ Raman spectroscopic observation of corrosion reaction of Fe with Na_2O_2 up to 833 K, Electrochemistry. 73 (2005) 675–679.

[152] M.H. Oh, T. Yu, S.-H. Yu, B. Lim, K.-T. Ko, M.-G. Willinger, D.-H. Seo, B.H. Kim, M.G. Cho, J.-H. Park, K. Kang, Y.-E. Sung, N. Pinna, T. Hyeon, Galvanic Replacement Reactions in Metal Oxide Nanocrystals, Science. 340 (2013) 964–968.

[153] A. López-Ortega, A.G. Roca, P. Torruella, M. Petrecca, S. Estradé, F. Peiró, V. Puntes, J. Nogués, Galvanic Replacement onto Complex Metal-Oxide Nanoparticles: Impact of Water or Other Oxidizers in the Formation of either Fully Dense Onion-like or Multicomponent Hollow MnO x /FeO x Structures, Chem. Mater. 28 (2016) 8025–8031.

[154] C.-J. Jia, L.-D.S. Sun, F. Luo, X.-D. Han, L.J. Heyderman, Z.-G. Yan, C.-H. Yan, K. Zheng, Z. Zhang, M. Takano, N. Hayashi, M. Eltschka, M. Kläui, U. Rüdiger, T. Kasama, L. Cervera-Gontard, R.E. Dunin-Borkowski, G. Tzvetkov, J. Raabe, Large-scale synthesis of single-crystalline iron oxide magnetic nanorings., J. Am. Chem. Soc. 130 (2008) 16968–77.

[155] A.H. Latham, M.J. Wilson, P. Schiffer, M.E. Williams, TEM-induced structural evolution in amorphous Fe oxide nanoparticles, J. Am. Chem. Soc. 128 (2006) 12632–12633.

[156] D.A.J. Herman, S. Cheong, M.J. Banholzer, R.D. Tilley, How hollow structures form from crystalline iron–iron oxide core–shell nanoparticles in the electron beam, Chem. Commun. 49 (2013) 6203.

[157] C.-J. Jia, L.-D. Sun, Z.-G. Yan, L.-P. You, F. Luo, X.-D. Han, Y.-C. Pang, Z. Zhang, C.-H. Yan, Single-Crystalline Iron Oxide Nanotubes, Angew. Chemie Int. Ed. 44 (2005) 4328–4333.

[158] L.L. Wang, J. Bao, L.L. Wang, F. Zhang, Y. Li, One-pot synthesis and bioapplication of amine-functionalized magnetite nanoparticles and hollow nanospheres, Chem. - A Eur. J. 12 (2006) 6341–6347.

[159] J.H. Park, G. Von Maltzahn, L. Zhang, M.P. Schwartz, E. Ruoslahti, S.N. Bhatia, M.J.

Sailor, Magnetic iron oxide nanoworms for tumor targeting and imaging, Adv. Mater. 20 (2008) 1630–1635.

[160] S. Palchoudhury, Y. Xu, J. Goodwin, Y. Bao, Synthesis of iron oxide nanoworms, J. Appl. Phys. 109 (2011) 21–23.

[161] L.M. Bronstein, J.E. Atkinson, A.G. Malyutin, F. Kidwai, B.D. Stein, D.G. Morgan, J.M. Perry, J.A. Karty, Nanoparticles by Decomposition of Long Chain Iron Carboxylates: From Spheres to Stars and Cubes, Langmuir. 27 (2011) 3044–3050.

[162] P.D. Cozzoli, E. Snoeck, M.A. Garcia, C. Giannini, A. Guagliardi, A. Cervellino, F. Gozzo, A. Hernando, K. Achterhold, N. Ciobanu, F.G. Parak, R. Cingolani, L. Manna, Colloidal synthesis and characterization of tetrapod-shaped magnetic nanocrystals, Nano Lett. 6 (2006) 1966–1972.

[163] X. Li, Z. Si, Y. Lei, J. Tang, S. Wang, S. Su, S. Song, L. Zhao, H. Zhang, Direct hydrothermal synthesis of single-crystalline triangular Fe_3O_4 nanoprisms, CrystEngComm. 12 (2010) 2060.

[164] Y. Zeng, R. Hao, B. Xing, Y. Hou, Z. Xu, One-pot synthesis of Fe3O4 nanoprisms with controlled electrochemical properties, Chem. Commun. 46 (2010) 3920.

[165] J.H. Lee, J.E. Ju, B. Il Kim, P.J. Pak, E.-K. Choi, H.-S. Lee, N. Chung, Rod-shaped iron oxide nanoparticles are more toxic than sphere-shaped nanoparticles to murine macrophage cells, Environ. Toxicol. Chem. 33 (2014) 2759–2766.

[166] N.T.K. Thanh, N. Maclean, S. Mahiddine, Mechanisms of Nucleation and Growth of Nanoparticles in Solution, Chem. Rev. 114 (2014) 7610–7630.

[167] Y. Jun, J.-H. Lee, J. Choi, J. Cheon, Symmetry-Controlled Colloidal Nanocrystals: Nonhydrolytic Chemical Synthesis and Shape Determining Parameters, J. Phys. Chem. B. 109 (2005) 14795–14806.

[168] S.G. Kwon, T. Hyeon, Colloidal Chemical Synthesis and Formation Kinetics of Uniformly Sized Nanocrystals of Metals, Oxides, and Chalcogenides, Acc. Chem. Res. 41 (2008) 1696–1709.

[169] E.R. Leite, C. Ribeiro, Crystallization and Growth of Colloidal Nanocrystals, Springer New York, New York, NY, 2012.

[170] C. Burda, X. Chen, R. Narayanan, M.A. El-Sayed, Chemistry and Properties of Nanocrystals of Different Shapes, Chem. Rev. 105 (2005) 1025–1102.

[171] J. Park, J. Joo, S.G. Kwon, Y. Jang, T. Hyeon, Synthesis of Monodisperse Spherical Nanocrystals, Angew. Chemie Int. Ed. 46 (2007) 4630–4660.

[172] Z. Wu, S. Yang, W. Wu, Shape control of inorganic nanoparticles from solution, Nanoscale.

8 (2016) 1237–1259.

[173] J. van Embden, A.S.R. Chesman, J.J. Jasieniak, The Heat-Up Synthesis of Colloidal Nanocrystals, Chem. Mater. 27 (2015) 2246–2285.

[174] M. Chen, J.P. Liu, S. Sun, One-Step Synthesis of FePt Nanoparticles with Tunable Size, J. Am. Chem. Soc. 126 (2004) 8394–8395.

[175] T. Sugimoto, E. Matijević, Formation of uniform spherical magnetite particles by crystallization from ferrous hydroxide gels, J. Colloid Interface Sci. 74 (1980) 227–243.

[176] V.K. LaMer, R.H. Dinegar, Theory, Production and Mechanism of Formation of Monodispersed Hydrosols, J. Am. Chem. Soc. 72 (1950) 4847–4854.

[177] E. Ringe, R.P. Van Duyne, L.D. Marks, Wulff construction for alloy nanoparticles, Nano Lett. 11 (2011) 3399–3403.

[178] X. Peng, L. Manna, W. Yang, J. Wickham, E. Scher, A. Kadavanich, A.P. Alivisatos, Shape control of CdSe nanocrystals, Nature. 404 (2000) 59–61.

[179] L. Manna, E.C. Scher, A.P. Alivisatos, Synthesis of soluble and processable rod-, arrow-, teardrop-, and tetrapod-shaped CdSe nanocrystals, J. Am. Chem. Soc. 122 (2000) 12700–12706.

[180] Z.A. Peng, X. Peng, Mechanisms of the Shape Evolution of CdSe Nanocrystals, J. Am. Chem. Soc. 123 (2001) 1389–1395.

[181] Z. Xu, C. Shen, Y. Hou, H. Gao, S. Sun, Oleylamine as Both Reducing Agent and Stabilizer in a Facile Synthesis of Magnetite Nanoparticles Oleylamine as Both Reducing Agent and Stabilizer in a Facile Synthesis of Magnetite Nanoparticles, Communications. 21 (2009) 1778–1780.

[182] Y. Hou, Z. Xu, S. Sun, Controlled synthesis and chemical conversions of FeO nanoparticles, Angew. Chemie - Int. Ed. 46 (2007) 6329–6332.

[183] H. Sun, B. Chen, X. Jiao, Z. Jiang, Z. Qin, D. Chen, Solvothermal Synthesis of Tunable Electroactive Magnetite Nanorods by Controlling the Side Reaction, J. Phys. Chem. C. 116 (2012) 5476–5481.

[184] A. Pardo, R. Pujales, M. Blanco, E.M. Villar-Alvarez, S. Barbosa, P. Taboada, V. Mosquera, Analysis of the influence of synthetic paramaters on the structure and physico-chemical properties of non-spherical iron oxide nanocrystals and their biological stability and compatibility, Dalt. Trans. 45 (2016) 797–810.

[185] H. Yang, D. Hasegawa, M. Takahashi, T. Ogawa, Facile synthesis, phase transfer, and magnetic properties of monodisperse magnetite nanocubes, IEEE Trans. Magn. 44 (2008) 3895–3898.

[186] M. Estrader, A. Lopez-Ortega, I. V Golosovsky, S. Estrade, A.G. Roca, G. Salazar-Alvarez, L. Lopez-Conesa, D. Tobia, E. Winkler, J.D. Ardisson, W.A.A. Macedo, A. Morphis, M. Vasilakaki, K.N. Trohidou, A. Gukasov, I. Mirebeau, O.L. Makarova, R.D. Zysler, F. Peiro, M.D. Baro, L. Bergstrom, J. Nogues, Origin of the large dispersion of magnetic properties in nanostructured oxides: FexO/Fe3O4 nanoparticles as a case study, Nanoscale. 7 (2015) 3002–3015.

[187] E. Wetterskog, C.-W. Tai, J. Grins, L. Bergström, G. Salazar-Alvarez, Anomalous Magnetic Properties of Nanoparticles Arising from Defect Structures: Topotaxial Oxidation of Fe1-xO|Fe3−δO4Core|Shell Nanocubes to Single-Phase Particles, ACS Nano. 7 (2013) 7132–7144.

[188] A. López-Ortega, E. Lottini, G. Bertoni, C. de Julián Fernández, C. Sangregorio, Topotaxial Phase Transformation in Cobalt Doped Iron Oxide Core/Shell Hard Magnetic Nanoparticles, Chem. Mater. 29 (2017) 1279–1289.

[189] M. Figlarz, Topotaxy, nucleation and growth, Solid State Ionics. 43 (1990) 143–170.

[190] B. Devouard, M. Posfai, X. Hua, D.A. Bazylinski, R.B. Frankel, P.R. Buseck, Magnetite from magnetotactic bacteria; size distributions and twinning, Am. Mineral. 83 (1998) 1387–1398.

[191] G. Mirabello, J.J.M. Lenders, N.A.J.M. Sommerdijk, Bioinspired synthesis of magnetite nanoparticles, Chem. Soc. Rev. 45 (2016) 5085–5106.

[192] Y. Amemiya, A. Arakaki, S.S. Staniland, T. Tanaka, T. Matsunaga, Controlled formation of magnetite crystal by partial oxidation of ferrous hydroxide in the presence of recombinant magnetotactic bacterial protein Mms6, Biomaterials. 28 (2007) 5381–5389.

[193] A. Arakaki, F. Masuda, Y. Amemiya, T. Tanaka, T. Matsunaga, Control of the morphology and size of magnetite particles with peptides mimicking the Mms6 protein from magnetotactic bacteria, J. Colloid Interface Sci. 343 (2010) 65–70.

[194] I. Milosevic, H. Jouni, C. David, F. Warmont, D. Bonnin, L. Motte, Facile microwave process in water for the fabrication of magnetic nanorods, J. Phys. Chem. C. 115 (2011) 18999–19004.

[195] P.R. Swann, N.J. Tighe, High voltage microscopy of the reduction of hematite to magnetite, Metall. Trans. B. 8 (1977) 479–487.

[196] Y. Yang, M. Li, Y. Wu, T. Wang, E. Shi, G. Choo, J. Ding, B. Zong, Z. Yang, J. Xue, Nanoscaled self-alignment of Fe 3 O 4 nanodiscs in ultrathin rGO films with engineered conductivity for electromagnetic interference shielding, Nanoscale. 8 (2016) 15989–15998.

[197] X.-L. Liu, Y. Yang, J.-P. Wu, Y.-F. Zhang, H.-M. Fan, J. Ding, Novel magnetic vortex

nanorings/nanodiscs: Synthesis and theranostic applications, Chinese Phys. B. 24 (2015) 127505.

[198] A. Cabot, A.P. Alivisatos, V.F. Puntes, L. Balcells, Ò. Iglesias, A. Labarta, Magnetic domains and surface effects in hollow maghemite nanoparticles, Phys. Rev. B. 79 (2009) 094419.

[199] B. Lv, Y. Xu, D. Wu, Y. Sun, Single-crystal α-Fe 2 O 3 hexagonal nanorings: stepwise influence of different anionic ligands (F − and SCN − anions), Chem. Commun. 47 (2011) 967–969.

[200] G. Thomas, F. Demoisson, R. Chassagnon, E. Popova, N. Millot, One-step continuous synthesis of functionalized magnetite nanoflowers, Nanotechnology. 27 (2016) 135604.

[201] R. Ramesh, M. Rajalakshmi, C. Muthamizhchelvan, S. Ponnusamy, Synthesis of Fe 3O 4 nanoflowers by one pot surfactant assisted hydrothermal method and its properties, Mater. Lett. 70 (2012) 73–75.

[202] L.S. Zhong, J.S. Hu, H.P. Liang, A.M. Cao, W.G. Song, L.J. Wan, Self-assembled 3D flowerlike iron oxide nanostructures and their application in water treatment, Adv. Mater. 18 (2006) 2426–2431.

[203] P. Guardia, J. Pérez-Juste, A. Labarta, X. Batlle, L.M. Liz-Marzán, Heating rate influence on the synthesis of iron oxide nanoparticles : the case of decanoic acid., Chem. Commun. 46 (2010) 6108–6110.

[204] C. Moya, X. Batlle, A. Labarta, The effect of oleic acid on the synthesis of Fe3−xO4 nanoparticles over a wide size range, Phys. Chem. Chem. Phys. 17 (2015) 27373–27379.

[205] F. Vereda, J. de Vicente, R. Hidalgo-Alvarez, Oxidation of ferrous hydroxides with nitrate: A versatile method for the preparation of magnetic colloidal particles, J. Colloid Interface Sci. 392 (2013) 50–56.

[206] K. Nishio, M. Ikeda, N. Gokon, S. Tsubouchi, H. Narimatsu, Y. Mochizuki, S. Sakamoto, A. Sandhu, M. Abe, H. Handa, Preparation of size-controlled (30-100 nm) magnetite nanoparticles for biomedical applications, J. Magn. Magn. Mater. 310 (2007) 2408–2410.

[207] C. Martinez-Boubeta, K. Simeonidis, A. Makridis, M. Angelakeris, O. Iglesias, P. Guardia, A. Cabot, L. Yedra, S. Estrade, F. Peiro, Z. Saghi, P.A. Midgley, I. Conde-Leboran, D. Serantes, D. Baldomir, Learning from Nature to Improve the Heat Generation of Iron-Oxide Nanoparticles for Magnetic Hyperthermia Applications, Sci. Rep. 3 (2013).

[208] E. Alphandéry, Y. Ding, A.T. Ngo, Z.L. Wang, L.F. Wu, M.P. Pileni, Assemblies of Aligned Magnetotactic Bacteria and Extracted Magnetosomes: What Is the Main Factor Responsible for the Magnetic Anisotropy?, ACS Nano. 3 (2009) 1539–1547.

[209] S. Chandra, R. Das, V. Kalappattil, T. Eggers, C. Harnagea, R. Nechache, M.-H. Phan, F. Rosei, H. Srikanth, Epitaxial magnetite nanorods with enhanced room temperature magnetic anisotropy, Nanoscale. 9 (2017) 7858–7867.

[210] F. Walz, The Verwey transition - a topical review, J. Phys. Condens. Matter. 14 (2002) R285–R340.

[211] G.F. Goya, T.S. Berquó, F.C. Fonseca, M.P. Morales, Static and dynamic magnetic properties of spherical magnetite nanoparticles, J. Appl. Phys. 94 (2003) 3520–3528.

[212] J.-C. Si, Y. Xing, M.-L. Peng, C. Zhang, N. Buske, C. Chen, Y.-L. Cui, Solvothermal synthesis of tunable iron oxide nanorods and their transfer from organic phase to water phase, CrystEngComm. 16 (2014) 512–516.

[213] T. Macher, J. Totenhagen, J. Sherwood, Y. Qin, D. Gurler, M.S. Bolding, Y. Bao, Ultrathin iron oxide nanowhiskers as positive contrast agents for magnetic resonance imaging, Adv. Funct. Mater. 25 (2015) 490–494.

[214] Y.J. Chen, P. Gao, C.L. Zhu, R.X. Wang, L.J. Wang, M.S. Cao, X.Y. Fang, Synthesis, magnetic and electromagnetic wave absorption properties of porous Fe_3O_4/Fe/SiO2 core/shell nanorods, J. Appl. Phys. 106 (2009) 054303.

[215] W.W. Wang, J.L. Yao, Synthesis and magnetic property of silica/iron oxides nanorods, Mater. Lett. 64 (2010) 840–842.

[216] O. Özdemir, Low-temperature properties of a single crystal of magnetite oriented along principal magnetic axes, Earth Planet. Sci. Lett. 165 (1999) 229–239.

[217] Y. Yang, X.L. Liu, J.B. Yi, Y. Yang, H.M. Fan, J. Ding, Stable vortex magnetite nanorings colloid: Micromagnetic simulation and experimental demonstration, J. Appl. Phys. 111 (2012) 1–9.

[218] S. Dutz, Are Magnetic Multicore Nanoparticles Promising Candidates for Biomedical Applications?, IEEE Trans. Magn. 52 (2016) 1–3.

[219] A. Kostopoulou, S.K.P. Velu, K. Thangavel, F. Orsini, K. Brintakis, S. Psycharakis, A. Ranella, L. Bordonali, A. Lappas, A. Lascialfari, Colloidal assemblies of oriented maghemite nanocrystals and their NMR relaxometric properties, Dalt. Trans. 43 (2014) 8395–8404.

[220] A.P. Roberts, Y. Cui, K.L. Verosub, Wasp-waisted hysteresis loops: Mineral magnetic characteristics and discrimination of components in mixed magnetic systems, J. Geophys. Res. Solid Earth. 100 (1995) 17909–17924.

[221] R. Crichton, Inorganic Biochemistry of Iron Metabolism, John Wiley & Sons, Ltd, Chichester, UK, 2001.

[222] Yi-Xiang, J. Wang, Superparamagnetic iron oxide based MRI contrast agents: Current status

of clinical application, Quant. Imaging Med. Surg. 1 (2011) 35–40.

[223] V. Valdiglesias, N. Fernández-Bertólez, G. Kiliç, C. Costa, S. Costa, S. Fraga, M.J. Bessa, E. Pásaro, J.P. Teixeira, B. Laffon, Are iron oxide nanoparticles safe? Current knowledge and future perspectives, J. Trace Elem. Med. Biol. 38 (2016) 53–63.

[224] P. Guardia, R. Di Corato, L. Lartigue, C. Wilhelm, A. Espinosa, M. Garcia-Hernandez, F. Gazeau, L. Manna, T. Pellegrino, Water-Soluble Iron Oxide Nanocubes with High Values of Specific Absorption Rate for Cancer Cell Hyperthermia Treatment, ACS Nano. 6 (2012) 3080–3091.

[225] L. Lartigue, D. Alloyeau, J. Kolosnjaj-Tabi, Y. Javed, P. Guardia, A. Riedinger, C. Péchoux, T. Pellegrino, C. Wilhelm, F. Gazeau, Biodegradation of Iron Oxide Nanocubes: High-Resolution In Situ Monitoring, ACS Nano. 7 (2013) 3939–3952.

[226] K.H. Bae, M. Park, M.J. Do, N. Lee, J.H. Ryu, G.W. Kim, C. Kim, T.G. Park, T. Hyeon, Chitosan oligosaccharide-stabilized ferrimagnetic iron oxide nanocubes for magnetically modulated cancer hyperthermia, ACS Nano. 6 (2012) 5266–5273.

[227] V.K. Sharma, A. Alipour, Z. Soran-Erdem, Z.G. Aykut, H. V. Demir, Highly monodisperse low-magnetization magnetite nanocubes as simultaneous T 1 – T 2 MRI contrast agents, Nanoscale. 7 (2015) 10519–10526.

[228] F. Ghaemi-Oskouie, Y. Shi, The Role of Uric Acid as an Endogenous Danger Signal in Immunity and Inflammation, Curr. Rheumatol. Rep. 13 (2011) 160–166.

[229] F.J. Lázaro, A.R. Abadía, M.S. Romero, L. Gutiérrez, J. Lázaro, M.P. Morales, Magnetic characterisation of rat muscle tissues after subcutaneous iron dextran injection, Biochim. Biophys. Acta - Mol. Basis Dis. 1740 (2005) 434–445.

[230] M. Safi, S. Clowez, A. Galimard, J.-F. Berret, In vitro toxicity and uptake of magnetic nanorods, J. Phys. Conf. Ser. 304 (2011) 012033.

[231] Z.-G. Yue, W. Wei, Z.-X. You, Q.-Z. Yang, H. Yue, Z.-G. Su, G.-H. Ma, Iron Oxide Nanotubes for Magnetically Guided Delivery and pH-Activated Release of Insoluble Anticancer Drugs, Adv. Funct. Mater. 21 (2011) 3446–3453.

[232] G. Hemery, C. Genevois, F. Couillaud, S. Lacomme, E. Gontier, E. Ibarboure, S. Lecommandoux, E. Garanger, O. Sandre, Monocore vs. multicore magnetic iron oxide nanoparticles: uptake by glioblastoma cells and efficiency for magnetic hyperthermia, Mol. Syst. Des. Eng. 2 (2017) 629–639.

[233] M. Marín-Barba, H. Gavilán, L. Gutiérrez, E. Lozano-Velasco, I. Rodríguez-Ramiro, G.N. Wheeler, C.J. Morris, M.P. Morales, A. Ruiz, Unravelling the mechanisms that determine the uptake and metabolism of magnetic single and multicore nanoparticles in a Xenopus laevis

model, Nanoscale. 10 (2018) 690–704.

[234] R. Xing, A.A. Bhirde, S. Wang, X. Sun, G. Liu, Y. Hou, X. Chen, Hollow iron oxide nanoparticles as multidrug resistant drug delivery and imaging vehicles, Nano Res. 6 (2013) 1–9.

[235] P.P. Wyss, S. Lamichhane, M. Rauber, R. Thomann, K.W. Krämer, V.P. Shastri, Tripod USPIONs with high aspect ratio show enhanced T2 relaxation and cytocompatibility, Nanomedicine. 11 (2016) 1017–1030.

[236] X. Zhou, Y. Shi, L. Ren, S. Bao, Y. Han, S. Wu, H. Zhang, L. Zhong, Q. Zhang, Controllable synthesis, magnetic and biocompatible properties of Fe3O4 and α-Fe2O3 nanocrystals, J. Solid State Chem. 196 (2012) 138–144.

[237] K. Luyts, D. Napierska, B. Nemery, P.H.M. Hoet, How physico-chemical characteristics of nanoparticles cause their toxicity: complex and unresolved interrelations, Environ. Sci. Process. Impacts. 15 (2013) 23–38.

[238] R. Hergt, S. Dutz, R. Müller, M. Zeisberger, Magnetic particle hyperthermia: nanoparticle magnetism and materials development for cancer therapy, J. Phys. Condens. Matter. 18 (2006) S2919–S2934.

[239] R. Hergt, S. Dutz, Magnetic particle hyperthermia—biophysical limitations of a visionary tumour therapy, J. Magn. Magn. Mater. 311 (2007) 187–192.

[240] R. Hergt, R. Hiergeist, M. Zeisberger, D. Schüler, U. Heyen, I. Hilger, W.A. Kaiser, Magnetic properties of bacterial magnetosomes as potential diagnostic and therapeutic tools, J. Magn. Magn. Mater. 293 (2005) 80–86.

[241] G. Vallejo-Fernandez, O. Whear, A.G. Roca, S. Hussain, J. Timmis, V. Patel, K. O'Grady, Mechanisms of hyperthermia in magnetic nanoparticles, J. Phys. D. Appl. Phys. 46 (2013) 312001.

[242] P. Guardia, A. Riedinger, S. Nitti, G. Pugliese, S. Marras, A. Genovese, M.E. Materia, C. Lefevre, L. Manna, T. Pellegrino, One pot synthesis of monodisperse water soluble iron oxide nanocrystals with high values of the specific absorption rate, J. Mater. Chem. B. 2 (2014) 4426.

[243] J.G. Ovejero, D. Cabrera, J. Carrey, T. Valdivielso, G. Salas, F.J. Teran, Effects of inter- and intra-aggregate magnetic dipolar interactions on the magnetic heating efficiency of iron oxide nanoparticles, Phys. Chem. Chem. Phys. 18 (2016) 10954–10963.

[244] D. Serantes, K. Simeonidis, M. Angelakeris, O. Chubykalo-Fesenko, M. Marciello, M. Del Puerto Morales, D. Baldomir, C. Martinez-Boubeta, Multiplying magnetic hyperthermia response by nanoparticle assembling, J. Phys. Chem. C. 118 (2014) 5927–5934.

[245] Z. Nemati, R. Das, J. Alonso, E. Clements, M.H. Phan, H. Srikanth, Iron Oxide Nanospheres and Nanocubes for Magnetic Hyperthermia Therapy: A Comparative Study, J. Electron. Mater. 46 (2017) 3764–3769.

[246] J. Tang, M. Myers, K.A. Bosnick, L.E. Brus, Magnetite Fe 3 O 4 Nanocrystals: Spectroscopic Observation of Aqueous Oxidation Kinetics †, J. Phys. Chem. B. 107 (2003) 7501–7506.

[247] J. Mohapatra, A. Mitra, M. Aslam, D. Bahadur, Octahedral-Shaped Fe_3O_4 Nanoparticles With Enhanced Specific Absorption Rate and R_2 Relaxivity, IEEE Trans. Magn. 51 (2015) 1–3.

[248] Y. Lv, Y. Yang, J. Fang, H. Zhang, E. Peng, X. Liu, W. Xiao, J. Ding, Size dependent magnetic hyperthermia of octahedral Fe_3O_4anoparticles, RSC Adv. 5 (2015) 76764–76771.

[249] M. Ma, Y. Zhang, Z. Guo, N. Gu, Facile synthesis of ultrathin magnetic iron oxide nanoplates by Schikorr reaction., Nanoscale Res. Lett. 8 (2013) 16.

[250] A. Wachowiak, Direct Observation of Internal Spin Structure of Magnetic Vortex Cores, Science. 298 (2002) 577–580.

[251] D.-H. Kim, E.A. Rozhkova, I. V. Ulasov, S.D. Bader, T. Rajh, M.S. Lesniak, V. Novosad, Biofunctionalized magnetic-vortex microdiscs for targeted cancer-cell destruction, Nat. Mater. 9 (2010) 165–171.

[252] S. Tong, C.A. Quinto, L. Zhang, P. Mohindra, G. Bao, Size-Dependent Heating of Magnetic Iron Oxide Nanoparticles, ACS Nano. 11 (2017) 6808–6816.

[253] Z. Nemati, S.M. Salili, J. Alonso, A. Ataie, R. Das, M.H. Phan, H. Srikanth, Superparamagnetic iron oxide nanodiscs for hyperthermia therapy: Does size matter?, J. Alloys Compd. 714 (2017) 709–714.

[254] R. Weissleder, M. Nahrendorf, M.J. Pittet, Imaging macrophages with nanoparticles, Nat. Mater. 13 (2014) 125–138.

[255] V. Hatje, K.W. Bruland, A.R. Flegal, Increases in Anthropogenic Gadolinium Anomalies and Rare Earth Element Concentrations in San Francisco Bay over a 20 Year Record, Environ. Sci. Technol. 50 (2016) 4159–4168.

[256] Z. Zhou, X. Zhu, D. Wu, Q. Chen, D. Huang, C. Sun, J. Xin, K. Ni, J. Gao, Anisotropic shaped iron oxide nanostructures: Controlled synthesis and proton relaxation shortening effects, Chem. Mater. 27 (2015) 3505–3515.

[257] N. Lee, H. Kim, S.H. Choi, M. Park, D. Kim, H.-C. Kim, Y. Choi, S. Lin, B.H. Kim, H.S. Jung, H. Kim, K.S. Park, W.K. Moon, T. Hyeon, Magnetosome-like ferrimagnetic iron oxide nanocubes for highly sensitive MRI of single cells and transplanted pancreatic islets, Proc.

Natl. Acad. Sci. 108 (2011) 2662–2667.

[258] A. Orza, H. Wu, Y. Xu, Q. Lu, H. Mao, One-Step Facile Synthesis of Highly Magnetic and Surface Functionalized Iron Oxide Nanorods for Biomarker-Targeted Applications, ACS Appl. Mater. Interfaces. 9 (2017) 20719–20727.

[259] H.M. Fan, M. Olivo, B. Shuter, J.B. Yi, R. Bhuvaneswari, H.R. Tan, G.C. Xing, C.T. Ng, L. Liu, S.S. Lucky, B.H. Bay, J. Ding, Quantum dot capped magnetite nanorings as high performance nanoprobe for multiphoton fluorescence and magnetic resonance imaging, J. Am. Chem. Soc. 132 (2010) 14803–14811.

[260] E. Pöselt, H. Kloust, U. Tromsdorf, M. Janschel, C. Hahn, C. Ma??lo, H. Weller, Relaxivity optimization of a pegylated iron-oxide-based negative magnetic resonance contrast agent for T 2-weighted spin-echo imaging, ACS Nano. 6 (2012) 1619–1624.

[261] Y. Bao, J.A. Sherwood, Z. Sun, Magnetic iron oxide nanoparticles as T 1 contrast agents for magnetic resonance imaging, J. Mater. Chem. C. 6 (2018) 1280–1290.

[262] H. Bin Na, T. Hyeon, Nanostructured T1 MRI contrast agents, J. Mater. Chem. 19 (2009) 6267.

[263] F.-Y. Chen, Z.-J. Gu, H.-P. Wan, X.-Z. Xu, Q. Tang, Manganese Nanosystem for New Generation of MRI Contrast Agent, Rev. Nanosci. Nanotechnol. 4 (2015) 81–91.

[264] R. Langer, Drug delivery and targeting., Nature. 392 (1998) 5–10.

[265] W. Schütt, C. Grüttner, U. Häfeli, M. Zborowski, J. Teller, H. Putzar, C. Schümichen, Applications of magnetic targeting in diagnosis and therapy--possibilities and limitations: a mini-review., Hybridoma. 16 (1997) 109–17.

[266] Y. Matsumura, H. Maeda, A new concept for macromolecular therapeutics in cancer chemotherapy: mechanism of tumoritropic accumulation of proteins and the antitumor agent smancs., Cancer Res. 46 (1986) 6387–92.

[267] H. Kakwere, M.P. Leal, M.E. Materia, A. Curcio, P. Guardia, D. Niculaes, R. Marotta, A. Falqui, T. Pellegrino, Functionalization of strongly interacting magnetic nanocubes with (thermo)responsive coating and their application in hyperthermia and heat-triggered drug delivery, ACS Appl. Mater. Interfaces. 7 (2015) 10132–10145.

[268] S. Carregal-Romero, P. Guardia, X. Yu, R. Hartmann, T. Pellegrino, W.J. Parak, Magnetically triggered release of molecular cargo from iron oxide nanoparticle loaded microcapsules, Nanoscale. 7 (2015) 570–576.

[269] C. Zhang, Z. Mo, G. Teng, B. Wang, R. Guo, P. Zhang, Superparamagnetic functional C@Fe3O4 nanoflowers: development and application in acetaminophen delivery, J. Mater. Chem. B. 1 (2013) 5908.

[270] L. Cheng, W. Ruan, B. Zou, Y. Liu, Y. Wang, Chemical template-assisted synthesis of monodisperse rattle-type Fe 3 O 4 @C hollow microspheres as drug carrier, Acta Biomater. 58 (2017) 432–441.

[271] K. Cheng, S. Peng, C. Xu, S. Sun, Porous hollow Fe_3O_4 nanoparticles for targeted delivery and controlled release of cisplatin. TL - 131, J. Am. Chem. Soc. 131 VN- (2009) 10637–10644.

[272] S.-W. Cao, Y.-J. Zhu, M.-Y. Ma, L. Li, L. Zhang, Hierarchically Nanostructured Magnetic Hollow Spheres of Fe3O4 and γ-Fe2O3: Preparation and Potential Application in Drug Delivery, J. Phys. Chem. C. 112 (2008) 1851–1856.

[273] M.P. Sharrock, Particulate magnetic recording media: a review, IEEE Trans. Magn. 25 (1989) 4374–4389.

[274] A.E. Berkowitz, R.P. Goehner, E.L. Hall, P.J. Flanders, Microstructure, relaxation, and print- through in γ- Fe 2 O 3 particles, J. Appl. Phys. 57 (1985) 3928–3930.

[275] A. Berkowitz, Some materials considerations in particulate media, IEEE Trans. Magn. 22 (1986) 466–471.

[276] H. Naono, R. Fujiwara, Micropore formation due to thermal decomposition of acicular microcrystals of α-FeOOH, J. Colloid Interface Sci. 73 (1980) 406–415.

[277] M. Stachen, M.P. Morales, M. Ocana, C.J. Serna, Effect of precursor impurities on the magnetic properties of uniform γ-Fe2O3 ellipsoidal particles, Phys. Chem. Chem. Phys. 1 (1999) 4465–4471.

[278] A. Corradi, S. Andress, J. French, G. Bottoni, D. Candolfo, A. Cecchetti, F. Masoli, Magnetic properties of new (NP) hydrothermal particles, IEEE Trans. Magn. 20 (1984) 33–38.

[279] A. Corradi, S. Andress, C. Dinitto, D. Bottoni, G. Candolfo, A. Cecchetti, F. Masoli, Print-through, erasability, playback losses: Different phenomena from the same roots, IEEE Trans. Magn. 20 (1984) 760–762.

[280] M.P. Morales, C. de Julián, J.M. González, C.J. Serna, The effect of the distribution of vacancies on the magnetic properties of γ – Fe2O3 particles, J. Mater. Res. 9 (1994) 135–141.

[281] N.O. Núñez, P. Tartaj, M.P. Morales, R. Pozas, M. Ocaña, C.J. Serna, Preparation, Characterization, and Magnetic Properties of Fe-Based Alloy Particles with Elongated Morphology, Chem. Mater. 15 (2003) 3558–3563.

[282] R. Mendoza-Reséndez, O. Bomati-Miguel, M.P. Morales, P. Bonville, C.J. Serna, Microstructural characterization of ellipsoidal iron metal nanoparticles, Nanotechnology. 15

(2004) S254–S258.

[283] N. Nuñez, P. Tartaj, M. Morales, T. González-Carreño, C. Serna, Correlation between microstructural features and magnetic behavior of Fe-based metallic nanoneedles, Acta Mater. 54 (2006) 219–224.

[284] M.P. Morales, S.A. Walton, L.S. Prichard, C.J. Serna, D.P.E. Dickson, K. O'Grady, Characterisation of advanced metal particle recording media pigments, J. Magn. Magn. Mater. 190 (1998) 357–370.

[285] K. Simeonidis, S. Mourdikoudis, E. Kaprara, M. Mitrakas, L. Polavarapu, Inorganic engineered nanoparticles in drinking water treatment: a critical review, Environ. Sci. Water Res. Technol. 2 (2016) 43–70.

[286] T. Pradeep, Anshup, Noble metal nanoparticles for water purification: A critical review, Thin Solid Films. 517 (2009) 6441–6478.

[287] A.S. Helal, E. Mazario, A. Mayoral, P. Decorse, R. Losno, C. Lion, S. Ammar, M. Hémadi, Highly efficient and selective extraction of uranium from aqueous solution using a magnetic device: succinyl-β-cyclodextrin-APTES@maghemite nanoparticles, Environ. Sci. Nano. 5 (2018) 158–168.

[288] M. Auffan, J. Rose, J.-Y. Bottero, G. V. Lowry, J.-P. Jolivet, M.R. Wiesner, Towards a definition of inorganic nanoparticles from an environmental, health and safety perspective, Nat. Nanotechnol. 4 (2009) 634–641.

[289] M. Auffan, J. Rose, O. Proux, D. Borschneck, A. Masion, P. Chaurand, J.-L. Hazemann, C. Chaneac, J.-P. Jolivet, M.R. Wiesner, A. Van Geen, J.-Y. Bottero, Enhanced Adsorption of Arsenic onto Maghemites Nanoparticles: As(III) as a Probe of the Surface Structure and Heterogeneity, Langmuir. 24 (2008) 3215–3222.

[290] S. Brice-Profeta, M.-A. Arrio, E. Tronc, N. Menguy, I. Letard, C. Cartier dit Moulin, M. Noguès, C. Chanéac, J.-P. Jolivet, P. Sainctavit, Magnetic order in - nanoparticles: a XMCD study, J. Magn. Magn. Mater. 288 (2005) 354–365.

[291] M.S. Onyango, Y. Kojima, H. Matsuda, A. Ochieng, Adsorption Kinetics of Arsenic Removal from Groundwater by Iron-Modified Zeolite., J. Chem. Enginnering Japan. 36 (2003) 1516–1522.

[292] G.A. Waychunas, C.S. Kim, J.F. Banfield, Nanoparticulate Iron Oxide Minerals in Soils and Sediments: Unique Properties and Contaminant Scavenging Mechanisms, J. Nanoparticle Res. 7 (2005) 409–433.

[293] A. Khodabakhshi, M.M. Amin, M. Mozaffari, Synthesis of magnetite nanoparticles and evaluation of its efficiency for arsenic removal from simulated industrial waste water, Iran. J.

Environ. Heal. Sci. Eng. 8 (2011) 189–200.

[294] S.R. Chowdhury, E.K. Yanful, Arsenic and chromium removal by mixed magnetite–maghemite nanoparticles and the effect of phosphate on removal, J. Environ. Manage. 91 (2010) 2238–2247.

[295] M. Iram, C. Guo, Y. Guan, A. Ishfaq, H. Liu, Adsorption and magnetic removal of neutral red dye from aqueous solution using Fe_3O_4 hollow nanospheres, J. Hazard. Mater. 181 (2010) 1039–1050.

[296] G.S. Parkinson, U. Diebold, J. Tang, L. Malkinski, Tailoring the Interface Properties of Magnetite for Spintronics, Adv. Magn. Mater. (2012) 61–88.

[297] Z. Zhang, S. Satpathy, Electron states, magnetism, and the Verwey transition in magnetite, Phys. Rev. B. 44 (1991) 13319–13331.

[298] A. Mitra, B. Barick, J. Mohapatra, H. Sharma, S.S. Meena, M. Aslam, Large tunneling magnetoresistance in octahedral Fe_3O_4 nanoparticles, AIP Adv. 6 (2016) 055007.

[299] A. Pratt, M. Kurahashi, X. Sun, Y. Yamauchi, Adsorbate-induced spin-polarization enhancement of Fe_3O_4 (0 0 1), J. Phys. D. Appl. Phys. 44 (2011) 064010.

[300] G. Sun, B. Dong, M. Cao, B. Wei, C. Hu, Hierarchical Dendrite-Like Magnetic Materials of Fe_3O_4 , γ-Fe_2O_3 , and Fe with High Performance of Microwave Absorption, Chem. Mater. 23 (2011) 1587–1593.

[301] C.-L. Zhu, M.-L. Zhang, Y.-J. Qiao, G. Xiao, F. Zhang, Y.-J. Chen, Fe_3O_4/TiO_2 Core/Shell Nanotubes: Synthesis and Magnetic and Electromagnetic Wave Absorption Characteristics, J. Phys. Chem. C. 114 (2010) 16229–16235.

[302] R.K. Walser, W. Win, P.M. Valanju, Shape-optimized ferromagnetic particles with maximum theoretical microwave susceptibility, IEEE Trans. Magn. 34 (1998) 1390–1392.

[303] Y. Yang, M. Li, Y. Wu, B. Zong, J. Ding, Size-dependent microwave absorption properties of Fe_3O_4 nanodiscs, RSC Adv. 6 (2016) 25444–25448.

[304] X. Li, B. Zhang, C. Ju, X. Han, Y. Du, P. Xu, Morphology-controlled synthesis and electromagnetic properties of porous Fe_3O_4 nanostructures from iron alkoxide precursors, J. Phys. Chem. C. 115 (2011) 12350–12357.

[305] X. Liu, Z. Zhong, Y. Tang, B. Liang, Review on the Synthesis and Applications of Fe_3O_4 Nanomaterials, J. Nanomater. 2013 (2013) 1–7.

[306] O. Delmer, P. Balaya, L. Kienle, J. Maier, Enhanced Potential of Amorphous Electrode Materials: Case Study of RuO_2, Adv. Mater. 20 (2008) 501–505.

[307] S. Jin, H. Deng, D. Long, X. Liu, L. Zhan, X. Liang, W. Qiao, L. Ling, Facile synthesis of hierarchically structured Fe_3O_4/carbon micro-flowers and their application to lithium-ion

battery anodes, J. Power Sources. 196 (2011) 3887–3893.

[308] Y. Zeng, R. Hao, B. Xing, Y. Hou, Z. Xu, One-pot synthesis of Fe_3O_4 nanoprisms with controlled electrochemical properties, Chem. Commun. 46 (2010) 3920.

[309] B. Koo, H. Xiong, M.D. Slater, V.B. Prakapenka, M. Balasubramanian, P. Podsiadlo, C.S. Johnson, T. Rajh, E. V. Shevchenko, Hollow Iron Oxide Nanoparticles for Application in Lithium Ion Batteries, Nano Lett. 12 (2012) 2429–2435.